# Mesoscopic Electronics Beyond DC Transport

A dissertation presented
by

Leonardo Di Carlo

to
The Department of Physics
in partial fulfillment of the requirements
for the degree of
Doctor of Philosophy
in the subject of

Physics

Harvard University
Cambridge, Massachusetts

November 2007

© 2007 by Leonardo Di Carlo
All rights reserved.

Dissertation Advisor: Professor Charles M. Marcus Author: Leonardo Di Carlo

# Mesoscopic Electronics Beyond DC Transport

## Abstract

Since the inception of mesoscopic electronics in the 1980's, direct current (dc) measurements have underpinned experiments in quantum transport. Novel techniques complementing dc transport are becoming paramount to new developments in mesoscopic electronics, particularly as the road is paved toward quantum information processing. This thesis describes seven experiments on GaAs/AlGaAs and graphene nanostructures unified by experimental techniques going beyond traditional dc transport.

Firstly, dc current induced by microwave radiation applied to an open chaotic quantum dot is investigated. Asymmetry of mesoscopic fluctuations of induced current in perpendicular magnetic field is established as a tool for separating the quantum photovoltaic effect from classical rectification.

A differential charge sensing technique is next developed using integrated quantum point contacts to resolve the spatial distribution of charge inside a double quantum dot. An accurate method for determining interdot tunnel coupling and electron temperature using charge sensing is demonstrated.

A two-channel system for detecting current noise in mesoscopic conductors is developed, enabling four experiments where shot noise probes transmission properties not available in dc transport and Johnson noise serves as an electron thermometer.

Suppressed shot noise is observed in quantum point contacts at zero parallel magnetic field, associated with the 0.7 structure in conductance. This suppression evolves with increasing field into the shot-noise signature of spin-lifted mode degeneracy. Quantitative agreement is found with a phenomenological model for density-dependent mode splitting.

Shot noise measurements of multi-lead quantum-dot structures in the Coulomb blockade

regime distill the mechanisms by which Coulomb interaction and quantum indistinguishability correlate electron flow. Gate-controlled sign reversal of noise cross correlation in two capacitively-coupled dots is observed, and shown to arise from interdot Coulomb interaction. Super-Poissonian auto-correlation and positive cross correlation are measured in a multi-lead dot, and shown consistent with dynamical blockade of multi-level transport.

Shot noise measurements in graphene nanostructures reveal a Fano factor independent of carrier type and density, device geometry, and the presence of a $p$-$n$ junction. This result contrasts with theory for ballistic graphene sheets and junctions, and points to strong influence of disorder on transmission.

A final experiment investigating the graphene $p$-$n$ junction in the quantum Hall regime reminds us the power of dc transport. New conductance plateaus are observed at 1 and $3/2 \times e^2/h$, consistent with recent theory for equilibration of edge states at the $p$-$n$ interface.

# Contents

# List of Figures

# Acknowledgements

As I approach the finish line of this ultra-marathon that is a Ph.D., I am thrilled to express my gratitude to the many people who have helped me both personally and scientifically along the way.

First and foremost I thank Prof. Charles Marcus, or simply Charlie, as everyone calls this charismatic anomaly in the world of physics. I shall never forget my first impression of Charlie in electricity and magnetism class for Physics freshmen at Stanford. Ever since that day in January 1995, I have admired Charlie's ability to explain the most abstract of physics concepts drawing examples from daily life, his casual yet absolutely precise manner of speech, and his unending passion for physics beyond mesoscopics and the technical disciplines (cryogenics and nanofabrication, to name a few) that make our research specialty possible. I thank Charlie for welcoming me to his research group in July 2001, recognizing from the start the half engineer, half physicist in me and guiding me through the years to exciting mesoscopic physics experiments that involved measurement techniques new to me and to the group. I thank him for teaching me the fine art of being an experimentalist, which at times has even involved us chasing ground loops way past midnight! I thank him for creating a uniquely productive lab in which every instrument works, every tool is in its place, and coffee never runs out! Most importantly, I thank him for fostering the environment of open communication and sharing that so uniquely characterizes his group.

This brings me to my labmates, past and present. Through the tasks they perform(ed) as czars, and through their energetic participation at group meetings and journal clubs, they keep the lab running smoothly and our discussions of mesoscopic physics at high level. Bear with me, the list of labmates with whom I have had the pleasure to overlap is long: Jacob Aptekar, Christian Barthel, Rob Barton, Andrew Bestwick, Michael Biercuk, Lily Childress, Jerry Chow, Sang Lin Chu, Hugh Churchill, Nathaniel Craig, Keirsun Crockett,

Sara Cronenwett, Michaelangelo D'Agostino, Josh Folk, Slaven Garaj, Alex Johnson, Jennifer Harlow, Reinier Heeres, Bart Horn, Andy Kent, Will Koehl, Edward Laird, Heather Lynch, Eli Levenson-Falk, Nadya Mason, Doug McClure, Jeff Miller, Douwe Monsma, Jesper Nygard, Elina Onitskanski, Jason Petta, Ron Potok, David Reilly, Sarah Slater, Hadar Steinberg, Carolyn Stwertka, Susan Watson, Jimmy Williams, Yiming Zhang, Dominik Zumbuhl, and Floris Zwanenburg.

I wish to thank the labmates I had the pleasure of collaborating with during the projects presented in this thesis. Thanks to Susan Watson for the intensive course in cryogenics and low-noise measurement she guided me through during my first month with the group, which proved so useful during my first project dealing with photocurrents. I thank Dominik, expert in the measurement of mesoscopic fluctuations, for teaching me early on to acquire statistics fast (and even faster!), and for many car rides home late at night.

Many thanks to Heather and Lily for our joint effort on that challenging project called charge-Rabi, of which our differential charge sensing work together with Alex and Keirse was a spin-off. The time we spent learning to transmit broadband signals down the dilution refrigerator was among the most rewarding experiences in graduate school. It is a pleasure to see many of the tricks we developed together during that time being in use still today, including soldering coax directly onto chip carriers! On a personal note, I thank them both for spreading their passion for long-distance running to me. I have them to thank for the loss of $\sim$ 20 lbs in 2003 (more than half of which I've have regained since!). And Alex, thanks for proving that genius and modesty can go hand in hand.

I thank Doug and Yiming for joining forces with me and forming the Noise Team. If one word summarizes our effort to produce a performant noise measurement system, it would be *perseverance!* We have come a long way from being swamped by $1/f$ noise and snail-paced number crunching in our early, lower-frequency implementations of the system. It has been a pleasure witnessing Doug's evolution from a college freshman with an uncanny talent for computers to a graduate student who also digs deep into low-temperature physics books

like Pobell and Lounasmaa's. Thanks as well for all the tennis matches! I am especially thankful to Yiming for his sharp mind and his surgeon-quality steady hands. I truly value the many late nights we have spent in front of the blackboard discussing circuits, noise and results in the literature, motivating each other with the occasional *think about it!*

Recently, I have had the pleasure of also collaborating with Jimmy Williams. I thank Jimmy for teaching me so much about graphene fabrication in exchange for some electronics tips. I thank him also for being a great friend (the kind that takes you to the Dave Matthew's concert in Fenway and always offers you a ride home at the end of the day [although it might involve walking farther to his car than to your place!]) and a great running buddy.

I have David Reilly to thank for radiating so much well-being since arriving as a post-doc in 2004, and for becoming one of my closest friends. I am still surprised by the many resonances we share, starting from our nearly identical interests in music, both in listening to and making it (even down to our choice of drums and then guitar as favorite instruments), through high-frequency electronics and 0.7 structure, to sports. I have particularly enjoyed tapping into the *Reillypedia*, that seemingly infinite knowledge of his on nearly every topic, over lunch, coffee, and especially whisky. I especially thank this Renaissance man for being a role model to everyone in the lab.

I extend a very special thank you to Cem Duruöz (whom I've never met), Alex, Sara, Nathaniel, Sarah, Elina, and Jeff for selflessly lending quantum dots and point contacts they fabricated for many of the experiments presented in this thesis.

Moving beyond the Marcus lab, I extend my gratitude to Prof. James Harris at Stanford, Micah Hanson and Arthur Gossard at UCSB, and Loren Pfeiffer and Ken West at Alcatel-Lucent for growing the high-quality heterostructures that make the above devices possible.

I extend a big thank you to the theorists with whom I have collaborated during the Ph.D.: they are Maxim Vavilov, Hans-Andreas Engel, Caio Lewenkopf, Leonid Levitov, and Dima Abanin. Eugene Sukhorukov, Ramon Aguado, David Sanchez, and Valentin Rychkov provided many illuminating discussions at conferences. E-mail correspondence with Wilfred

van der Wiel, Michael Moskalets, and Mikhail Polianski is also greatly appreciated.

I thank my pre-Harvard mentors both at Stanford University and at CEA-Saclay, William Oliver, Yoshi Yamamoto, Christian Glattli and Patrice Roche, for showing me that noise can sometimes be the most interesting signal. The brief periods I worked in their labs as a REU, Master's and DEA student helped me define a long-term interest in noise measurements that is reflected in five of the chapters ahead.

I thank Amir Yacoby, Misha Lukin, Paul Horowitz, and Charlie, my qualifying exam committee, for their long-term support, guidance, and reading of my yearly progress reports, and Leonid Levitov, Amir, Misha, and Charlie for accepting my invitation to form the stellar Ph.D. committee to which I will have the pleasure of presenting this thesis shortly.

I wish to thank Louis DeFeo and his team in the machine shop for expertly bringing to life the designs I have submitted during these years. Thanks Louis for patiently teaching me the art of hand-drawing schematics. I also thank our local electronics genius James McArthur, whose highly versatile and now world-renowned digital-to-analog converters (in their various incarnations) have been essential in all experiments I have worked on.

None of the work presented here would have been possible without the hard work of the people who administer, execute and deliver our lab's purchasing requests. A sincere thank you to the three James's (Gotfredson, Houlahan and Reynolds), who have worked around the clock to keep our orders processed and delivered in a timely fashion, and our personal expenses reimbursed. Thanks to Ralph Generazzo and Joan Frankel in the SEAS purchasing department for their hard work and their patience, especially regarding requests for overnight deliveries! And finally, thanks to Tomas Rosado and Matt Toomey in McKay shipping and receiving, who countless times went beyond the call of duty to deliver and send packages. I am forever thankful to Tom for his spirit, the improptu salsa lessons he gave us on several occasions in the lab, and for many wonderful times at his house, including one Christmas. I wish him a happy retirement following 32 years of service to Harvard.

And we come to the wonderful administrative staff in the physics department. I espe-

cially thank Sheila Ferguson for much more than her understanding of my misunderstanding of administrative deadlines. Sheila, a wonderful friend, has always kept the door open for me and offered valuable advice while treating me to a cappuccino. I thank Kathy Ryan for several short-term interest-free loans during a time when my rent was *obviously* much too high, and for her desire to make my graduate-student life easier. Thanks also to Vickie Green, whose wit makes me smile even in the grayest days of winter.

I wish to thank the Harvard NSEC for providing me graduate student funding during two academic years. A special thank you to Naomi Brave, Robert Graham, and Robert Westervelt for also allocating the funds that let me attend the $6^{\text{th}}$ Rencontres du Vietnam. I thank the IBM Ph.D. fellowship program for funding me during the last semester of graduate school, and for a wonderful internship at the T. J. Watson Research center this past summer. I thank Drs. Chun-yung Sung, Phaedon Avouris, Zhihong Chen, and Yu-ming Lin for welcoming me to Aisle 2, and especially Zhihong for patiently teaching me so much graphene fabrication just days before giving birth.

Outside the world of physics, I first thank Laura Vincens, my high school counselor and friend since 1991, for believing in me more than I believe in myself. Thanks to my long-term Stanford friends, Danny Podolsky, Carrie Dodson, Yannick Kassum, and the *Vaches Folles!* with whom I once dreamed of rock-stardom playing tunes from around the world. I thank all my friends at the Cambridge Running Club, and especially Daniel Goldberg, Leah Jones, Heidi Schafer, Eileen Harrington, and Jen George, for extending their friendship beyond the Harvard and MIT tracks. I especially thank Leah for sharing her apartment with me during the interim period dedicated to writing this thesis.

Last but not least, I extend my deepest gratitude to my family. My parents, Alicia and Oscar, have always provided me with the unending love and support that enables me to pursue my dreams even when it means, as it will soon, going 5300 miles away from home to do it. And I thank my sister Natalia, my closest friend, for always being there and for bringing my god-daughter Laia into this world.

*In loving memory of Angie and Chava.*

# Chapter 1

# Introduction

Mesoscopic electronics concerns conductors whose dimensions are intermediate between the macroscopic scale of our everyday experience and the atomic scale. Spanning the range of tens of nanometers to several microns, the mesoscopic length scale is where electrons in semiconductors and metals can manifest their quantum mechanical nature, at once wave- and particle-like, when cooled to a few degrees Kelvin. The interplay between wave-like and particle-like electrical conduction is a central theme in mesoscopic electronics [1, 2].

## 1.1 Wave or particle?

As an illustration of quantum transport at the two extremes, we consider a quantum dot (QD) [3] of area 0.7 $\mu$m$^2$ coupled to large source and drain electronic reservoirs [Fig. 1.1(a)] at temperature $T < 1$ K. Figures 1.1(b) and 1.1(d) show measurements of differential conductance $g = dI/dV_{\rm sd}$, the current response to a voltage excitation, for strong and weak coupling to the reservoirs.

In the open regime [Figs. 1.1(a) and 1.1(b)], $g$ shows fluctuations as a function of perpendicular magnetic field $B_\perp$. These fluctuations of order 20% about an average of $\sim 1e^2/h$ are not measurement noise: they are (almost) perfectly repeatable and symmetric in $B_\perp$. They are a spectacular manifestation of wave-like interference between phase-coherent electron trajectories traversing the dot, and of the scrambling of the interference pattern by $B_\perp$ [4].

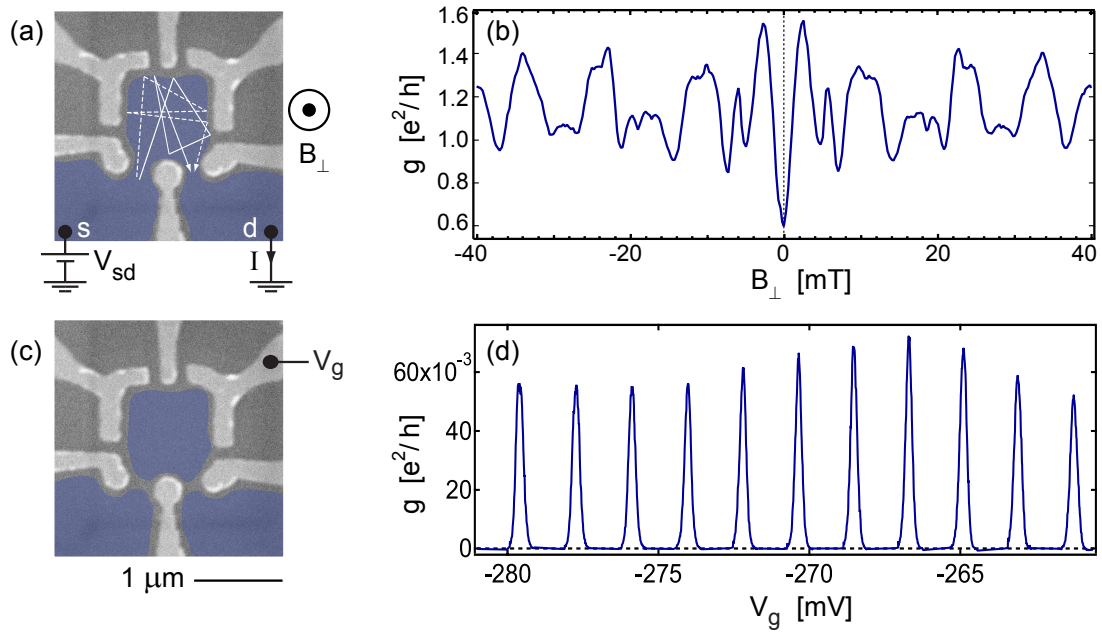


Figure 1.1: (a) Scanning electron micrograph of a quantum dot of area 0.7 $\mu$m$^2$ defined and controlled by negative voltages applied to metallic gates on the surface of GaAs/AlGaAs heterostructure with a 2 dimensional electron gas (2DEG) $\sim$ 100 nm below the surface. Added false color indicates regions of the 2DEG not depleted by the gates which define a quantum dot coupled to electronic reservoirs. (b) Differential conductance $g$ as a function of perpendicular magnetic field $B_\perp$ in the open regime shows strong fluctuations near perfectly symmetric in $B_\perp$ ($T \sim 200$ mK). (c) More negative voltages applied to the lower three gates extends the 2DEG depletion, limiting the coupling between dot and reservoirs to tunneling. (d) In this nearly-closed regime, $g$ reveals sharp peaks at nearly-periodic settings of the plunger gate voltage $V_{\rm g}$ ($T \sim 60$ mK). In between peaks, charge inside the dot is quantized.

Upon reducing the coupling into the tunneling regime [Figs. 1.1(c) and 1.1(d)], $g$ becomes sharply peaked at quasi-periodic settings of the gate voltage $V_{\rm g}$. In between the peaks, $g$ vanishes because the electrostatic energy cost of adding or removing a single electron from the puddle exceeds the thermal energy $k_BT$, and the electron number in the puddle is quantized. Known as Coulomb blockade (CB) [3], this phenomenon manifests spectacularly the particle nature of the electron.

## 1.2 Direct current transport

Measurements in Fig. 1.1 are examples of direct current (dc) transport. Since the inception of mesoscopic electronics in the mid eighties, measurements of this kind have enabled key developments in the field. Notable among them are the discovery of the integer [5] and fractional [6] quantum Hall effects in two-dimensional (2D) conductors, the quantization of ballistic conductance in quantum point contacts (QPCs) [7, 8], and the Kondo effect in quantum dots [9, 10].

We take a moment to carefully define dc transport as the term is used throughout this thesis. We refer by dc transport to the static current that flows through a conductor in response to a static voltage excitation applied across its terminals [Fig. 1.2(a)], as well as to the dual situation involving a static voltage response to a static injected current [Fig. 1.2(b)]. The name is also applied to versions of these measurements involving more than two terminals, such as the four-wire technique which eliminates series and contact resistance and facilitates the interpretation of data. In practice, transport measurements are rarely purely dc, owing largely to $1/f$ noise in both devices and amplifiers. Most often measurements are done using the standard lock-in technique [11] with sinusoidal excitation at frequency $10 - 1000$ Hz [Fig. 1.2(c)] . Since this time scale is longer than that of electron dynamics in mesoscopic conductors (rarely longer than microseconds), near-dc lock-in measurements are also called dc transport.

## 1.3 Beyond dc transport

The seven experiments presented in this thesis reflect my goal to explore in graduate school a wide variety of topics in mesoscopic electronics while learning, and possibly helping develop, measurement techniques going beyond dc transport. These experiments investigate GaAs/AlGaAs QPCs, GaAs/AlGaAs quantum dots in open and CB regimes, and graphene nanostructures. The main theme connecting these experiments is the use of measurement

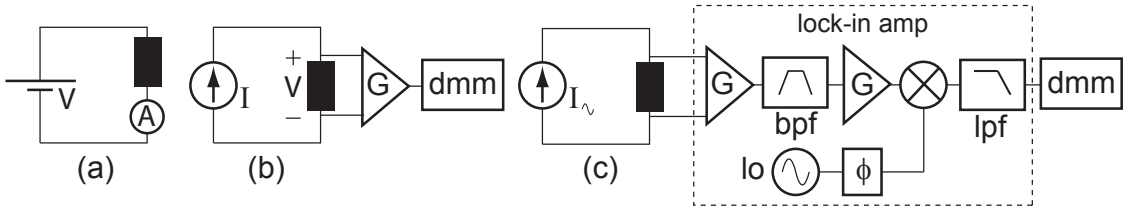


Figure 1.2: (a,b) Schematic of dc transport measurements using (a) voltage bias and (b) current bias. (c) Schematic of a current-bias measurement by lock-in detection. A sinusoidal current excitation at a frequency $f$ (typically $10 - 1000$ Hz) is applied. The voltage across the device is amplified, band-limited (bpf) around $f$, amplified more, and mixed down to dc by a local oscillator (lo) phase locked to the current excitation. A final low-pass filter (lpf) time-averages the dc output, which is proportional the ac voltage across at the device at $f$.

techniques going beyond dc transport as defined above.

Following a brief introduction comparing the GaAs/AlGaAs heterostructure and graphene 2D conductors from which all the nanostructures investigated are patterned, Chapter 3 investigates the mesoscopic fluctuations of dc current induced in open chaotic quantum dots by microwave radiation. Chapter 4 presents the development of differential charge sensing, a technique that uses proximal QPCs to locally sense the distribution of charge inside a double quantum dot, and which enables a new method for determining the interdot coupling and electron temperature. Chapter 5 describes the design, fabrication, calibration and performance of the two-channel noise measurement system that enables the physics experiments presented in four subsequent chapters. Chapter 6 investigates current noise in QPCs, revealing a suppression of shot noise associated with the 0.7 conductance anomaly, and bias-dependent electron heating effects. Chapters 7 and 8 are devoted to the study of shot noise in highly tunable multi-terminal single and double quantum dots operated in the CB regime. Chapter 9 reports, to my knowledge, the first experimental investigation of shot noise in graphene nanostructures, including a $p$-$n$ junction. A final chapter devoted to the quantum Hall effect in the graphene $p$-$n$ junction reminds us the power of the dc transport technique.

Three appendices provide supplementary experimental and theoretical details which

might be useful to others in the field. Appendix A describes various techniques I have explored for coupling signals in the MHz-GHz range down a dilution refrigerator. Appendix B provides derivations of two double-dot equations in Ch. 4. Finally, App. C presents Matlab code for simulating sequential transport of single and double quantum dots.

The three measurements beyond dc transport – microwave induced dc-current, charge sensing and current noise – and the physics experiments they enable are now introduced one by one with minimum use of mathematics.

## 1.4 Microwave-induced dc currents in open chaotic quantum dots

### 1.4.1 Theory background

We discuss three mechanisms by which a time-periodic variation of the confining potential of an open quantum dot can produce a dc current $I$ with zero dc bias. Two of them, the photovoltaic effect and adiabatic quantum pumping, are quantum interference effects arising from the absence of left-right symmetry (LRS) of scattering across a time-dependent potential[1]. The third, rectification, is a classical effect that involves the mixing-down to dc of an ac voltage across the dot terminals by either a non-linear conductance, a time-dependent conductance, or both.

We consider first the case of a static confining potential. Within the Landauer-Büttiker (L-B) framework [2] describing transport through phase-coherent conductors by scattering of incident electronic plane waves into outgoing waves,

$$I = \frac{e}{h} \sum_n \int dE \left[ |S_{ds}(E)|^2 - |S_{sd}(E)|^2 \right] f(E).$$

Here, $f(E) = [1 + \exp((E-\mu)/k_B T)]^{-1}$ is the Fermi-Dirac distribution function with $\mu$ the chemical potential in both leads, and $S_{ds}$ is the scattering amplitude for an electron incident

[1]More traditional turnstile pumps [12] rely on Coulomb-charging effects.

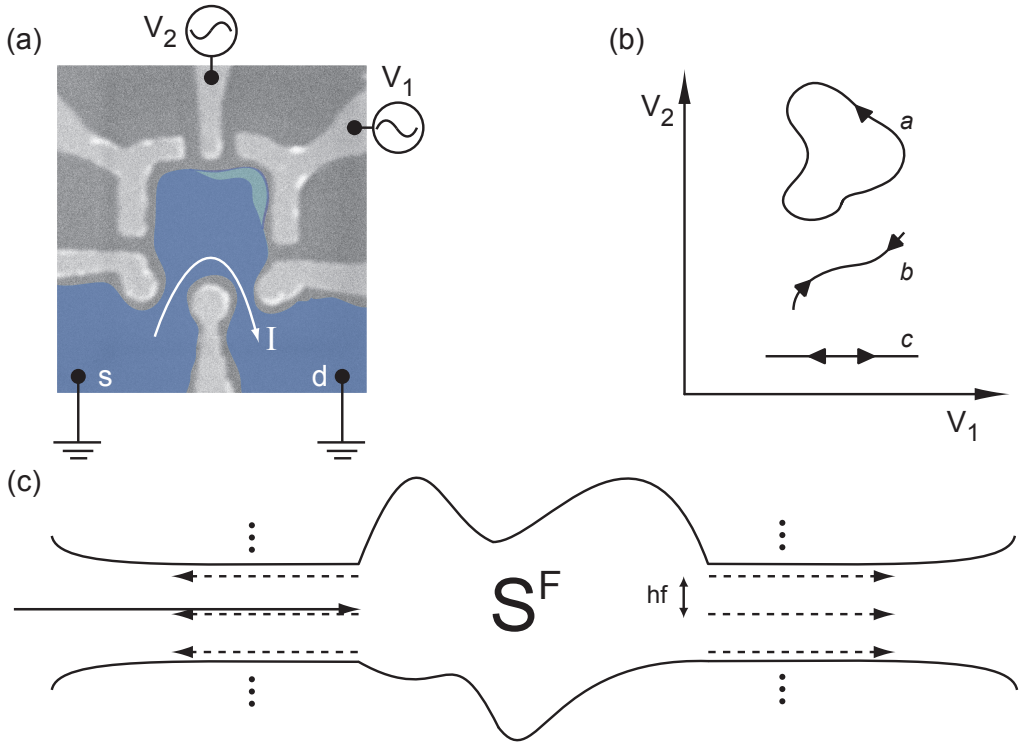


Figure 1.3: (a) Periodic voltages applied to the dot-defining gates can induce a dc current $I$ through the dot with both leads grounded. (b) Finite pumping current $I^{(1)}$ requires tracing a finite area in parameter space, for example contour *a*. $I^{(1)} = 0$ for contours *b* and *c*. Tracing contour *a* in the opposite direction reverses the sign of $I^{(1)}$. All three contours can generate photocurrents. (c) Illustration of Floquet scattering. Incident electron waves can absorb or emit energy quanta as they scatter through the time-dependent potential.

on the source to exit at the drain[2]. Unitarity of the scattering matrix $S$ requires $|S_{ds}(E)| = |S_{sd}(E)|$ regardless of the shape of the confining potential. This LRS of transmission means that $I = 0$.[3]

When the confining potential is time-periodic [for example, as a result of time-dependent voltages applied to one or two top gates, as shown in Fig. 1.3(a)], LRS can be broken and

[2]We assume single-mode inputs and outputs for simplicity and consistency with the experiment. For the multi-mode case, we would replace $|S_{ds}|^2$ above with $\mathrm{tr}(S_{ds}^{\dagger} S_{ds})$.

[3]Time-reversal symmetry also requires $S_{ds}(B_\perp) = S_{sd}(-B_\perp)$. Combined with unitarity of $S$, this leads to the symmetry of $g$ in $B_\perp$.

finite $I$ induced. Within the framework of Floquet scattering [13, 14, 15], an extension of L-B to time-dependent potentials, incident electron waves absorb and emit energy quanta as they scatter through the dot, and

$$I = \frac{e}{h} \sum_n \int dE \left[ |S^F_{ds}(E_n, E)|^2 - |S^F_{sd}(E_n, E)|^2 \right] f(E).$$

Here, $E_n = E + n\hbar\omega$, with $\omega$ the fundamental frequency of the modulation, and $S^F_{ds}(E_n, E)$ is the scattering amplitude for an electron wave at energy $E$ incident from the source to exit at the drain while absorbing ($n > 0$) or emitting ($n < 0$) $|n|$ quanta [Fig. 1.3(c)]. Unitarity of the Floquet scattering matrix $S^F$ does not require that incident waves scatter with the same net probability from source to drain as from drain to source, so $\sum_n |S^F_{ds}(E_n, E)|^2 \neq \sum_n |S^F_{sd}(E_n, E)|^2$ and $I \neq 0$ in general. Also, unitarity of $S^F$ and time-reversal symmetry combined do not require $\sum_n |S^F_{ds}(E_n, E, B_\perp)|^2 \neq \sum_n |S^F_{sd}(E_n, E, -B_\perp)|^2$. This means that symmetry in $B_\perp$ is not expected for $I$.

The induced current can be expanded as $I = \sum_{n>0} I^{(n)}$, with $I^{(n)} \propto (w/\gamma_{\rm esc})^n$. Here, $\gamma_{\rm esc} = 2\Delta/h$ is the inverse dwell time of electrons in the dot, with $\Delta$ the quantum level spacing. The scale $\hbar\gamma_{\rm esc}$ of energy-dependence in the scattering matrix sets the frequency scale for pumping-dominated $I$ (the adiabatic regime $\omega << \gamma_{\rm esc}$) and for photocurrent dominated $I$ (the non-adiabatic regime $\omega << \gamma_{\rm esc}$). Many characteristics of $I^{(1)}$ justify the name pumping current. First, the charge transferred per unit time is proportional to the pump speed. Second, applying the modulation in reverse changes the sign of $I^{(1)}$. This last property means that a one-parameter variation of the confining potential will not induce any finite $I^{(1)}$, and neither will a two-parameter variation that does not trace a finite-area contour in parameter space [Fig. 1.3(b)]. In contrast, photocurrent is not reversible and can be induced with a single-parameter variation (though only strongly in the non-adiabatic regime).

### 1.4.2 Experiment

Chapter 3 presents an investigation [16] of dc current generation in an open chaotic quantum dot with continuous-wave excitation, ranging from MHz to GHz, applied to only one gate. For adiabatic frequencies (low MHz), we find that single-gate excitation *can* induce a finite $I$. In this regime, the observed mesoscopic fluctuations of $I$ (about a zero average) are symmetric in $B_\perp$. This suggests that rectification - due to parasitic coupling of the gate voltage to the reservoirs combined with gate-dependent conductance (itself symmetric in $B_\perp$) - is the principal source of induced current in this regime.

For gate-voltage modulation at GHz frequencies, $I$ is found to be either predominantly symmetric or completely asymmetric in $B_\perp$ depending on the particular frequency. We interpret these results as showing competing mechanisms of induced mesoscopic current in the GHz regime, with photocurrent producing a signal fully asymmetric in $B_\perp$ and rectification producing a signal predominantly symmetric in $B_\perp$. We establish field symmetry as an experimental tool for separating photovoltaic currents from rectification currents.

### 1.4.3 Relevance

This experiment was a timely exploration of new effects predicted by a very active theoretical literature inspired by the pioneering experiment [17] on adiabatic quantum pumping in 1999. The experiment had reported $B_\perp$-symmetric pumping, consistent with theory developed nearly synchronously [18]. Subsequent theory soon discovered that dc currents induced by adiabatic quantum pumping should not show field symmetry [19, 20], suggested rectification as a possible explanation for the symmetries observed [21], and extended beyond the adiabatic regime [22, 13]. Our measurements in the adiabatic regime shed experimental light on the role rectification could have played in the earlier experiment. Our use of field symmetry as an experimental tool for distinguishing between photocurrent and rectification was revisited in subsequent theory in collaboration with Maxim Vavilov [23]. Rectification

currents were found to remain predominantly symmetric in the frequency range of the experiment.

## 1.5 Differential charge sensing

### 1.5.1 Background

Charge sensing is the use of an independent conduction path to measure the number and distribution of charges in a nearby conductor. A QPC [24, 25], quantum dot [26], metallic single-electron transistor [27] or any other device whose conductance is sensitive to the local electrostatic environment can serve as a charge sensor. In our lab, the most common charge sensor is a QPC gate-biased at the point of maximal transconductance.

Charge sensing often goes by other names. *Listening* is very descriptive, but somewhat inappropriate. Being a form of measurement, albeit weak, charge sensing inevitably exerts a back-action [28, 29, 30] on the system being detected. *Field effect* is also a popular name, for two reasons. First, M. Field is lead-author of the first paper [24] reporting the use of a QPC to charge-sense a quantum dot in CB. Second, there is a close analogy between charge sensing and the field effect transistor [31], where gate charge controls the carrier density and thereby the conductivity of the independent channel underneath.

### 1.5.2 Experiment

Chapter 4 demonstrates differential charge sensing (DCS) of a semiconductor double quantum dot operating in CB [32]. *Differential* means that integrated QPC sensors positioned at opposite side of the double dot can each resolve the spatial distribution of a fixed total charge within the system (Fig. 1.4). Charge sensing is then used to investigate delocalization arising from hybridization of charge states by gate-controlled interdot tunnel coupling $t$. The main result is an improved method for determining $t$ and the electron temperature without requiring transport.

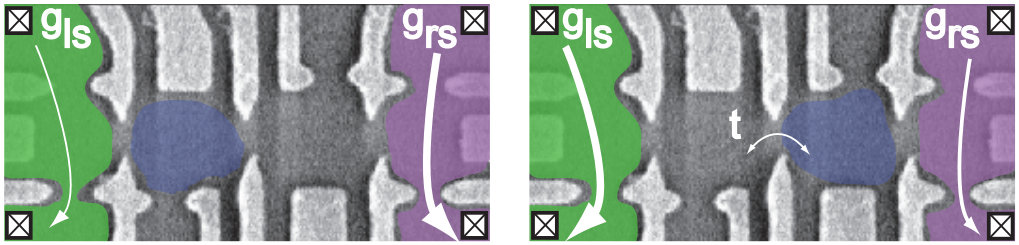


Figure 1.4: Illustration of differential charge sensing. Conductance through each of two independent QPC charge sensors on opposite sides of a double quantum dot shows a few-percent reduction when a single charge is transitioned from the far dot into the adjacent dot. Charge sensing also allows an accurate measurement of the interdot tunnel coupling $t$ and the electron temperature.

### 1.5.3 Relevance

Delocalization had been studied previously in single semiconductor quantum dots strongly coupled to a reservoir [25]. Also, DCS had been previously demonstrated in metallic systems, where $t$ cannot be tuned [33, 34]. In time, DCS of a semiconductor double quantum dot proved more than an incremental step. Alex Johnson and others in the group combined DCS with pulsed-gating techniques to demonstrate energy-spectroscopy [35] of an isolated double quantum dot and single-spin detection via spin-to-charge conversion. Today, DCS is a a robust readout scheme for a two-electron-spin qubit [36]. The method of charge sensing by standard lock-in detection of QPC sensor conductance used in Ch. 4 is now called dc-QPC charge sensing, to contrast it with the recently developed rf-QPC technique [37] that enables charge detection on microsecond time scales.

## 1.6 Current Noise

### 1.6.1 Background

In electronics, the term noise refers quite generally to the temporal fluctuations of currents and voltages about a time average [38], as illustrated in Fig. 1.5(a). In compliance with the

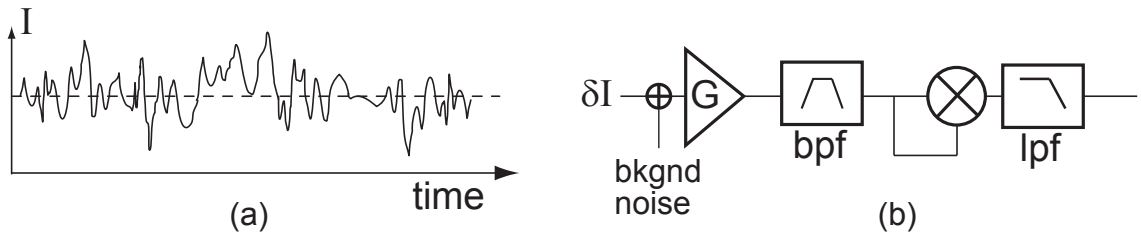


Figure 1.5: (a) In electronics, noise typically refers the temporal fluctuation of currents or voltages about a time-average (dashed line). (b) Block diagram of a basic noise measurement system. The noise signal is amplified, filtered over a bandwidth $\Delta_f$, squared, and integrated over $\tau_{\rm int}$. The statistical error in the extraction of $S_I$ is $(S_I + S_{\rm bkg})/\sqrt{\Delta_f \tau_{\rm int}}$, with $S_{\rm bkg}$ the spectral density of the input-referred noise background.

colloquial use of this term (synonymous with annoyance), many types of electronic noise are undesirable: examples include amplifier noise, interference pickup from radio stations and the 60 Hz power grid, and $1/f$ and telegraphic-like resistance fluctuations arising from dynamic charge traps in substrates.

In contrast to these examples, the intrinsic noise arising from the fundamental transport mechanism in a mesoscopic conductor can be an interesting signal to us [39]. Two types of current noise relevant to this thesis are Johnson[4] and shot noise. Johnson noise, defined as current noise at zero bias, is a practical electron thermometer [40]. Shot noise, arising at finite bias from stochastic partitioning of the incident electron flux, reveals transmission properties not captured by dc transport.

While on paper [Fig. 1.5(b)] noise measurements appear as straightforward as dc transport measurements by lock-in detection, in practice they are more involved because large bandwidths (tens to hundreds of kilohertz) and long integration times (seconds to minutes) are needed to resolve the noise spectral density $S_I$ of currents of order picoamps to nanoamps. The higher the bandwidth, the more susceptibility to interference. The longer the integration time, the more experimental drift matters. The technical aspects of noise measurement are discussed in detail in Ch. 5 presenting a two-channel noise measurement

[4]Often called thermal noise and Johnson-Nyquist noise.

system [41].

Given the added complexity, it is important to ask: *when is a noise measurement useful?* Example cases include: noise thermometry [40, 42], characterization of multi-mode mode transmission [43, 44, 45], investigation of interactions [39, 46], detection of quasiparticle charge [47, 48, 49, 50] and investigation of two-particle interference [51, 52]. Noise experiments presented in Chs. 6 to 9 are examples of the first three. The last two uses of noise measurements remain longer-term goals for the group.

### 1.6.2 Noise within the Landauer-Büttiker framework

We briefly discuss current noise within L-B [53, 39], which is useful for discussing the noise experiments ahead. For a two-terminal multi-mode conductor[5],

$$S_I = 4k_BTg + 2e^2/h \sum_n \tau_n(1-\tau_n)\left[eV_{\rm sd}/\tanh(eV_{\rm sd}/2k_BT) - 2k_BT\right],$$

where $g = e^2/h \times \sum_n \tau_n$ is the conductance and $\tau_n$ corresponds to eigenvalues of $S_{ds}^\dagger S_{ds}$. The first term describes thermal noise consistent with the fluctuation-dissipation theorem, and is the only term surviving at $V_{\rm sd} = 0$. The second term originates from partitioning of the electron flux by partial transmission (Fig. 1.6). Partition noise, as this term is called, shows a quadratic-to linear crossover on a bias scale[6] $e|V_{\rm sd}| \sim 2k_BT$. The Fano factor $\mathcal{F}$, which gives the asymptotic slope of $S_I(2eI)$ at high bias, is given by $\mathcal{F} = \sum_n \tau_n(1-\tau_n)/\sum_n \tau_n$. For example, $\mathcal{F} = 1/3$ in disordered metals and $1/4$ in multi-mode chaotic quantum dots [39]. Note that $\mathcal{F}$ gives information about the $\tau_n$ distribution that is different from the sum given by $g$.

L-B theory [53, 39] for conductors with arbitrary number of terminals makes two predictions resulting from quantum indistinguishability of electrons. First, finite-bias current

[5]We assume energy-independent transmission.

[6]This crossover is the basis of a novel primary thermometer [42].

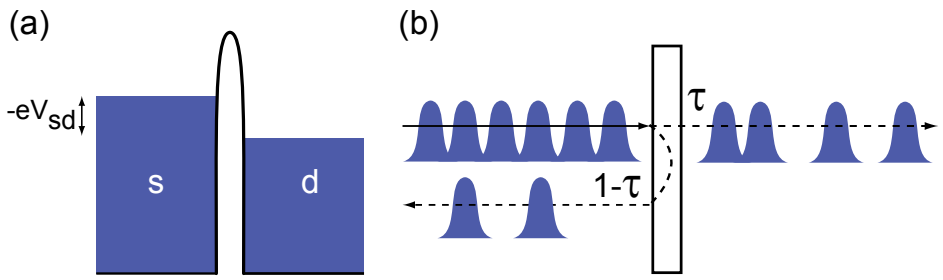


Figure 1.6: Illustration of electron partitioning in the limit of zero temperature. A finite bias across a conductor produces a noiseless incident electron flux which is partitioned at the conductor, producing noisy net current at both terminals.

noise at any terminal is sub-Poissonian ($\mathcal{F} < 1$). Second, the current noise cross correlation between any two terminals is always negative, regardless of bias conditions. The violation of any of these two properties is a hallmark of strong interactions [46].

### 1.6.3 Shot-noise signatures of 0.7 structure and spin in QPCs

*Experiment:* Chapter 6 presents an investigation [54, 55] of shot noise in QPCs as a function of source-drain bias, gate voltage, and in-plane magnetic field $B_{\|}$. The main physics result of this experiment is the observation at $B_{\|} = 0$ of a suppression of shot noise associated with the 0.7 structure in dc transport [56]. This suppression is relative to L-B with degenerate transmission ($\tau_1 = \tau_2$) through the two modes of the lowest QPC sub-band. With increasing field, this suppression evolves smoothly into the shot-noise signature expected for spin-lifted transmission degeneracy $\tau_1 = \tau_\uparrow \neq \tau_2 = \tau_\downarrow$. Comparison to the phenomenological Reilly model [57] that assumes a density-dependent mode splitting yields quantitative agreement, providing further evidence that QPC transport just below the $2e^2/h$ conductance plateau at $B_{\|} = 0$ involves two modes with unequal transmission.

*Relevance:* While neither the first measurement of QPC shot noise [58, 59], nor the first investigation of the shot-noise signature of the 0.7 anomaly [60], this experiment significantly reduced measurement error bars and most clearly showed the smooth evolution of the noise suppression with $B_{\|}$. This quickly motivated comparisons to several theo-

retical models of the 0.7 structure. Using a generalized single-impurity Anderson model motivated by density-functional calculations that suggest a quasi-bound state [61], Ref. [62] found quantitative agreement with the $B_{\|}$-dependent noise signatures observed. Modeling screening of Coulomb interaction in the QPC, Ref. [63] qualitatively reproduced the observed $B_{\|}$-dependent noise signatures. Meanwhile, density-functional calculations [64] including exchange and correlation effects found density-dependent splitting, justifying the phenomenological model to which our noise data was first compared. It thus seems that the observed shot-noise suppression may not quite rule out any of these competing theories for this long-standing open problem in mesoscopic physics that is the 0.7 structure.

### 1.6.4 Fano factor in graphene nanostructures

*Experiment:* Chapter 9 reports an experimental investigation [65] of shot noise in graphene nanostructures, including globally gated sheets and a *p-n* junction. The main result is the observation that $\mathcal{F}$ is largely independent of carrier type, carrier density, sample geometry, and even the presence of a junction.

*Relevance:* This work is, to my knowledge, the first investigation of shot noise in graphene nanostructures. The observed noise signature contrasts with the prediction of a sharply density-dependent $\mathcal{F}$ by L-B-type calculations for ballistic graphene, as well as with theory for ballistic *p-n* junctions. These results are in partial agreement with theory for charge-puddle disorder, which predicts a robust $\mathcal{F} \sim 0.30$ independent of carrier type and density over a wide range of device aspect ratio. However, this value is $\sim 20\%$ lower than the value observed in the experiment.

### 1.6.5 Current noise in the Coulomb blockade regime

*Experiments:* Chapters 7 and 8 investigate shot noise in quantum dot structures operating in the CB regime. The first experiment [66] reports gate-controlled sign reversal of the cross correlation of current fluctuations in a capacitively-coupled double quantum dot. The

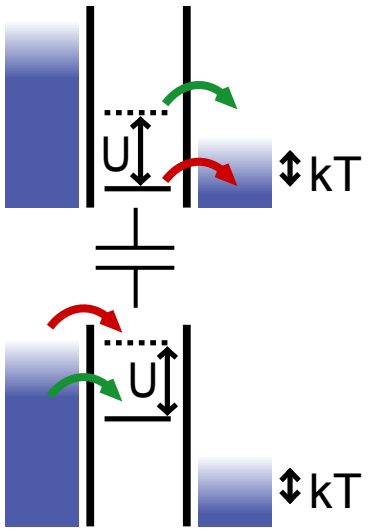


Figure 1.7: Level diagrams for a configuration of bias and gate voltage at which positive cross correlation between temporal current fluctuations in two capacitively coupled quantum dots is observed. The interdot mutual charging energy $U$ makes tunneling-out the top dot and tunneling-in to the bottom dot sensitive to the charge state in the other dot. These two tunneling processes, each the critical step for transport in the corresponding dot, facilitate each other. This cooperation leads to positive noise cross correlation.

observed gate-dependent cross correlation is reproduced by a sequential-tunneling model that includes interdot Coulomb interaction and can be understood from an intuitive picture of mutual charge-state-dependent tunneling (Fig. 1.7).

The second experiment [67] investigates noise correlations in a single quantum dot with two or three leads. The main result is the observation of super-Poissonian noise auto-correlation and positive noise cross correlation consistent with dynamical channel blockade. Shown schematically in Fig. 1.8 for the two-lead configuration, this effect results from finite-bias transport through multiple quantum levels when CB is only partially lifted. An electron tunneling into the long-lived red level temporarily blocks sequential tunneling through the upper levels. These periods of silence in between bursts of current leads to super-Poissonian auto-correlation and positive cross correlation.

*Relevance:* The main result of these two experiments is the observation of controllable shot-noise signatures unambiguously resulting from strong Coulomb interaction. These ex-

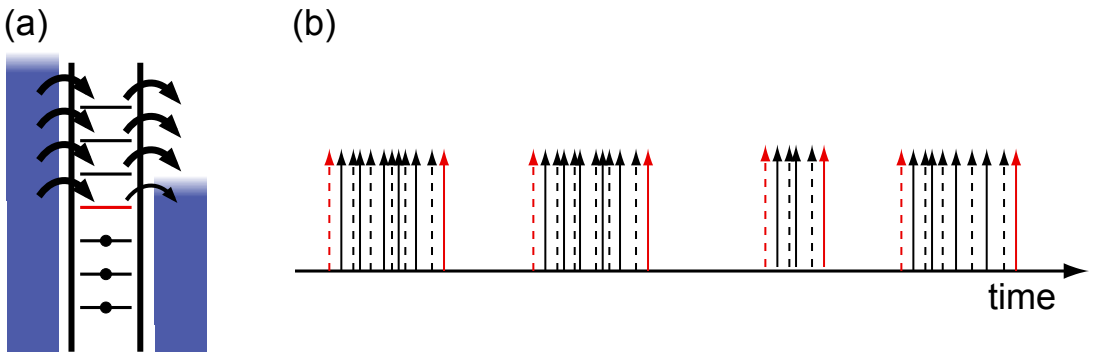


Figure 1.8: (a) Energy level diagram showing a bias and gate configuration at which super-Poissonian noise is observed in a single quantum dot. (b) Tunneling-in (solid red arrow) of an electron to the lowest energy level in the bias window temporarily blocks transport trough the upper three levels. When the electron tunnels-out (dashed red arrow) into the right reservoir, sequential tunneling through the upper levels resumes temporarily. Transport is again blocked when tunneling-in occurs to the red level.

periments distill the basic mechanisms by which super-Poissonian noise and positive noise correlations arise in systems where localized states occur naturally and uncontrollably. Examples of such systems are metal-semiconductor field effect transistors [68], self-assembled stacked quantum dots [69] and tunnel barriers [70, 71].

# Chapter 2

# Technology enabling mesoscopic electronics

Mesoscopic electronics is enabled by three technological advances that allow the inequalities $\lambda_F \sim L < Ł_\phi(T)$ and $E_C > k_B T$ to hold in experimentally accessible regimes. Here, $\lambda_F$ is the electron (Fermi) wavelength, $L$ the device feature size, $Ł_\phi(T)$ the electron phase coherence length, $E_C$ the electrostatic charging energy, and $T$ the temperature.

The first advance is the production of sub-Kelvin temperatures using refrigerators based on liquefied Helium. Most notable are the $^3$He-$^4$He dilution and $^3$He refrigerators reaching base temperatures $T \sim 50$ and 300 mK, respectively [72, 40]. The second is electron-beam lithography (e-beam), which makes possible the patterning of features of order tens of nanometers. The third is the development and discovery of conductors with density low enough for $\lambda_F$ to reach some hundred nanometers, and clean enough that $L_\phi(T)$ can become considerably longer than $\lambda_F$ at cryogenic temperatures.

In this chapter we discuss the 2D conductors on which the nanostructures investigated in this thesis are patterned. These are the GaAs/AlGaAs electron gas (2DEG) and graphene. Many characteristics set these two systems apart. For one, 2DEG is fabricated in ultra high-vacuum molecular beam epitaxy chambers, while graphene is exfoliated from thicker graphite using Scotch tape! 2DEG is a metallic gas of essentially free electrons with a renormalized mass. On the other hand, graphene is a zero-gap semi-metal whose electrons and holes are massless and chiral, and thus act (at least in theory) as Dirac-like particles

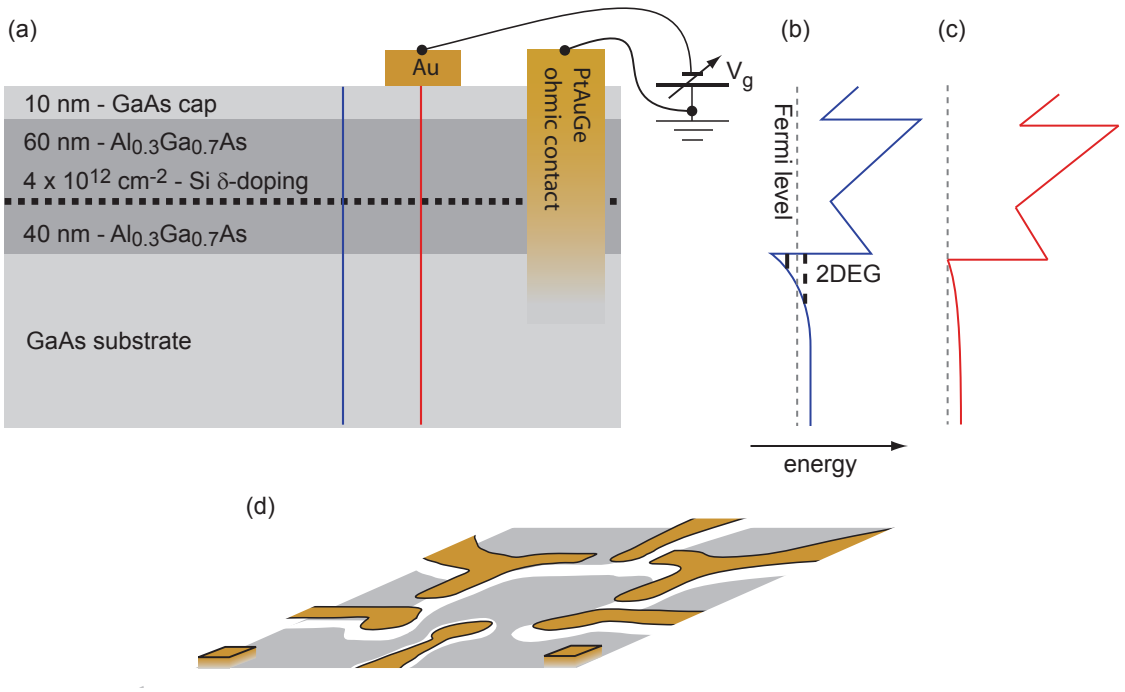


Figure 2.1: (a) Schematic of GaAs/AlGaAs heterostructure. The specific parameters shown correspond to wafer 010219B, grown by Micah Hanson and Arthur Gossard at UCSB, and from which the device measured in Ch. 4 was made. Also shown are the top metallic gates (Au) patterned by electron-beam lithography and Pt/Au/Ge ohmic contacts annealed through the surface to make direct contact to the 2DEG. (b) Band diagram showing the variation of the conduction band edge as a function of depth. The 2DEG occupies the lowest subband (thick solid line) in the triangular well formed at the GaAs/AlGaAs interface. The second subband (thick dashed line), 150 meV above the first, is unoccupied at cryogenic temperatures. (c) $V_g \sim -0.3$ V applied to a top gate tilts the conduction band edge and locally depletes the 2DEG. (d) A 3D schematic of a gate-defined quantum dot coupled to two regions of 2DEG which serve as source and drain electron reservoirs. Ohmics contact the reservoirs.

rather than as free electrons.

## 2.1 GaAs/AlGaAs 2DEG

The fabrication of heterostruture materials by molecular beam epitaxy has progressed tremendously since the seventies [73]. Today, the 2D electron gas confined to the interface between GaAs and $Al_xGa_{1-x}As$ reaches a mobility $\mu \sim 30 \times 10^6$ cm$^2$/Vs. This figure translates into an electron mean free path $\ell \sim 300$ $\mu$m, the distance an electron travels on average between its last and next collision with a lattice imperfection.

A schematic of a heterostructure used in this thesis (Ch. 4) is shown in Fig. 2.1. It reveals one of the three main features that make 2DEG a high quality conductor. This is the physical separation of the conduction channel from the donor layer. The mobile electrons populate the lowest subband of a triangular potential right at the GaAs/AlGaAs interface, while the ionized Si donors lie on a thin layer some 50 nm away. The extremely clean growth conditions, and the nearly identical lattice constants in GaAs and AlGaAs also contribute to the high mobility of 2DEG.

Nanostructures are electrostatically defined in 2DEG by applying negative voltages $V_g$ (relative to the 2DEG) to metallic (Au) gates patterned on the top surface of the heterostructure using e-beam. $V_g \sim -0.3$ V locally depletes the 2DEG $\sim 100$ nm underneath, producing a shadow in the 2DEG that electrons are forbidden to enter. More negative voltages (up to $V_g \sim -3$ V, as limited by the onset of conduction through the Schottky barrier between the gates and the GaAs cap) can be applied to controllably extend the depletion region. In this way, electron puddles (quantum dots) or point-like constrictions (QPCs) can be defined with controlled coupling to the 2DEG regions serving as electron reservoirs. Ohmic contacts to the reservoirs, so called because good contacts act simply like resistors in the $\sim 0.1 - 1$ k$\Omega$ range, are made by annealing Pt/Au/Ge square pads into the wafer and contacting the 2DEG directly. The reader interested in the technique (and subtle art) of making good ohmic contacts is directed to Ref. [74] for a thorough discussion.

## 2.2 Graphene

Graphene [75] is a zero-gap semi-metal consisting of a 2D honeycomb lattice of carbon exactly one atomic layer thick. The honeycomb lattice consists of two identical (but displaced) carbon sublattices, giving graphene a valley degeneracy of 2 and a linear dispersion about two inequivalent Dirac points where valence and conduction bands meet [76]. Eigenstates in graphene have wavefunctions whose relative weighting in the two sublattices can

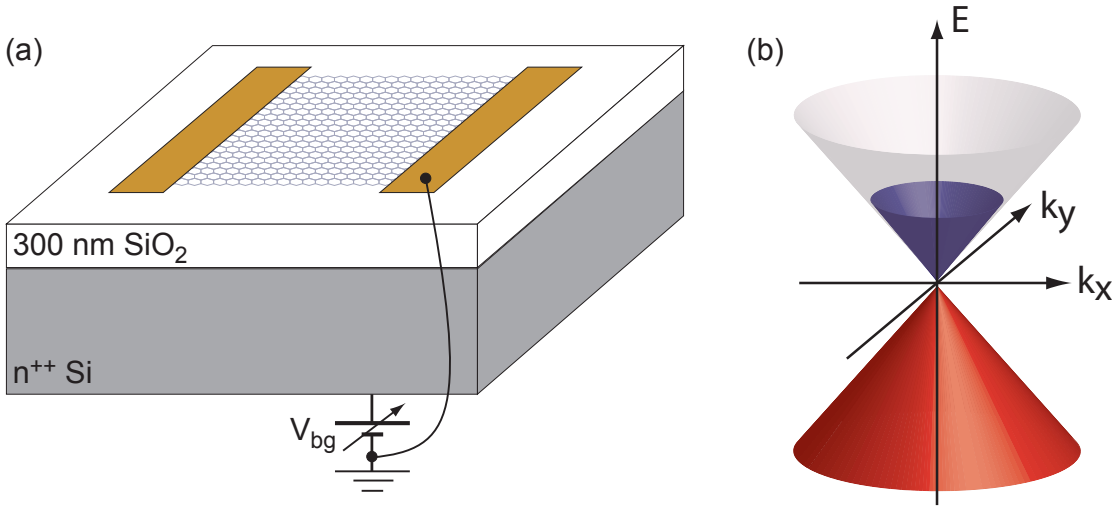


Figure 2.2: (a) Schematic diagram of the graphene structures used for noise experiments presented in Ch. 9. The carrier type and density is globally controlled with a voltage $V_{\rm bg}$ applied to the back gate. (b) The linear dispersion of graphene near the Dirac points where the valence (red) and conduction (blue) bands meet. The Fermi level in this schematic corresponds to positive $V_{\rm bg}$ (relative to the $V_{\rm bg}$-value at the charge-neutrality point, which can be non-zero due to chemical doping of the sample).

be mapped onto a pseudospin. Within one valley, the pseudospin of electrons (holes) is aligned (anti-aligned) with the momentum $\overrightarrow{k}$ (relative to the Dirac Point), and viceversa for the other valley. These electronic properties lead to novel transport phenomena, most notably anomalous conductance quantization in the quantum Hall regime [77, 78].

Graphene is clean enough to show quantum Hall signatures with $B_\perp \sim 4$ T at $T = 4$ K and with $B_\perp = 45$ T at room temperature [79]. Currently, the typical carrier mobility in graphene $\mu \sim 5 \times 10^3$ cm$^2$/Vs [80] pales in comparison with 2DEG. However, this mobility compares favorably with Si, $\mu \sim 1 \times 10^3$ cm$^2$/Vs (lightly doped $n$-type) [31]. At the time of writing, graphene is touted as a candidate material for a post-silicon electronics. Only time, and lots more research, will tell.

In contrast to 2DEG, graphene is not typically grown from the bottom-up. While such methods do exist (commonly thermal decomposition of silicon carbide [81]), the most popular fabrication technique is the *Scotch-tape method* [82]. This method is used to fabricate

all the graphene structures measured in Chs. 9 and 10. The name derives from the fact that the initial fabrication step is the mechanical exfoliation of thin graphitic layers from highly-oriented pyrolitic graphite (HOPG) using tape (and tweezers). These thin layers are then deposited on a heavily-doped Si substrate capped with 300 nm of $SiO_2$. This oxide thickness leads to an optical interference that allows a trained eye to identify single-layer graphene through a microscope with magnification $\times 150$.

Graphite flakes identified as possible single-layers are next contacted with Ti/Au (typically 5/40 nm) leads patterned using e-beam. The lead pattern defines some of the graphene structure dimensions, and the sheet edges define the rest. It is important to note that the termination at these edges (be them armchair, zigzag, etc.) is never known. Neither is the exact orientation of the graphene lattice. A schematic diagram of the graphene devices used for noise experiments in Ch. 9 is shown in Fig. 2.2.

Like 2DEG, graphene can be gated using the electric field effect [82]. The carrier type and density $n_s$ can be globally controlled from nominally zero up to $|n_s| \sim 10^{13}$ cm$^{-2}$ by applying a voltage $V_{\rm bg}$ on the back gate relative to one of the terminals. Scanning probe experiments [83] show that charge neutrality corresponds more to $n$- and $p$-type puddles $\sim 150$ nm in extent rather than to homogeneous charge neutrality. Local control of carrier density has recently been demonstrated using a combination of the global back gate and a local top gate [84, 85, 86]. The top-gating procedure used in our lab will be described in detail in Ch. 10.

## 2.3 Comparison

The following table provides a list of key properties of 2D systems, and their corresponding typical values in bulk 2DEG and graphene. For 2DEG, a typical sheet density $n_{\rm s} = 2 \times 10^{11}$ cm$^{-2}$ and $\mu = 10^6$ cm$^2$/Vs are assumed. For graphene, a carrier density $|n_{\rm s}| = 1.4 \times 10^{12}$ cm$^{-2}$, corresponding to $V_{\rm bg} = \pm 20$ V with respect to the charge-neutrality point,

and a typical $\mu = 5 \times 10^3$ cm$^2$/Vs are used. The listed properties will be relevant to the experiments presented in the following chapters.

| Property | Symbol | Formula | | Value | | Units |
|---|---|---|---|---|---|---|
| | | 2DEG | G | 2DEG | G | |
| Effective mass | $m_*$ | | | 0.067 | 0 | $m_e$ |
| Spin degeneracy | $g_\mathrm{s}$ | | | 2 | 2 | |
| Valley degeneracy | $g_\mathrm{v}$ | | | 1 | 2 | |
| Landé g-factor | $g^*$ | | | -0.44 | 2 | |
| Fermi wave vector | $k_\mathrm{F}$ | $(4\pi n_s/g_\mathrm{s}g_\mathrm{v})^{1/2}$ | | 0.1 | 0.2 | 1/nm |
| Fermi wavelength | $\lambda_\mathrm{F}$ | $2\pi/k_\mathrm{F}$ | | 56 | 30 | nm |
| Fermi energy | $E_\mathrm{F}$ | $(\hbar k_\mathrm{F})^2/2m^*$ | $\hbar k_\mathrm{F}\nu$ | 7 | 140 | meV |
| Fermi velocity | $v_\mathrm{F}$ | $\hbar k_\mathrm{F}/m^*$ | $\nu$ | $1.9 \times 10^5$ | $10^6$ | m/s |
| Density of states | $\rho(E_\mathrm{F})$ | $g_\mathrm{s}g_\mathrm{v}m^*/2\pi\hbar^2$ | $g_\mathrm{s}g_\mathrm{v}E_\mathrm{F}/2\pi\hbar^2\nu^2$ | 280 | 21 | $1/\mu$m$^2$meV |
| Conductivity | $\sigma$ | $n_s e\mu$ | | 860 | 30 | $e^2/h$ |
| Diffusion constant | $D$ | $\sigma/e^2\rho(E_\mathrm{F})$ | | $7 \times 10^4$ | 350 | cm$^2$/s |
| Mean free path | $\ell$ | $2D/v_\mathrm{F}$ | | $10^4$ | 70 | nm |
| Scattering time | $\tau_\mathrm{e}$ | $\ell/v_\mathrm{F}$ | | 40 | .07 | ps |
| Zeeman energy | $E_\mathrm{Z}$ | $g^*\mu_\mathrm{B}B$ | | 25.5 | 116 | $\mu$eV/T |

Table 2.1: Typical parameters for bulk GaAs/AlGaAs 2DEG and for graphene (G). Here, $m_e = 9.11 \times 10^{-31}$ kg is the free-electron mass, and $\nu = 10^6$ m/s is the energy-independent Fermi velocity in graphene.

# Chapter 3

# Photocurrent, rectification and magnetic field symmetry of induced current through quantum dots

L. DiCarlo, C. M. Marcus
*Department of Physics, Harvard University, Cambridge, Massachusetts 02138*
J. S. Harris, Jr.
*Department of Electrical Engineering, Stanford University, Stanford, California 94305*

We report mesoscopic dc current generation in an open chaotic quantum dot with ac excitation applied to one of the shape-defining gates. For excitation frequencies large compared to the inverse dwell time of electrons in the dot (i.e., GHz), we find mesoscopic fluctuations of induced current that are *asymmetric* in the applied perpendicular magnetic field, as predicted by recent theory. Conductance, measured simultaneously, is found to be symmetric in field. In the adiabatic (i.e., MHz) regime, in contrast, the induced current is always symmetric in field, suggesting its origin is mesoscopic rectification.[1]

[1]This chapter is adapted with permission from Phys. Rev. Lett. **91**, 246804 (2003). © (2003) by the American Physical Society.

## 3.1 Introduction

The study of phase-coherent electron transport in systems with rapidly time-varying potentials significantly extends the domain of mesoscopic physics, and is likely to be important in quantum information processing in the solid state, where gate operations must be fast compared to decoherence rates. Three regimes of transport where quantum interference effects play an important role may be identified: dc transport with static potentials, exhibiting coherence effects such as universal conductance fluctuations (UCF) and weak localization; adiabatic transport, showing mesoscopic rectification and charge pumping [87, 88, 89, 17, 19, 90, 21]; and high-frequency transport, where photovoltaic effects [91, 92, 93, 94, 95, 96, 97, 98] and decoherence from a fluctuating electromagnetic environment have been studied [99, 100, 101, 102]. Recently, theory connecting these regimes in quantum dots has appeared [103, 22, 104, 13, 105], with most predicted effects remaining unexplored experimentally.

In this chapter, we compare dc currents induced by adiabatic and nonadiabatic sinusoidal modulation of the voltage on one of the confining gates of an open GaAs/AlGaAs quantum dot. Motivated by recent theory [19, 21, 22], we pay particular attention to the symmetry of the induced dc current as a function of perpendicular magnetic field, $B_\perp$. For adiabatic frequencies ($\omega \ll \tau_d^{-1}$, where $\tau_d$ is the inverse dwell time of electrons in the dot) mesoscopic fluctuations (about a zero average) of induced current are always found to be symmetric in $B_\perp$. As discussed in [106, 21], this suggests *rectification*—due to coupling of the gate voltage to the reservoirs combined with gate-dependent conductance—as the principal source of induced current in this regime. On the other hand, for gate-voltage modulation at GHz frequencies ($\omega \gtrsim \tau_d^{-1}$), the induced dc current may be either predominantly symmetric or completely asymmetric in $B_\perp$, depending on the particular frequency.

We interpret these results as showing competing mechanisms of induced mesoscopic current in the GHz regime, with photocurrent producing a signal asymmetric in $B_\perp$ and

rectification producing a signal symmetric in $B_\perp$. Full asymmetry of photocurrent reflects the broken time-reversal symmetry due to the ac excitation. In contrast, rectification arises from a modulated conductance, which remains predominantly symmetric in field even when an ac excitation is present. Which effect dominates depends strongly on the frequency of the modulation. We thus establish field symmetry as an experimental tool for separating these different physical effects. This allows us to study, for instance, how rectification and photocurrent separately depend on the amplitude of the applied ac modulation.

## 3.2 Device

The quantum dot investigated was formed by electrostatic gates 90 nm above the two-dimensional electron gas (2DEG) in a GaAs/AlGaAs heterostructure, and has an area $A \sim 0.7\,\mu\mathrm{m}^2$, accounting for $\sim$ 50 nm depletion at the gate edge. The bulk density of the 2DEG was $2 \times 10^{11}$ cm$^{-2}$ and the mobility $1.4 \times 10^5$ cm$^2$/Vs, giving a bulk mean free path $\sim 1.5$ $\mu$m. Ohmic contact resistances were on the order of 350 $\Omega$. Measurements are presented for the case of one fully conducting (spin degenerate) mode per lead, which gives an average dot conductance $\langle g \rangle \sim e^2/h$. Relevant time scales include the dot crossing time $\tau_{\mathrm{cross}} \sim \sqrt{A}/v_F \sim 4$ ps and dwell time within the dot $\tau_d = h/2\Delta \sim 0.2$ ns for single-mode leads ($\Delta = 2\pi\hbar^2/m^*A \sim 10$ $\mu$eV is the quantum level spacing, $v_F$ is the Fermi velocity and $m^*$ the effective electron mass).

## 3.3 Methods

The induced dc current through the dot was measured in a dilution refrigerator via 300 $\Omega$ leads, while two semirigid 50 $\Omega$ coaxial lines allowed ac excitation to be coupled from the high-frequency source (Wiltron 6769B) to either of two gates of the dot over a range 10 MHz to 20 GHz. A room temperature bias tee enabled ac and dc voltage to be simultaneously applied to the chosen gate. With coaxial lines attached, the base electron temperature,

where all measurements were carried out, was $\sim 200$ mK, determined from UCF amplitude [100] and Coulomb blockade peak widths [3]. The ac excitation was chopped at 153 Hz by a square pulse of variable duty cycle, $p$ (given as a percentage). The induced current was amplified with an ac-coupled Ithaco 1211 current amplifier (nominal input impedance 2 k$\Omega$) and lock-in detected. Conductance was simultaneously measured by applying a 17 Hz, 2 $\mu V_{\rm rms}$ sinusoidal voltage bias across the dot. Output of the same current amplifier was then detected using a second lock-in at 17 Hz. The measured conductance $g_p$ was found to be a simple weighted average of the conductance with excitation on ($g_{\rm on}$) and off ($g_{\rm off}$), $g_p \approx p g_{\rm on} + (1-p) g_{\rm off}$, as seen in Fig. 3.1(d).

## 3.4 Mesoscopic fluctuations as a function of $B_\perp$

Figures 3.1(a) and 3.1(b) show dot conductance $g_{50}(\pm B_\perp)$ and induced current $I(\pm B_\perp)$, with $p = 50\%$ duty cycle, as a function of perpendicular field, $B_\perp$, for applied frequencies of 10 MHz ($\omega\tau_d \sim .01$) and 5.56 GHz ($\omega\tau_d \sim 7$). Dot conductances are in all cases found to be symmetric in $B_\perp$, and show the expected weak localization dip at $B_\perp = 0$ and UCF. The induced current with 10 MHz excitation is also symmetric in field. In contrast, the induced current for 5.56 GHz applied to the gate is found to be fully asymmetric in field. This is evident in the traces in Fig. 3.1(b). The difference between induced current at 10 MHz and 5.56 GHz is seen most clearly by looking at the correlation between induced currents at $\pm B_\perp$, defined by $C_I(B_\perp) = (\delta I(B_\perp)\delta I(-B_\perp))/\langle \delta I(B_\perp)^2 \rangle_{B_\perp}$. The brackets denote an average over the measured magnetic field range, and $\delta I$ is the deviation of the current from its average value over this range. For 10 MHz, $C_I$ is non-negative for all magnetic field values, whereas for 5.56 GHz it changes sign numerous times.

The correlation field scales of mesoscopic fluctuations of induced current and conductance for 10 MHz and 5.56 GHz are roughly equivalent, $\sim 1.5$ mT, as determined from slopes of log-power spectra [107]. Induced dc current at 10 MHz (5.56 GHz) has roughly

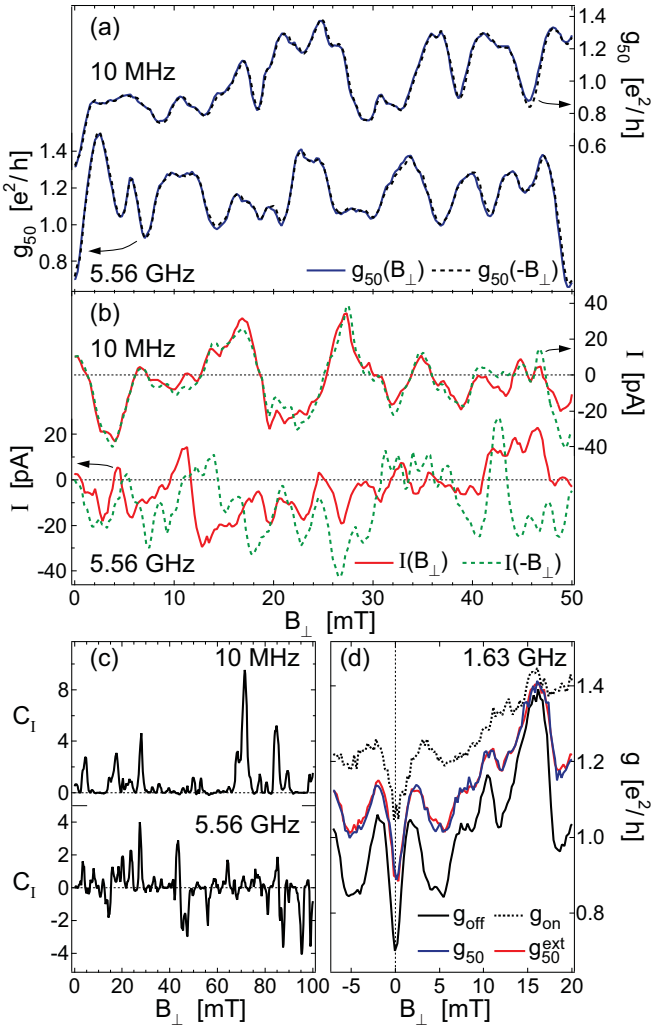


Figure 3.1: (a) Conductance $g_{50}(\pm B_\perp)$ as a function of perpendicular magnetic field $B_\perp$, for 200 nW of incident radiation at 10 MHz (top) and 370 nW at 5.56 GHz (bottom). (b) Induced dc currents $I(\pm B_\perp)$, measured simultaneously with the conductance traces in (a). (c) Cross correlation $C_I(B_\perp)$ (see text) of induced current fluctuations at $\pm B_\perp$. Correlation is everywhere nonnegative for 10 MHz, but both positive and negative for 5.56 GHz. (d) Comparison of measured dot conductance with 50% duty cycle, $g_{50}$ (blue), and extracted trace $g_{50}^{\rm ext} = (g_{\rm off} + g_{\rm on})/2$ (red), an average of traces with ac excitation off, $g_{\rm off}$ (black), and excitation on, $g_{\rm on}$ (dashed). Traces at different frequencies were made for different dot shape configurations, and hence are uncorrelated.

zero average and rms fluctuation amplitude of $\sim 20$ (13) pA, corresponding to $\sim 12$ (.015) electrons per cycle. These values are obtained for ac gate voltages of 6.4 ($\sim 12$) $\mathrm{mV_{rms}}$, comparable to the measured dc gate-voltage correlation scale, $\sim 10$ mV. (The ac gate voltage at 10 MHz was calibrated and found to be equal to the voltage applied at the top

of the cryostat; the ac gate voltage at 5.56 GHz could not be easily calibrated and instead was estimated by locating the inflection of the curve of induced dc current versus incident power, as seen for instance in Fig. 3.3, and comparing to theory [22].)

## 3.5 Mesoscopic fluctuations as a function of gate voltage

Figure 3.2 shows fluctuations of conductance and induced current as a function of the dc gate voltage, $V_g^{dc}$, on a shape distorting gate of the dot—the same gate to which the ac excitation is applied—at opposite magnetic field values, ±50 mT. The conductance traces $g(V_g^{dc})$ in Fig. 3.2(a) are nearly identical at ±50 mT, for both 10 MHz and 2.4 GHz excitations. Induced current fluctuations, shown in Fig. 3.2(b), are symmetric at 10 MHz, but are not symmetric for 2.4 GHz.

Using the *same* gate both to drive the dot at ac and change dot shape as a slowly swept parameter allows the induced dc current to be compared to a simple model of rectification [106, 21] applicable in the adiabatic limit. The model takes the measured $g(V_g^{dc})$ as input, and assumes that the ac part of the total gate voltage, $V_g(t) = V_g^{dc} + V_g^{ac}\sin(\omega t)$, couples to the source and drain reservoirs of the dot, giving rise to a (possibly phase shifted) drain-source voltage, $V_{ds}(t) = \alpha V_g^{ac}\sin(\omega t + \phi)$, with $\alpha$ and $\phi$ as parameters. The dc rectification current resulting from $V_{ds}(t)$ and $g[V_g(t)]$ is given by

$$I_{\rm rect} = \frac{\omega}{2\pi}\int_0^{2\pi/\omega} \alpha V_g^{ac}\sin(\omega t+\phi)g[V_g(t)]dt. \tag{3.1}$$

For $V_g^{ac}$ much less than the gate-voltage correlation scale, $I_{\rm rect} \approx \frac{\alpha}{2}\cos(\phi)(V_g^{ac})^2\frac{dg}{dV_g}$ [21]. However, for the data in Fig. 3.2, $V_g^{ac} = 6.8$ mV(∼ 8 mV) for 10 MHz (2.4 GHz), which is not much smaller than the correlation voltage of 10 mV, so the full integral, Eq. (3.1), is used to model rectification. Figure 3.2(b) shows a comparison of measured currents and rectification currents calculated from Eq. (3.1), using the +50 mT data from Fig. 3.1(a) as input and values $\alpha = 7(6)\times 10^{-4}$ and $\phi = 0(0)$ for 10 MHz (2.4 GHz). For the 10 MHz

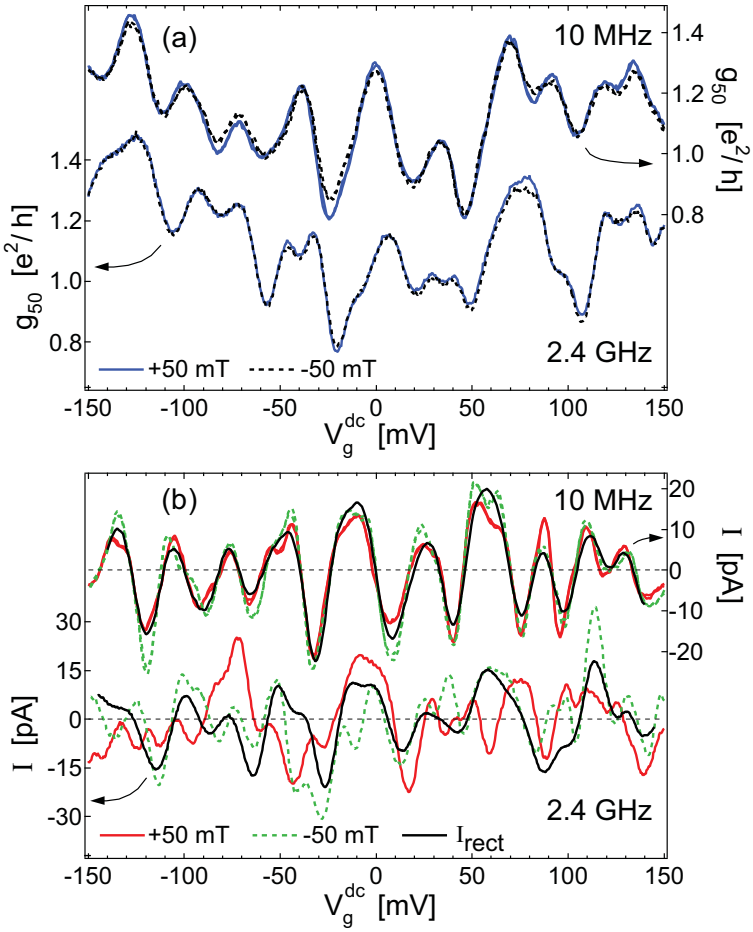


Figure 3.2: (a) Conductance as a function of the dc voltage on the same gate to which ac is coupled, at +50 mT and at −50 mT, for 115 nW of incident power at 10 MHz (top) and 45 nW at 2.4 GHz (bottom). Two traces are shown at each magnetic field for 10 MHz, revealing the degree of repeatability in the measurements. Traces at different frequencies were taken on different days. (b) Simultaneous measurements of induced dc currents. Currents calculated using the rectification model are also shown, in black, for numerical parameters given in the text.

data, the similarity between the model and the measured current suggests that rectification adequately accounts for the induced current. On the other hand, the induced dc current at 2.4 GHz ($\omega\tau_d \sim 3$) does not appear to be well described by the rectification model. This was to be expected: the lack of symmetry in field of the induced current already tells us that a rectification model that takes symmetric conductance as its input cannot describe the asymmetric current induced by this higher applied frequency.

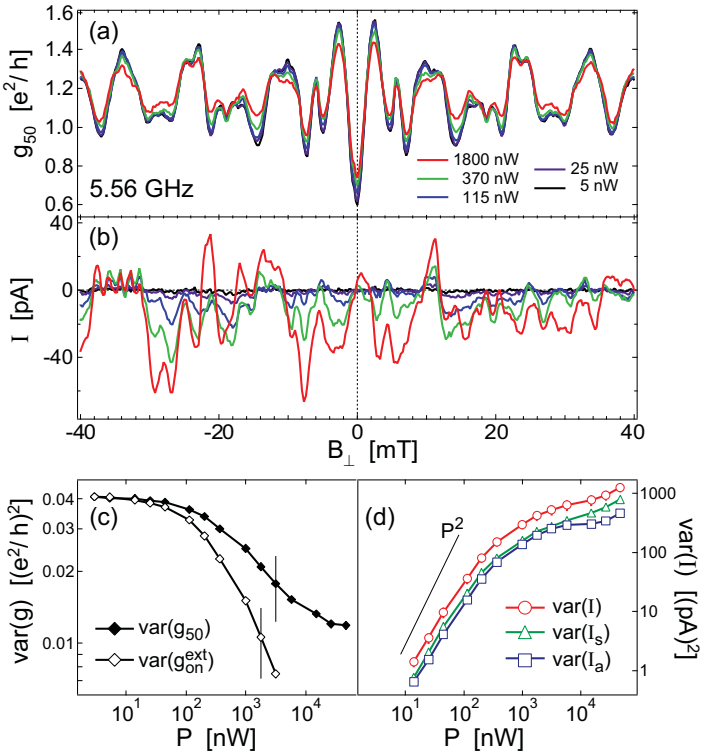


Figure 3.3: Magnetic field dependence of (a) conductance and (b) rf-induced dc current, for increasing levels of incident power $P$ at 5.56 GHz. Full sweeps spanned the $-100$ mT to $+100$ mT range. (c) Variance of the measured conductance $g_{50}$ and of the extracted on conductance $g_{\rm on}$, as a function of incident power. (d) Power dependence of the total induced dc current, and of its symmetric and antisymmetric components.

## 3.6 Microwave-power dependence of induced current

Conductance and induced current as a function of perpendicular field are shown in Figs. 3.3(a) and 3.3(b) for different levels of incident power $P$ at 5.56 GHz. Fluctuations in $g_{50}$ decrease with increasing $P$. In Fig. 3.3(c), we show the power dependence of the variance of the conductance. For high applied powers, the variance of conductance fluctuations is reduced to 1/4 of its zero-radiation level. This is expected, since during the fraction of time ($p = 50\%$) that the radiation is on, UCF should be fully suppressed at high power by a combination of shape averaging, dephasing without heating, and heating effects [101, 103]. Also shown in Fig. 3.3(c) is the variance of the extracted "on conductance," $g_{\rm on}^{\rm ext} = 2g_{50} - g_{\rm off}$, which we observe to decrease at a rate intermediate between $P^{-1/2}$ and $P^{-1}$ at high power. Theory [104] predicts a rate $P^{-1/2}$ in the absence of heating effects.

It is evident in Fig. 3.3(a) that no significant field asymmetry in conductance is observed, regardless of ac power applied. Recent theory [104] predicts that when applied frequency exceeds the temperature in the leads (which is the case here, $k_B T_e/h \sim 4$ GHz), dephasing will lead to field asymmetry in conductance. However, for our experimental conditions the predicted asymmetry is extremely small, smaller in fact than the asymmetry due to drift and noise in our set up (which, as seen in Figs. 3.1 and 3.2 is rather small.)

Figure 3.3(b) shows that mesoscopic fluctuations of the induced current at 5.56 GHz are fully asymmetric in field and increase in amplitude with increasing power. As a measure of this asymmetry, we compare the symmetric and antisymmetric components of current, $I_{\rm s}(B_\perp) = (I(B_\perp) + I(-B_\perp))/2$ and $I_{\rm a}(B_\perp) = (I(B_\perp) - I(-B_\perp))/2$. Figure 3.3(d) shows their variances and that of total induced current, calculated after subtracting a first order polynomial to $I(B_\perp)$ to account for a non-mesoscopic background present at the highest applied powers.

Variances of $I_{\rm s}$ and $I_{\rm a}$ are nearly equal, indicating that the current is fully asymmetric for all powers (except at the highest powers, discussed below). Variances of $I$, $I_{\rm s}$, and $I_{\rm a}$ increase at a rate approaching $P^2$ at the lowest powers, consistent with theory [22] for the weak pumping limit. The rate weakens at higher incident power, with a crossover near 300 nW, corresponding to an ac gate voltage comparable to the gate-voltage correlation scale.

In the nonadiabatic regime, the induced current is found to range between being predominantly symmetric and fully asymmetric in $B_\perp$, depending on the applied frequency. The degree of symmetry is also found to depend on the applied ac power, with greater symmetry found at higher power. This is illustrated in Fig. 3.4 for the case of ac gate voltage at 2.4 GHz. At low incident power the current is fully asymmetric, and the fluctuations have a correlation field $\sim 1$ mT. This is clearly observed in the top left inset, where we show the magnetic field dependence of the induced current for an incident power of 14 nW. At high power, var($I_{\rm a}$) saturates, leaving a predominantly symmetric signal (Fig. 3.4, lower right

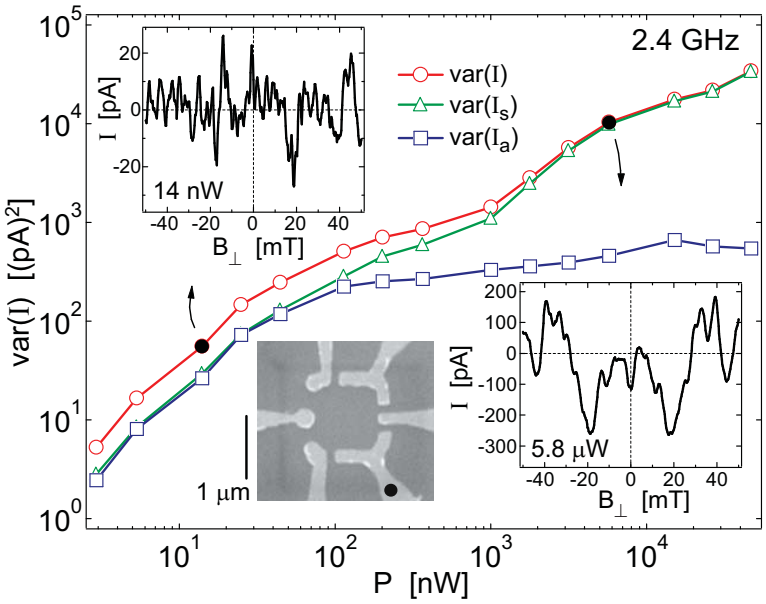


Figure 3.4: Variance of symmetric, antisymmetric and total current ($I_{\rm s}$, $I_{\rm a}$, $I$) as functions of incident power $P$ at 2.4 GHz. Upper left inset: Induced current as a function of magnetic field, $B_\perp$, for 14 nW power, showing asymmetric mesoscopic fluctuations with a correlation field $\sim$ 1 mT. Lower right inset: Induced current as a function of $B_\perp$ at 5.8 $\mu$W power, showing symmetric fluctuations with a correlation field $\sim$ 4 mT. An overall background in this trace was subtracted with a first order polynomial $a_o + a_1 B_\perp$. Lower left inset: Micrograph of device. Dot indicates gate to which ac is applied.

inset). The magnetic-field correlation scale increases to $\sim$ 4 mT at high power, suggesting enhanced dephasing presumably due to the ac voltages on the gate causing electron heating.

## 3.7 Conclusion and acknowledgements

In summary, we use magnetic field symmetry to distinguish mechanisms of induced dc current in response to ac gate voltages in a quantum dot. For lower frequencies, we find the induced current is symmetric in field, suggesting that mesoscopic rectification is responsible for the induced current in this regime. For higher frequencies (GHz), we find that the induced current can be fully asymmetric in field, suggesting instead that photocurrent can be the dominant source. The qualitative observation of these different regimes, distinguished by field symmetry, is consistent with recent theory [19, 21, 22].

We thank I. L. Aleiner, P. W. Brouwer, V. I. Falko, A. C. Johnson, and particularly

M. G. Vavilov for valuable discussion, and thank C. I. Duruöz, S. M. Patel, and S. W. Watson for experimental contributions. We acknowledge support from the NSF under DMR-0072777.

# Chapter 4

# Differential charge sensing and charge delocalization in a tunable double quantum dot

L. DiCarlo, H. J. Lynch, A. C. Johnson, L. I. Childress, K. Crockett, C. M. Marcus
*Department of Physics, Harvard University, Cambridge, Massachusetts 02138*
M. P. Hanson, A. C. Gossard
*Department of Materials, University of California, Santa Barbara, California 93106*

We report measurements of a tunable double quantum dot, operating in the quantum regime, with integrated local charge sensors. The spatial resolution of the sensors allows the charge distribution within the double dot system to be resolved at fixed total charge. We use this readout scheme to investigate charge delocalization as a function of temperature and strength of tunnel coupling, demonstrating that local charge sensing can be used to accurately determine the interdot coupling in the absence of transport.[1]

---

[1]This chapter is adapted with permission from Phys. Rev. Lett. **92**, 226801 (2004). © (2004) by the American Physical Society.

## 4.1 Introduction

Coupled semiconductor quantum dots have proved a fertile ground for exploring quantum states of electron charge and spin. These "artificial molecules" are a scalable technology with possible applications in information processing, both as classical switching elements [108, 109] or as charge or spin qubits [110]. Charge-state superpositions may be probed using tunnel-coupled quantum dots, which provide a tunable two-level system whose two key parameters, the bare detuning $\epsilon$ and tunnel coupling $t$ between two electronic charge states [111], can be controlled electrically.

In this chapter, we investigate experimentally a quantum two-level system, realized as left/right charge states in a gate-defined GaAs double quantum dot, using local electrostatic sensing (see Fig. 4.1). In the absence of tunneling, the states of the two-level system are denoted $(M+1, N)$ and $(M, N+1)$, where the pair of integers refers to the number of electrons on the left and right dots. For these two states, the total electron number is fixed, with a single excess charge moving from one dot to the other as a function of gate voltages. When the dots are tunnel coupled, the excess charge becomes delocalized and the right/left states hybridize into symmetric and antisymmetric states.

Local charge sensing is accomplished using integrated quantum point contacts (QPC's) positioned at opposite sides of the double dot. We present a model for charge sensing in a tunnel-coupled two-level system, and find excellent agreement with experiment. The model allows the sensing signals to be calibrated using temperature dependence and measurements of various capacitances. For significant tunnel coupling, $0.5k_BT_e \lesssim t < \Delta$ ($T_e$ is electron temperature, $\Delta$ is the single-particle level spacing of the individual dots), the tunnel coupling $t$ can be extracted quantitatively from the charge sensing signal, providing an improved method for measuring tunneling in quantum dot two-level systems compared to transport methods [111].

Charge sensing using a QPC was first demonstrated in Ref. [24], and has been used

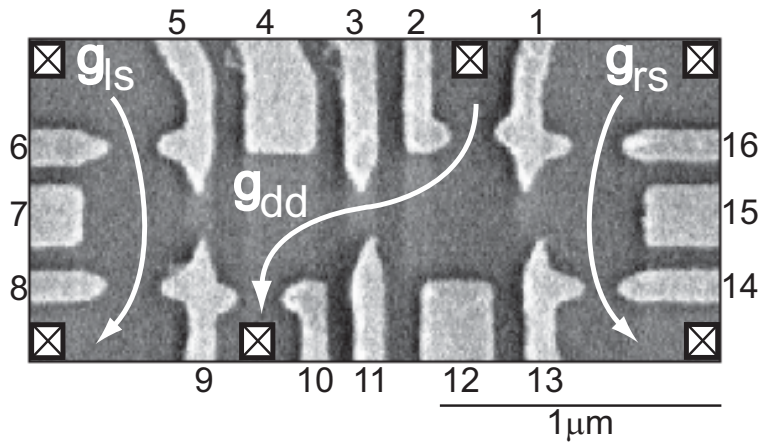


Figure 4.1: Scanning electron micrograph of a device similar to the measured device, consisting of a double quantum dot with quantum point contact charge sensors formed by gates 8/9 (13/14) adjacent to the left (right) dot. Series conductance $g_{\rm dd}$ through the double dot was measured simultaneously with conductances $g_{\rm ls}$ and $g_{\rm rs}$ through the left and right sensors.

previously to investigate charge delocalization in a single dot strongly coupled to a lead in the classical regime [25], and as a means of placing bounds on decoherence in an isolated double quantum dot [109]. The back-action of a QPC sensor, leading to phase decoherence, has been investigated experimentally [28] and theoretically [29, 30]. Charge sensing with sufficient spatial resolution to detect charge distributions within a double dot has been demonstrated in a metallic system [33, 34]. However, in metallic systems the interdot tunnel coupling cannot be tuned, making the crossover to charge delocalization difficult to investigate. Recently, high-bandwidth charge sensing using a metallic single-electron transistor [27], allowing individual charging events to be counted, has been demonstrated [112]. Recent measurements of gate-defined few-electron GaAs double dots [113] have demonstrated dual-QPC charge sensing down to $N, M = 0, 1, 2...$, but did not focus on sensing at fixed electron number, or on charge delocalization. The present experiment uses larger dots, containing $\sim 200$ electrons each (though still with temperature less than level spacing, see below).

The device we investigate, a double quantum dot with adjacent charge sensors, is formed by sixteen electrostatic gates on the surface of a GaAs/$Al_{0.3}Ga_{0.7}As$ heterostructure grown

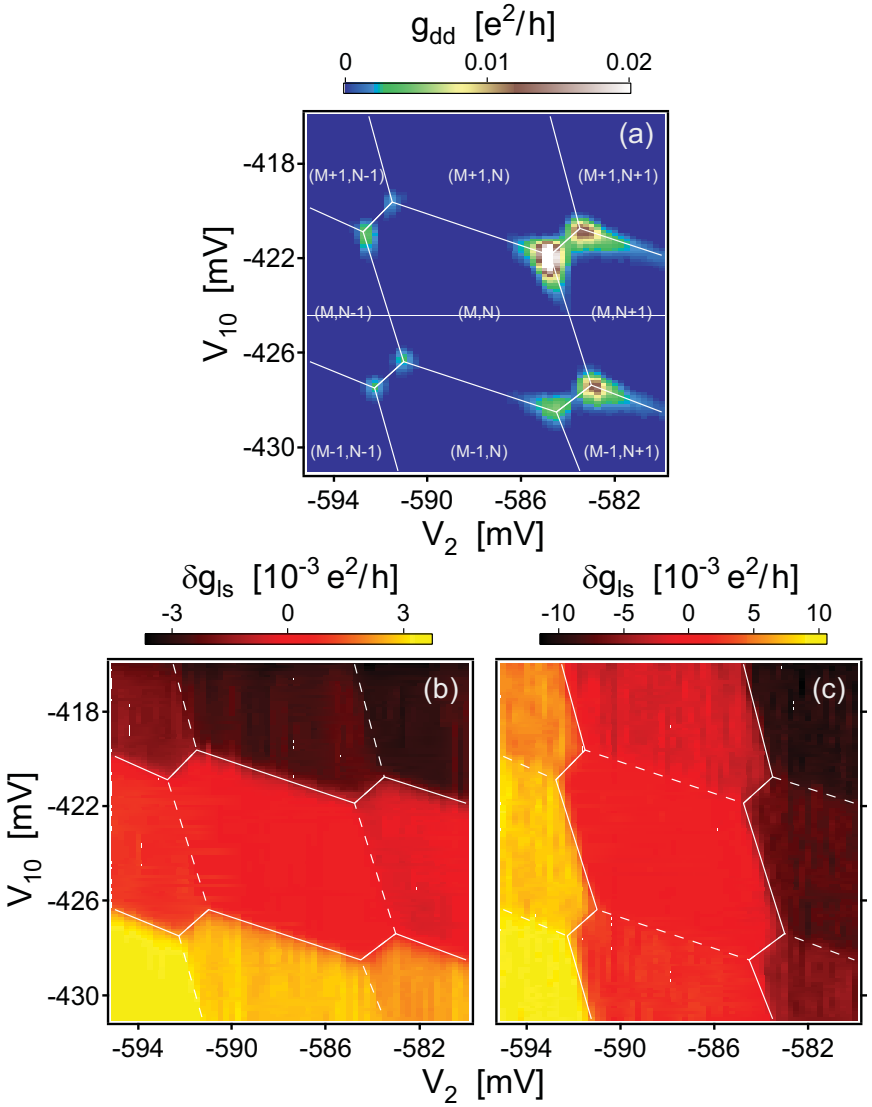


Figure 4.2: (a) Double dot conductance, $g_{\rm dd}$, as a function of gate voltages $V_2$ and $V_{10}$. White lines indicate the honeycomb pattern. Within each honeycomb cell, electron number on each dot is well defined, with $M(N)$ referring to electron number in the left (right) dot. (b, c) Simultaneously measured sensing signals from left (b) and right (c) QPCs. $\delta g_{\rm ls}$ ($\delta g_{\rm rs}$) are QPC conductances after subtracting a best-fit plane. See text for details. The horizontal pattern in (b) and vertical pattern in (c) demonstrate that each sensor is predominantly sensitive to the charge on the dot it borders.

by molecular beam epitaxy (see Fig. 4.1). The two-dimensional electron gas layer, 100 nm below the surface, has an electron density of $2 \times 10^{11}\,\mathrm{cm}^{-2}$ and mobility $2 \times 10^{5}\,\mathrm{cm}^2/\mathrm{Vs}$. Gates 3/11 control the interdot tunnel coupling while gates 1/2 and 9/10 control coupling to electron reservoirs. In this measurement, the left and right sensors were QPCs defined

by gates 8/9 and 13/14, respectively; gates 6, 7, 15, and 16 were not energized. Gaps between gates 5/9 and 1/13 were fully depleted, allowing only capacitive coupling between the double dot and the sensors.

Series conductance, $g_{\mathrm{dd}}$, through the double dot was measured using standard lock-in techniques with a voltage bias of $5\,\mu$V at 87 Hz. Simultaneously, conductances through the left and right QPC sensors, $g_{\mathrm{ls}}$ and $g_{\mathrm{rs}}$, were measured in a current bias configuration using separate lock-in amplifiers with 0.5 nA excitation at 137 and 187 Hz. Throughout the experiment, QPC sensor conductances were set to values in the 0.1 to 0.4 $e^2/h$ range by adjusting the voltage on gates 8 and 14.

The device was cooled in a dilution refrigerator with base temperature $T \sim 30\,\mathrm{mK}$. Electron temperature $T_e$ at base was $\sim 100\,\mathrm{mK}$, measured using Coulomb blockade peak widths with a single dot formed. Single-particle level spacing $\Delta \sim 80\,\mu\mathrm{eV}$ for the individual dots was also measured in a single-dot configuration using differential conductance measurements at finite drain-source bias. Single-dot charging energies, $E_C \sim 500\,\mu\mathrm{eV}$ for both dots, were extracted from the height in bias of Coulomb blockade diamonds [3].

## 4.2 Charge sensing honeycombs

Figure 4.2(a) shows $g_{\mathrm{dd}}$ as a function of gate voltages $V_2$ and $V_{10}$, exhibiting the familiar 'honeycomb' pattern of series conductance through tunnel-coupled quantum dots [12, 114, 115]. Conductance peaks at the honeycomb vertices, the so-called triple points, result from simultaneous alignment of energy levels in the two dots with the chemical potential of the leads. Although conductance can be finite along the honeycomb edges as a result of cotunneling, here it is suppressed by keeping the dots weakly coupled to the leads. Inside a honeycomb, electron number in each dot is well defined as a result of Coulomb blockade. Increasing $V_{10}$ ($V_2$) at fixed $V_2$ ($V_{10}$) raises the electron number in the left (right) dot one by one.

Figures 4.2(b) and 4.2(c) show left and right QPC sensor signals measured simultaneously with $g_{\rm dd}$. The sensor data plotted are $\delta g_{\rm ls(rs)}$, the left (right) QPC conductances after subtracting a best-fit plane (fit to the central hexagon) to remove the background slope due to cross-coupling of the plunger gates (gates 2 and 10) to the QPCs. The left sensor shows conductance steps of size $\sim 3 \times 10^{-3}\, e^2/h$ along the (more horizontal) honeycomb edges where the electron number on the left dot changes by one [solid lines in Fig. 4.2(b)]; the right sensor shows conductance steps of size $\sim 1 \times 10^{-2}\, e^2/h$ along the (more vertical) honeycomb edges where the electron number of the right dot changes by one [solid lines in Fig. 4.2(c)]. Both detectors show a conductance step, one upward and the other downward, along the $\sim 45^\circ$ diagonal segments connecting nearest triple points. It is along this shorter segment that the total electron number is fixed; crossing the line marks the transition from $(M+1, N)$ to $(M, N+1)$. Overall, we see that the transfer of one electron between one dot and the leads is detected principally by the sensor nearest to that dot, while the transfer of one electron between the dots is detected by both sensors, as an upward step in one and a downward step in the other, as expected.

## 4.3 Temperature and tunnel coupling

Focusing on interdot transitions at fixed total charge, i.e., transitions from $(M+1, N)$ to $(M, N+1)$, we present charge-sensing data taken along the "detuning" diagonal by controlling gates $V_2$ and $V_{10}$, shown as a red diagonal line between the triple points in Fig. 4.3(a). Raw data (no background subtracted) for the two sensors are shown in Fig. 4.3(b). The transfer of the excess charge from left dot to right dot causes conductance steps on both QPCs, clearly discernable from background slopes caused by coupling of gates 2 and 10 to the QPCs.

Also shown in Fig. 4.3(b) are fits to the raw sensor data based on a model of local sensing of an isolated two-level system in thermal equilibrium, which we now describe. Varying $V_2$

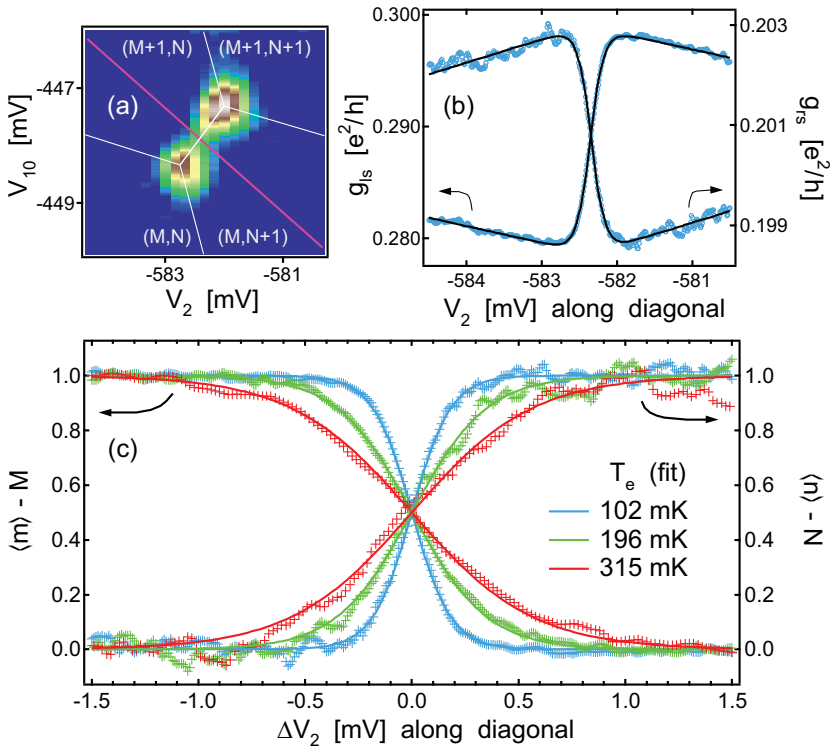


Figure 4.3: (a) Double dot conductance $g_{\rm dd}$ as a function of gate voltages $V_2$ and $V_{10}$ in the vicinity of a triple point. Same color scale as in Fig. 4.1(a). The detuning diagonal (red line) indicates the fixed-charge transition between $(M+1, N)$ and $(M, N+1)$. (b) Left and right QPC conductance with no background subtraction (blue points), along the detuning diagonal, with fits to the two-level model, Eq. (4.2) (black curves). See text for fit details. (c) Excess charge (in units of $e$) in the left and right dot, at $T = 30\,\mathrm{mK}$ (blue), 200 mK (green) and 315 mK (red). Corresponding values of $T_e$ extracted from the fits (solid curves) are 102, 196 and 315 mK.

and $V_{10}$ along the red diagonal changes the electrostatic energy difference, or bare detuning $\epsilon$, between $(M+1, N)$ and $(M, N+1)$ states. The lever arm relating gate voltage to detuning is set by the slope of the diagonal cut [see Fig. 4.3(a)] and various dot capacitances, and can be calibrated experimentally as described below. When the tunnel coupling $t$ mixing these two states is small compared to the single-particle level spacings for the individual dots, we can consider a two-level system whose ground and excited states, separated by an energy $\Omega = \sqrt{\epsilon^2 + 4t^2}$, consist of superpositions of $(M+1, N)$ and $(M, N+1)$ [116]. The probability of finding the excess charge on the left dot while in the ground (excited) state is $\frac{1}{2}(1 \mp \epsilon/\Omega)$. The excited state is populated at finite temperature, with an average

occupation $1/[1+\exp(\Omega/k_BT_e)]$. As shown in App. B, the average excess charge (in units of $e$) on the left and right dots is:

$$\left\{ \begin{array}{c} \langle m \rangle - M \\ \langle n \rangle - N \end{array} \right\} = \frac{1}{2}\left[1 \mp \frac{\epsilon}{\Omega}\tanh\left(\frac{\Omega}{2k_BT_e}\right)\right]. \tag{4.1}$$

Our model assumes that each sensor responds linearly to the average excess charge on each dot, but more sensitively to that on the nearest dot as demonstrated experimentally in Fig. 4.2. The resulting model for sensor conductance is:

$$g_{\mathrm{ls(rs)}} = g_{o\mathrm{l}(o\mathrm{r})} \pm \delta g_{\mathrm{l(r)}}\frac{\epsilon}{\Omega}\tanh\left(\frac{\Omega}{2k_BT_e}\right) + \frac{\partial g_{\mathrm{l(r)}}}{\partial \epsilon}\epsilon. \tag{4.2}$$

The first term on the right is the background conductance of the QPC, the second term represents the linear response to average excess charge, and the third represents direct coupling of the swept gates to the QPC. As shown in Fig. 4.3(b), our model gives very good fits to the data. For each trace (left and right sensors), fit parameters are $g_{o\mathrm{l}(o\mathrm{r})}$, $\delta g_{\mathrm{l(r)}}$, $\frac{\partial g_{\mathrm{l(r)}}}{\partial \epsilon}$, and $T_e$. In these data, the tunnel coupling is weak, and we may set $t = 0$.

Figure 4.3(c) shows the effect of increasing electron temperature on the transition width. Here, vertical axes show excess charge extracted from fits to QPC sensor conductance data. Sweeps along the red diagonal were taken at refrigerator temperatures of 30 mK (blue), 200 mK (green) and 315 mK (red). We use the 315 mK (red) data to extract the lever arm relating voltage along the red diagonal [see Fig. 4.3(a)] to detuning $\epsilon$. At this temperature, electrons are well thermalized to the refrigerator, and thus $T_e \approx T$. The width of the sensing transition at this highest temperature lets us extract the lever arm, which we then use to estimate the electron temperature for the blue (green) data, getting $T_e = 102(196)$ mK.

We next investigate the dependence of the sensing transition on interdot tunneling in the regime of strong tunneling, $t \gtrsim k_BT_e$. Figure 4.4 shows the left QPC sensing signal, again in units of excess charge, along the detuning diagonal crossing a different pair of triple points, at base temperature and for various voltages on the coupling gate 11. For the weakest interdot tunneling shown ($V_{11} = -1096$ mV), the transition was thermally

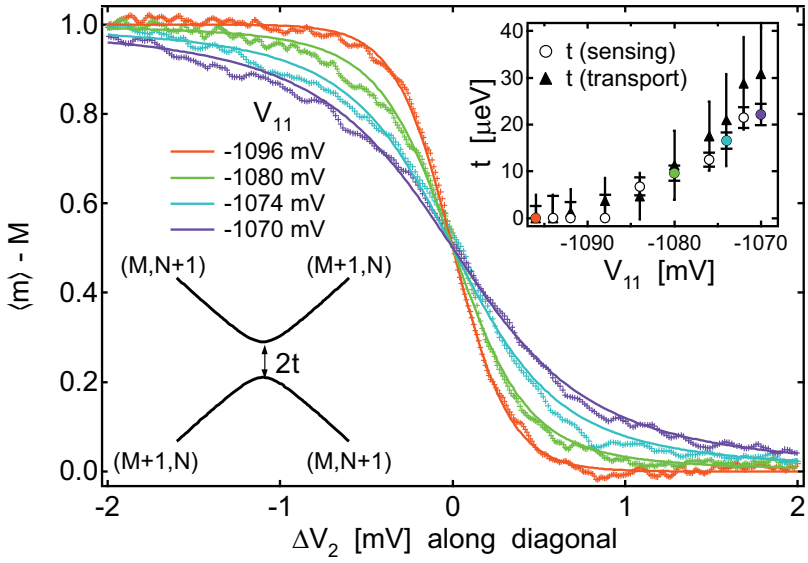


Figure 4.4: Excess charge on the left dot, extracted from left QPC conductance data, along a detuning diagonal (crossing different triple points from those in Fig. 4.4) at base temperature and several settings of the coupling gate 11. The temperature-broadened curve (red) widens as $V_{11}$ is made less negative, increasing the tunnel coupling $t$. See text for details of fits (solid curves). Top right inset: comparison of $t$ values extracted from sensing (circles) and transport (triangles) measurements, as a function of $V_{11}$. Colored circles correspond to the transitions shown in the main graph. Lower left inset: Schematic energy diagram of the two-level system model, showing ground and excited states as a function of detuning $\epsilon$, with splitting (anticrossing) of $2t$ at $\epsilon = 0$.

broadened, i.e., consistent with $t = 0$ in Eqs. (4.1) and (4.2), and did not become narrower when $V_{11}$ was made more negative. On the other hand, when $V_{11}$ was made less negative, the transition widened as the tunneling between dots increased. Taking $T_e = 102\,\mathrm{mK}$ for all data in Fig. 4.4 and calibrating voltage along the detuning diagonal by setting $t = 0$ for the $V_{11} = -1096$ mV trace allows tunnel couplings $t$ to be extracted from fits to our model of the other tunnel-broadened traces. We find $t = 10\,\mu\mathrm{eV}$ (2.4 GHz) (green trace), $t = 16\,\mu\mathrm{eV}$ (3.9 GHz) (turquoise trace), and $t = 22\,\mu\mathrm{eV}$ (5.3 GHz) (purple trace). Again, fits to the two-level model are quite good, as seen in Fig. 4.4.

Finally, we compare tunnel coupling values extracted from charge sensing to values found using a transport-based method that takes advantage of the $t$ dependence of the splitting of triple points (honeycomb vertices) [117, 111]. In the weak tunneling regime, $t \ll \Delta$, the splitting of triple points along the line separating isocharge regions $(M+1, N)$

and $(M, N+1)$ has two components in the plane of gate voltages, denoted here $\delta V_{10}$ and $\delta V_2$. The lower and upper triple points are found where the lowest energy $M+N+1$ state (the delocalized antisymmetric state) becomes degenerate with the charge states $(M, N)$ and $(M+1, N+1)$, respectively. Using the electrostatic model in Ref. [111], we can show (see App. B) that $\delta V_{10(2)}$ are related to various dot capacitances and $t$ by

$$\delta V_{10(2)} = \frac{|e|}{C_{g10(g2)}} \left( \frac{C_m}{C_o + C_m} + 2t \frac{C_o - C_m}{e^2} \right). \tag{4.3}$$

Here, $C_{g10(g2)}$ is the capacitance from gate 10 (2) to the left (right) dot, $C_o$ is the self-capacitance of each dot, and $C_m$ is the interdot mutual capacitance. All these capacitances must be known to allow extraction of $t$ from $\delta V_{10(2)}$. Gate capacitances $C_{g10(g2)}$ are estimated from honeycomb periods along respective gate voltage axes, $\Delta V_{10(2)} \sim |e|/C_{g10(g2)} \sim 6.8\,\mathrm{mV}$. Self-capacitances $C_o$ can be obtained from double dot transport measurements at finite bias [111]. However, lacking that data, we estimate $C_o$ from single-dot measurements of Coulomb diamonds [3]. Mutual capacitance $C_m$ is extracted from the dimensionless splitting $\delta V_{10(2)}/\Delta V_{10(2)} \sim \frac{C_m}{C_o + C_m} \sim 0.2$, measured at the lowest tunnel coupling setting.

Tunnel coupling values as a function of voltage on gate 11, extracted both from charge sensing and triple-point separation, are compared in the inset of Fig. 4.4. The two approaches are in good agreement, with the charge-sensing approach giving significantly smaller uncertainty for $t \gtrsim 0.5 k_B T_e$. The two main sources of error in the sensing approach are uncertainty in the fits (dominant at low $t$) and uncertainty in the lever arm due to a conservative 10 percent uncertainty in $T_e$ at base. Error bars in the transport method are set by the smearing and deformation of triple points as a result of finite interdot coupling and cotunneling. We note that besides being more sensitive, the charge-sensing method for measuring $t$ works when the double dot is fully decoupled from its leads. Like the transport method, however, the sensing approach assumes $t \ll \Delta$ (which may not be amply satisfied for the highest values of $V_{11}$).

## 4.4 Conclusion and acknowledgements

We have demonstrated differential charge sensing in a double quantum dot using paired quantum point contact charge sensors. States $(M+1, N)$ and $(M, N+1)$, with fixed total charge, are readily resolved by the sensors, and serve as a two-level system with a splitting of left/right states controlled by gate-defined tunneling. A model of local charge sensing of a thermally occupied two-level system agrees well with the data. Finally, the width of the $(M+1, N) \rightarrow (M, N+1)$ transition measured with this sensing technique can be used to extract the tunnel coupling with high accuracy in the range $0.5k_BT_e \lesssim t < \Delta$.

We thank M. Lukin, B. Halperin and W. van der Wiel for discussions, and N. Craig for experimental assistance. We acknowledge support by the ARO under DAAD55-98-1-0270 and DAAD19-02-1-0070, DARPA under the QuIST program, the NSF under DMR-0072777 and the Harvard NSEC, Lucent Technologies (HJL), and the Hertz Foundation (LIC).

# Chapter 5

# System for measuring auto- and cross correlation of current noise at low temperatures

L. DiCarlo[1], Yiming Zhang[1], D. T. McClure[1], C. M. Marcus
*Department of Physics, Harvard University, Cambridge, Massachusetts 02138*
L. N. Pfeiffer, K. W. West
*Alcatel-Lucent, Murray Hill, New Jersey 07974*

We describe the construction and operation of a two-channel noise detection system for measuring power and cross spectral densities of current fluctuations near 2 MHz in electronic devices at low temperatures. The system employs cryogenic amplification and fast Fourier transform based spectral measurement. The gain and electron temperature are calibrated using Johnson noise thermometry. Full shot noise of 100 pA can be resolved with an integration time of 10 s.[2]

---

[1]These authors contributed equally to this work.

[2]This chapter is adapted with permission from Rev. Sci. Instrum. **77**, 073906 (2006). © (2006) by the American Institute of Physics.

## 5.1 Introduction

Over the last decade, measurement of electronic noise in mesoscopic conductors has successfully probed quantum statistics, chaotic scattering and many-body effects [39, 46, 118]. Suppression of shot noise below the Poissonian limit has been observed in a wide range of devices, including quantum point contacts [58, 59, 119], diffusive wires [43, 44], and quantum dots [45], with good agreement between experiment and theory. Shot noise has been used to measure quasiparticle charge in strongly correlated systems, including the fractional quantum Hall regime [47, 48, 49] and normal-superconductor interfaces [50], and to investigate regimes where Coulomb interactions are strong, including coupled localized states in mesoscopic tunnel junctions [68] and quantum dots in the sequential tunneling [120, 121] and cotunneling [122] regimes. Two-particle interference not evident in dc transport has been investigated using noise in an electronic beam splitter [119].

Recent theoretical work [123, 51, 124, 125] proposes the detection of electron entanglement via violations of Bell-type inequalities using cross-correlations of current noise between different leads. Most noise measurements have investigated either noise autocorrelation [58, 43, 47, 126, 119, 42, 122] or cross correlation of noise in a common current [59, 127, 44, 128, 45, 68], with only a few experiments [129, 130, 131, 132] investigating cross correlation between two distinct currents. Henny *et al.* [129, 130] and Oberholzer *et al.* [131] measured noise cross correlation in the acoustic frequency range (low kilohertz) using room temperature amplification and a commercial fast Fourier transform (FFT)-based spectrum analyzer. Oliver *et al.* [132] measured cross correlation in the low megahertz using cryogenic amplifiers and analog power detection with hybrid mixers and envelope detectors.

In this chapter, we describe a two-channel noise detection system for simultaneously measuring power spectral densities and cross spectral density of current fluctuations in electronic devices at low temperatures. Our approach combines elements of the two methods described above: cryogenic amplification at low megahertz frequencies and FFT-based

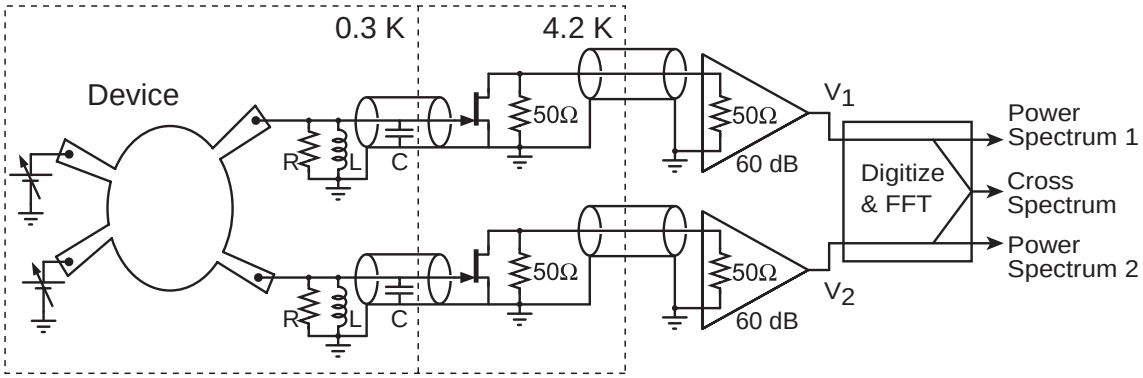


Figure 5.1: Block diagram of the two-channel noise detection system, configured to measure the power spectral densities and cross spectral density of current fluctuations in a multi-terminal electronic device.

spectral measurement.

Several factors make low-megahertz frequencies a practical range for low-temperature current noise measurement. This frequency range is high compared to the $1/f$ noise corner in typical mesoscopic devices. Yet, it is low enough that FFT-based spectral measurement can be performed efficiently with a personal computer (PC) equipped with a commercial digitizer. Key features of this FFT-based spectral measurement are near real-time operation and sufficient frequency resolution to detect spectral features of interest. Specifically, the fine frequency resolution provides information about the measurement circuit and amplifier noise at megahertz, and enables extraneous interference pickup to be identified and eliminated. These two features constitute a significant advantage over both wideband analog detection of total noise power, which sacrifices resolution for speed, and swept-sine measurement, which sacrifices speed for resolution.

## 5.2 Overview of the system

Figure 5.1 shows a block diagram of the two-channel noise detection system, which is integrated with a commercial $^3$He cryostat (Oxford Intruments Heliox $2^{VL}$). The system takes two input currents and amplifies their fluctuations in several stages. First, a parallel resistor-

inductor-capacitor (RLC) circuit performs current-to-voltage conversion at frequencies close to its resonance at $f_o = (2\pi\sqrt{LC})^{-1} \approx 2$ MHz. Through its transconductance, a high electron mobility transistor (HEMT) operating at 4.2 K converts these voltage fluctuations into current fluctuations in a 50 Ω coaxial line extending from 4.2 K to room temperature. A 50 Ω amplifier with 60 dB of gain completes the amplification chain. The resulting signals $V_1$ and $V_2$ are simultaneously sampled at 10 MS/s by a two-channel digitizer (National Instruments PCI-5122) in a 3.4 GHz PC (Dell Optiplex GX280). The computer takes the FFT of each signal and computes the power spectral density of each channel and the cross spectral density.

## 5.3 Amplifier

### 5.3.1 Design objectives

A number of objectives have guided the design of the amplification lines. These include (1) low amplifier input-referred voltage noise and current noise. (2) simultaneous measurement of both noise at megahertz and transport near dc, (3) low thermal load, (4) small size, allowing two amplification lines within the 52 mm bore cryostat, (5) maximum use of commercial components, and (6) compatibility with high magnetic fields.

### 5.3.2 Overview of the circuit

Each amplification line consists of four circuit boards interconnected by coaxial cable, as shown in the circuit schematic in Fig. 5.2(a). Three of the boards are located inside the $^3$He cryostat. The resonant circuit board [labeled RES in Fig. 5.2(a)] is mounted on the sample holder at the end of the 30 cm long coldfinger that extends from the $^3$He pot to the center of the superconducting solenoid. The heat-sink board (SINK) anchored to the $^3$He pot is a meandering line that thermalizes the inner conductor of the coaxial cable. The CRYOAMP board at the 4.2 K plate contains the only active element operating cryogenically, an Ag-

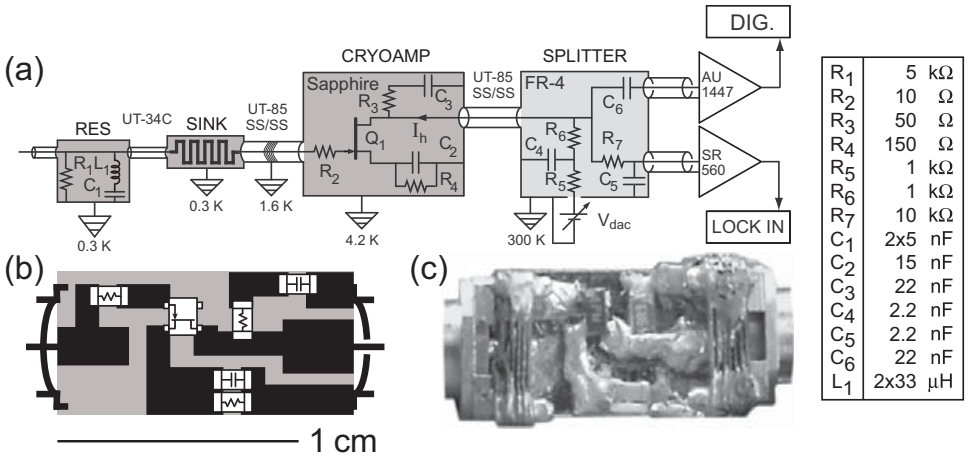


Figure 5.2: (a) Schematic diagram of each amplification line. Values of all passive components are listed in the accompanying table. Transistor $Q_1$ is an Agilent ATF-34143 HEMT. (b) Layout of the CRYOAMP circuit board. Metal (black regions) is patterned by etching of thermally evaporated Cr/Au on sapphire substrate. (c) Photograph of a CRYOAMP board. The scale bar applies to both (b) and (c).

ilent ATF-34143 HEMT. The four-way SPLITTER board operating at room temperature separates low- and high- frequency signals and biases the HEMT. Each line amplifies in two frequency ranges, a low-frequency range below $\sim 3$ kHz and a high-frequency range around 2 MHz.

The low-frequency equivalent circuit is shown in Fig. 5.2(a): a resistor ($R_1 = 5$ kΩ) to ground, shunted by a capacitor ($C_1 = 10$ nF), converts an input current $i$ to a voltage on the HEMT gate. The HEMT amplifies this gate voltage by $\sim -5$ V/V on its drain, which connects to a room temperature voltage amplifier at the low frequency port of the SPLITTER board. The low-frequency voltage amplifier (Stanford Research Systems model SR560) is operated in single-ended mode with ac coupling, 100 V/V gain and bandpass filtering (30 Hz to 10 kHz). The bandwidth in this low-frequency regime is set by the input time constant.

The high-frequency equivalent circuit is shown in Fig. 5.3(b). The inductor $L_1 = 66$ μH dominates over $C_1$ and forms a parallel RLC tank with $R_1$ and the capacitance $C \sim 96$ pF of the coaxial line connecting to the CRYOAMP board. Resistor $R_4$ is shunted by $C_2$ to

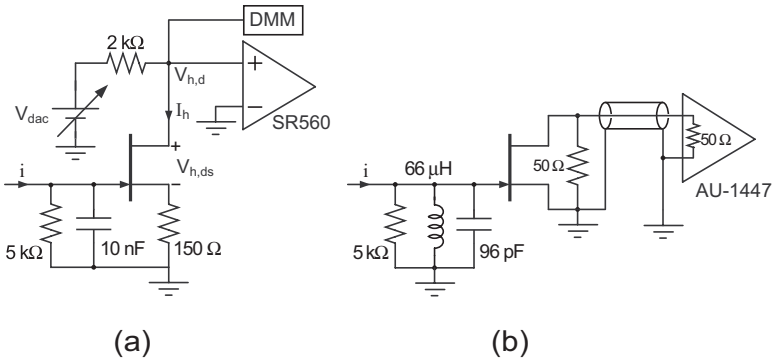


Figure 5.3: Equivalent circuits characterizing the amplification line in the (a) low-frequency regime (up to $\sim 3$ kHz), where it is used for differential conductance measurements, and in the (b) high-frequency regime (few megahertz), where it is used for noise measurement.

enhance the transconductance at the CRYOAMP board. The coaxial line extending from 4.2 K to room temperature is terminated on both sides by 50 Ω. At room temperature, the signal passes through the high-frequency port of the SPLITTER board to a 50 Ω amplifier (MITEQ AU-1447) with a gain of 60 dB and a noise temperature of 100 K in the range $0.01 - 200$ MHz.

### 5.3.3 Operating point

The HEMT must be biased in saturation to provide voltage (transconductance) gain in the low (high) frequency range. $R_4$, $R_5 + R_6$ and supply voltage $V_{\rm dac}$ determine the HEMT operating point ($R_1$ grounds the HEMT gate at dc). A notable difference in this design compared to similar published ones regards the placement of $R_4$. In previous implementations of similar circuits [133, 134, 135], $R_4$ is a variable resistor placed outside the refrigerator and connected to the source lead of $Q_1$ via a second coaxial line or low-frequency wire. Here, $R_4$ is located on the CRYOAMP board to simplify assembly and save space, at the expense of having full control of the bias point in $Q_1$ ($R_4$ fixes the saturation value of the HEMT current $I_{\rm h}$). Using the I-V curves in Ref. [135] for a cryogenically cooled ATF-34143, we choose $R_4 = 150$ Ω to give a saturation current of a few mA. This value of saturation current reflects a compromise between noise performance and power dissipation.

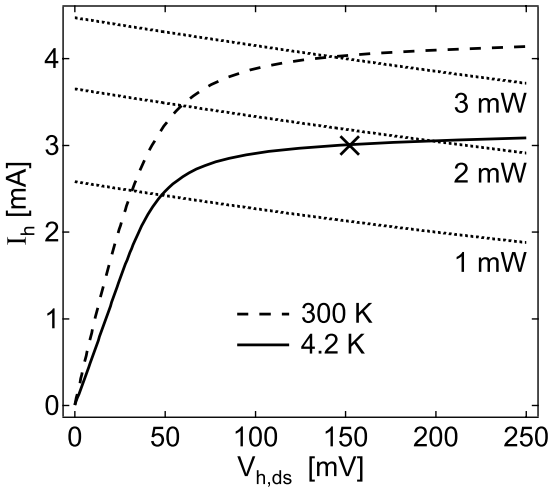


Figure 5.4: Drain current $I_{\rm h}$ as a function of HEMT drain-source voltage $V_{\rm h,ds}$, with the HEMT board at temperatures of 300 K (dashed) and 4.2 K (solid). These curves were obtained by sweeping the supply voltage $V_{\rm dac}$ and measuring drain voltage $V_{\rm h,d}$ with an HP34401A digital multimeter (see Fig. 5.3(a)). From $V_{\rm h,d}$ and $V_{\rm dac}$, $I_{\rm h}$ and $V_{\rm h,ds}$ were then extracted. Dotted curves are contours of constant power dissipation in the HEMT board. The HEMT is biased in saturation (cross).

As shown in Fig. 5.4, $Q_1$ is biased by varying the supply voltage $V_{\rm dac}$ fed at the SPLITTER board. At the bias point indicated by a cross, the total power dissipation in the HEMT board is $I_{\rm h}V_{\rm h,ds} + I_{\rm h}^2 R_4 = 1.8$ mW, and the input-referred voltage noise of the HEMT is $\sim 0.4$ nV/$\sqrt{\rm Hz}$.

### 5.3.4 Passive components

Passive components were selected based on temperature stability, size and magnetic field compatibility. All resistors (Vishay TNPW thin film) are 0805-size surface mount. Their variation in resistance between room temperature and 300 mK is $< 0.5\%$. Inductor $L_1$ (two 33 $\mu$H Coilcraft 1812CS ceramic chip inductors in series) does not have a magnetic core and is suited for operation at high magnetic fields. The dc resistance of $L_1$ is 26(0.3) $\Omega$ at 300(4.2) K. With the exception of $C_1$, all capacitors are 0805-size surface mount (Murata COG GRM21). $C_1$ (two 5 nF American Technical Ceramics 700B NPO capacitors in parallel) is certified nonmagnetic.

### 5.3.5 Thermalization

To achieve a low device electron temperature, circuit board substrates must handle the heat load from the coaxial line. The CRYOAMP board must also handle the power dissipated by the HEMT and $R_4$. Sapphire, having good thermal conductivity at low temperatures [40] and excellent electrical insulation, is used for the substrate in the RES, SINK and CRYOAMP boards. Polished blanks, 0.02 in. thick and 0.25 in. wide, were cut to lengths of 0.6 in. (RES and CRYOAMP) or 0.8 in. (SINK) using a diamond saw. Both planar surfaces were metallized with thermally evaporated Cr/Au (30/300 nm). Circuit traces were then defined on one surface using a Pulsar toner transfer mask and wet etching with Au and Cr etchants (Transene types TFA and 1020). Surface mount components were directly soldered.

The RES board is thermally anchored to the sample holder with silver epoxy (Epoxy Technology 410E). The CRYOAMP (SINK) board is thermalized to the 4.2 K plate ($^3$He pot) by a copper braid soldered to the back plane.

Semirigid stainless steel coaxial cable (Uniform Tube UT85-SS/SS) is used between the SINK and CRYOAMP boards, and between the CRYOAMP board and room temperature. Between the RES and SINK boards, smaller coaxial cable (Uniform Tube UT34-C) is used to conserve space.

With this approach to thermalization, the base temperature of the $^3$He refrigerator is 290 mK with a hold time of $\sim$ 45 h. As demonstrated further below, the electron base temperature in the device is also 290 mK.

## 5.4 Digitization and FFT processing

The amplifier outputs $V_1$ and $V_2$ (see Fig. 5.1) are sampled simultaneously using a commercial digitizer (National Instruments PCI-5122) with 14-bit resolution at a rate $f_s = 10$ MS/s. To avoid aliasing [136] from the broadband amplifier background, $V_1$ and $V_2$ are frequency

limited to below the Nyquist frequency of 5 MHz using 5-pole Chebyshev low-pass filters, built in-house from axial inductors and capacitors with values specified by the design recipe in Ref. [137]. The filters have a measured half power frequency of 3.8 MHz, 39 dB suppression at 8 MHz and a passband ripple of 0.03 dB.

While the digitizer continuously stores acquired data into its memory buffer (32 MB per channel), a software program processes the data from the buffer in blocks of $M = 10\ 368$ points per channel. $M$ is chosen to yield a resolution bandwidth $f_s/M \sim 1$ kHz, and to be factorizable into powers of two and three to maximize the efficiency of the FFT algorithm.

Each block of data is processed as follows. First, $V_1$ and $V_2$ are multiplied by a Hanning window $W_H[m] = \sqrt{2/3}[1 - \cos(2\pi m/M)]$ to avoid end effects [136]. Second, using the FFTW package [138], their FFTs are calculated:

$$\widetilde{V}_{1(2)}[f_n] = \sum_{m=0}^{M-1} W_{\mathrm{H}}[m] V_{1(2)}(t_m) e^{-i2\pi f_n t_m}, \tag{5.1}$$

where $t_m = m/f_s$, $f_n = (n/M)f_s$, and $n = 0, 1, ..., M/2$. Third, the power spectral densities $P_{1,2} = 2|\widetilde{V}_{1,2}|^2/(Mf_s)$ and the cross spectral density $X = 2(\widetilde{V}_1^* \cdot \widetilde{V}_2)/(Mf_s) = X_R + iX_I$ are computed.

As blocks are processed, running averages of $P_1$, $P_2$, and $X$ are computed until the desired integration time $\tau_{\mathrm{int}}$ is reached. With the 3.4 GHz computer and the FFTW algorithm, these computations are carried out in nearly real-time: it takes 10.8 s to acquire and process 10 s of data.

## 5.5 Measurement example: quantum point contact

In this section, we demonstrate the two-channel noise detection system with measurements of a quantum point contact (QPC). While the investigation of bias-dependent current noise in QPCs is the main topic of Ch. 6, we here describe the techniques used for measuring dc transport, as well as the circuit model and the calibration (based on Johnson-noise thermometry) that are used for extracting QPC noise.

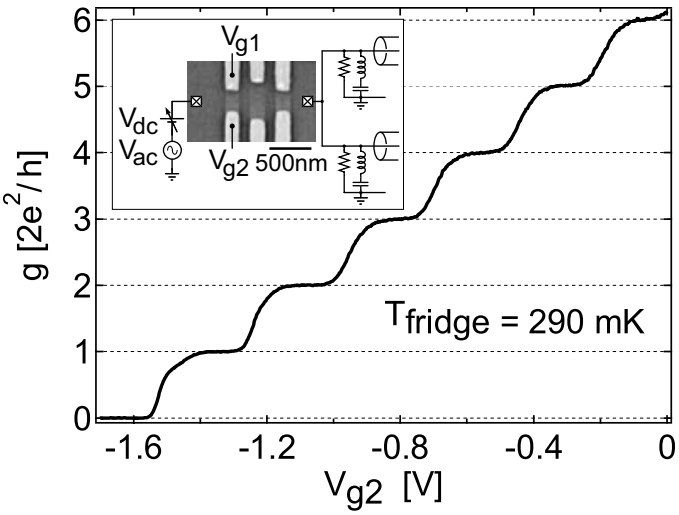


Figure 5.5: Inset: setup for detection of QPC current noise using cross-correlation, and electron micrograph of a device identical in design to the one used. The QPC is defined by negative voltages $V_{g1}$ and $V_{g2}$ applied on two facing gates. All other gates in the device are grounded. Main: linear conductance $g(V_{sd} = 0)$ as a function of $V_{g2}$ at 290 mK, measured using amplification line 1. $V_{g1} = -3.2$ V.

### 5.5.1 Setup

A gate-defined QPC[3] is connected to the system as shown in the inset of Fig. 5.5. The two amplification lines are connected to the same reservoir of the QPC. In this case, the two input RLC tanks effectively become a single tank with resistance $R' \approx 2.5$ kΩ, inductance $L' \approx 33$ $\mu$H and capacitance $C' \approx 192$ pF. The QPC current noise couples to both amplification lines and thus can be extracted from either the single channel power spectral densities or the cross spectral density. The latter has the technical advantage of rejecting any noise not common to both amplification lines.

### 5.5.2 Measuring dc transport

A 25 $\mu V_{rms}$, 430 Hz excitation $V_{ac}$ is applied to the other QPC reservoir and used for lock-in measurement of $g$. A dc bias voltage $V_{dc}$ is also applied to generate a finite $V_{sd}$. $V_{sd}$ deviates from $V_{dc}$ due to the resistance in-line with the QPC, which is equal to the sum of $R_1/2$ and

[3]This device is named QPC 1 in Ch. 6.

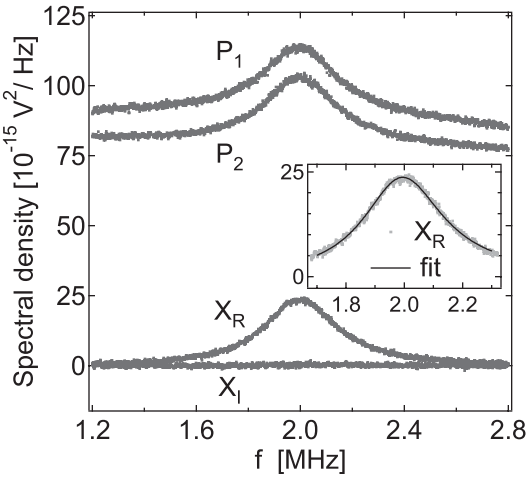


Figure 5.6: Power spectral densities $P_1$ and $P_2$, and real and imaginary parts $X_R$ and $X_I$ of the cross spectral density, at base temperature and with the QPC pinched off ($g = 0$), obtained from noise data acquired for $\tau_{\rm int} = 20$ s. Inset: expanded view of $X_R$ near resonance, along with a fit using Eq. (5.3) over the range 1.7 to 2.3 MHz.

ohmic contact resistance $R_s$. $V_{\rm sd}$ could in principle be measured by the traditional four-wire technique. This would require additional low-frequency wiring, as well as filtering to prevent extraneous pick-up and room-temperature amplifier noise from coupling to the noise measurement circuit. For technical simplicity, here $V_{\rm sd}$ is obtained by numerical integration of the measured bias-dependent $g$:

$$V_{\rm sd} = \int_0^{V_{\rm dc}} \frac{dV}{1 + (R_1/2 + R_s)g(V)} \tag{5.2}$$

Figure 5.5 shows linear conductance $g(V_{\rm sd} = 0)$ as a function of gate voltage $V_{\rm g2}$, at a fridge temperature $T_{\rm fridge} = 290$ mK (base temperature). Here, $g$ was extracted from lock-in measurements using amplification line 1. As neither the low frequency gain of amplifier 1 nor $R_s$ were known precisely beforehand, these parameters were calibrated by aligning the observed conductance plateaus to the expected multiples of $2e^2/h$. This method yielded a low-frequency gain $-4.6$ V/V and $R_s = 430\ \Omega$.

### 5.5.3 Measuring noise

Figure 5.6 shows $P_1$, $P_2$, $X_R$, and $X_I$ as a function of frequency $f$, at base temperature and with the QPC pinched off ($g = 0$). $P_{1(2)}$ shows a peak at the resonant frequency of the RLC tank, on top of a background of approximately $85(78) \times 10^{-15}$ V$^2$/Hz. The background in $P_{1(2)}$ is due to the voltage noise $S_{V,1(2)}$ of amplification line 1(2) ($\sim 0.4$ nV/$\sqrt{\text{Hz}}$). The peak results from thermal noise of the resonator resistance and current noise ($S_{I,1} + S_{I,2}$) from the amplifiers[4]. $X_R$ picks out this peak and rejects the amplifier voltage noise backgrounds. The inset zooms in on $X_R$ near the resonant frequency. The solid curve is a best-fit to the form

$$X_R(f) = \frac{X_R^0}{1 + (f^2 - f_o^2)^2/(f\Delta f_{3\text{dB}})^2}, \tag{5.3}$$

corresponding to the lineshape of white noise band-pass filtered by the RLC tank. The fit parameters are the peak height $X_R^0$, the half-power bandwidth $\Delta f_{3\text{dB}}$ and the peak frequency $f_o$. Power spectral densities $P_{1(2)}$ can be fit to a similar form including a fitted background term:

$$P_{1(2)}(f) = P_{1(2)}^{\text{B}} + \frac{P_{1(2)}^0}{1 + (f^2 - f_o^2)^2/(f\Delta f_{3\text{dB}})^2}. \tag{5.4}$$

### 5.5.4 System calibration using Johnson noise

Chapter 6 presents measurements of QPC excess noise, defined as $S_I^{\text{P}}(V_{\text{sd}}) = S_I(V_{\text{sd}}) - 4k_BT_eg(V_{\text{sd}})$ ($S_I$ is the total QPC current noise spectral density). The extraction of $S_I^{\text{P}}$ from measurements of $X_R^0$ requires that a circuit model for the noise detection system be defined and that all its parameters be calibrated *in situ*. The circuit model we use is shown in Fig. 5.7. Within this model,

$$S_I^{\text{P}} = \left(\frac{X_R^0}{G_X^2} - 4k_BT_eR_{\text{eff}}\right)\left(\frac{1 + gR_s}{R_{\text{eff}}}\right)^2, \tag{5.5}$$

[4]Further below, the contribution from amplifier current noise is shown to be negligible.

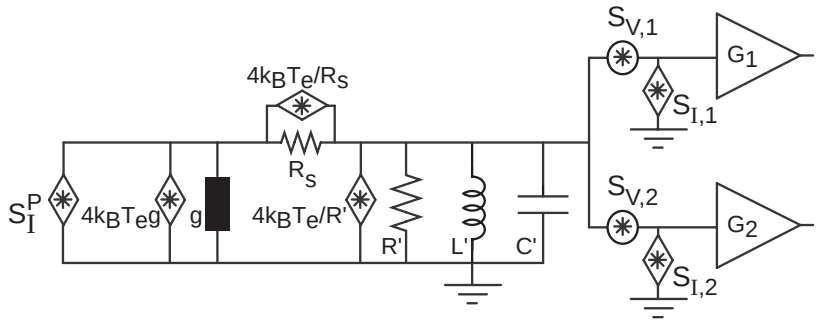


Figure 5.7: Circuit model used for extraction of the QPC partition noise $S_I^{\mathrm{P}}$. $G_{1(2)}$ is the voltage gain of amplification line 1(2) between HEMT gate and digitizer input.

where $G_X = \sqrt{G_1 G_2}$ is the cross-correlation gain and $R_{\mathrm{eff}} = 2\pi f_o^2 L'/\Delta f_{3\mathrm{dB}}$ is the total effective resistance parallel to the tank[5]. Calibration requires assigning values for $R_s$, $T_e$, and $G_X$. While the value $R_s$ is obtained from the conductance measurement, $G_X$ and $T_e$ are calibrated from thermal noise measurements. The procedure demonstrated in Fig. 5.8 stems from the relation[6] $X_R^0 = 4k_B T_e R_{\mathrm{eff}} G_X^2$, valid at $V_{\mathrm{sd}} = 0$.

First, $X_R(f)$ is measured over $\tau_{\mathrm{int}} = 30$ s for various $V_{\mathrm{g2}}$ settings at each of three elevated fridge temperatures ($T_{\mathrm{fridge}} = 3.1,\ 4.2,$ and 5.3 K). $X_R^0$ and $R_{\mathrm{eff}}$ are extracted from fits to $X_R(f)$ using Eq. (3) and plotted parametrically (open markers in Fig. 8(a)). A linear fit (constrained to pass through the origin) to each parametric plot gives the slope $dX_R^0/dR_{\mathrm{eff}}$ at each temperature, equal to $4k_B T_e G_X^2$. Assuming $T_e = T_{\mathrm{fridge}}$ at these temperatures, $G_X = 790$ V/V is extracted from a linear fit to $dX_R^0/dR_{\mathrm{eff}}(T_{\mathrm{fridge}})$, shown in Fig. 5.8(b).

Next, the base electron temperature is calibrated from a parametric plot of $X_R^0$ as a function of $R_{\mathrm{eff}}$ obtained from similar measurements at base temperature [solid circles in Fig. 5.8(a)]. From the fitted slope $dX_R^0/dR_{\mathrm{eff}}$ [black marker in Fig. 5.8(b)] and using the

[5]Within the model, $R_{\mathrm{eff}} = (1/(1/g + R_s) + 1/R')^{-1}$. The best-fit $\Delta f_{3\mathrm{dB}}$ to the measurement shown in Fig. 5.6 with the QPC pinched off ($g = 0$) gives $R' = 2.4$ kΩ. This small reduction from 2.5 KΩ reflects small inductor and capacitor losses near the resonant frequency.

[6]The full expression within the circuit model is $X_R^0 = (4k_B T_e R_{\mathrm{eff}} + (S_{I,1} + S_{I,2})R_{\mathrm{eff}}^2)G_X^2$. The linear dependence of $X_R^0$ on $R_{\mathrm{eff}}$ observed in Fig. 5.8(a) demonstrates that the quadratic term from amplifier current noise is negligible.

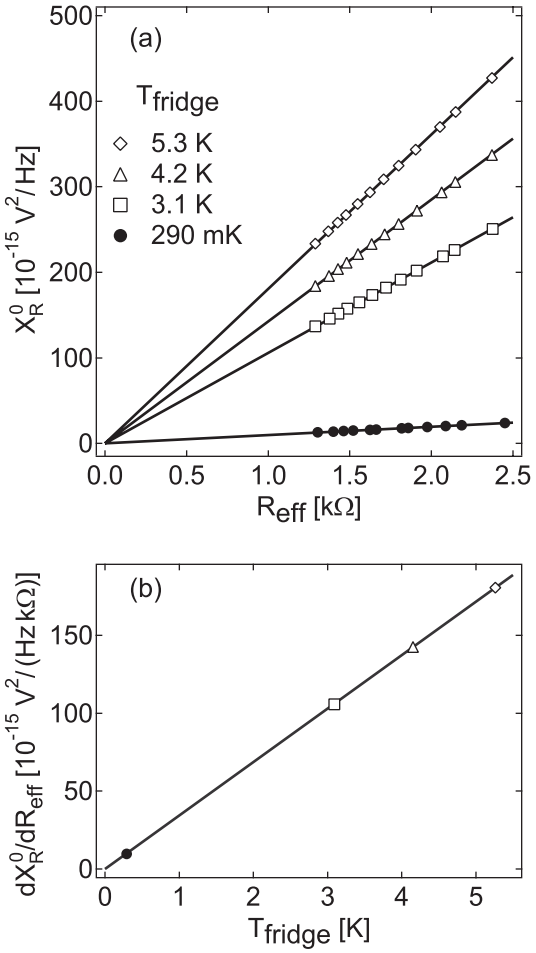


Figure 5.8: Calibration by noise thermometry of the electron temperature $T_e$ at base fridge temperature and the cross-correlation gain $G_X$. (a) $X_R^0$ as function of $R_{\rm eff}$ (both from fits to $X_R(f)$ using Eq. (5.3)), at base (solid circles) and at three elevated fridge temperatures (open markers). Solid lines are linear fits constrained to the origin. (b) Slope $dX_R^0/dR_{\rm eff}$ (from fits in (a)) as a function of $T_{\rm fridge}$. Solid line is a linear fit (constrained to the origin) of $dX_R^0/dR_{\rm eff}$ at the three elevated temperatures (open markers).

calibrated $G_X$, a value $T_e = 290$ mK is obtained. This suggests that electrons are well thermalized to the fridge.

## 5.6 System performance

The resolution in the estimation of current noise spectral density from one-channel and two-channel measurements is determined experimentally in this section. Noise data are

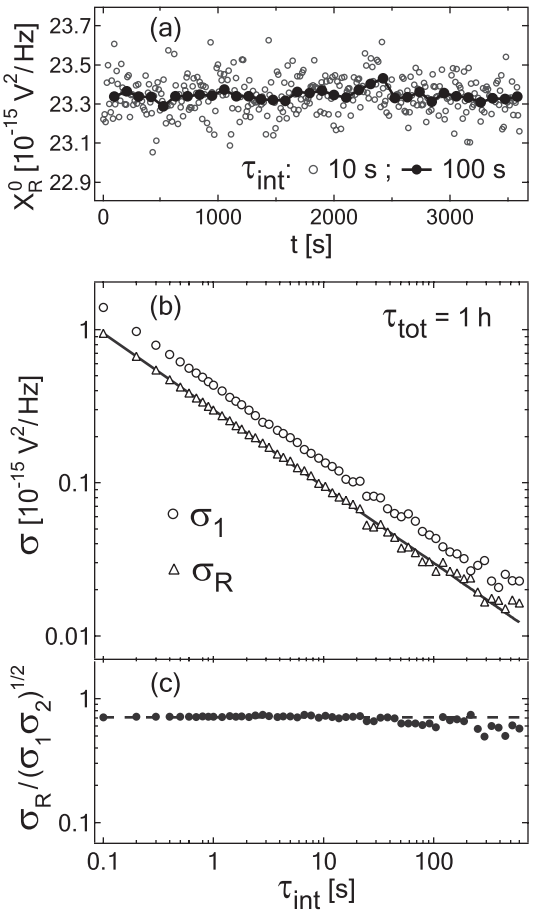


Figure 5.9: (a) $X_R^0$ as a function of time $t$, for $\tau_{\rm int}$ of 10 s (open circles) and 100 s (solid circles). (b) Standard deviations $\sigma_1$ and $\sigma_R$ as a function of $\tau_{\rm int}$. The solid line is a fit to $\sigma_R$ of the form $C\tau_{\rm int}^{-1/2}$, with best-fit value $C = 0.30 \times 10^{-15}$ $\rm s^{1/2}V^2/Hz$. (c) $\sigma_R/\sqrt{\sigma_1\sigma_2}$ as a function of $\tau_{\rm int}$. The dashed line is a constant $1/\sqrt{2}$.

first sampled over a total time $\tau_{\rm tot} = 1$ h, with the QPC at base temperature and pinched off. Dividing the data in segments of time length $\tau_{\rm int}$, calculating the power and cross spectral densities for each segment, and fitting with Eqs. (5.3) and (5.4) gives a sequence of $\tau_{\rm tot}/\tau_{\rm int}$ peak heights for each of $P_1$, $P_2$ and $X_R$. Shown in open (solid) circles in Fig. 5.9(a) is $X_R^0$ as a function of time $t$ for $\tau_{\rm int} = 10(100)$ s. The standard deviation $\sigma_R$ of $X_R^0$ is $1(0.3) \times 10^{-16}$ $\rm V^2/Hz$. The resolution $\delta S_I$ in current noise spectral density is given by $\sigma_R/(G_X^2 R_{\rm eff}^2)$ [see Eq. (5.5)]. For $\tau_{\rm int} = 10$ s, $\delta S_I = 2.8 \times 10^{-29}$ $\rm A^2/Hz$, which corresponds to full shot noise $2eI$ of $I \sim 100$ pA.

The effect of integration time on the resolution is determined by repeating the analysis

for different values of $\tau_{\rm int}$. Fig. 5.9(b) shows the standard deviation $\sigma_1$ ($\sigma_R$) of $P_1^0$ ($X_R^0$) as a function of $\tau_{\rm int}$. The standard deviation $\sigma_2$ of $P_2^0$, not shown, overlaps closely with $\sigma_1$. All three standard deviations scale as $1/\sqrt{\tau_{\rm int}}$, consistent with the Dicke radiometer formula [139] which applies when measurement error results only from finite integration time, i.e., it is purely statistical. This suggests that, even for the longest segment length of $\tau_{\rm int} = 10$ min, the measurement error is dominated by statistical error and not by instrumentation drift on the scale of 1 h.

Figure 5.9(c) shows $\sigma_{\rm R}/\sqrt{\sigma_1\sigma_2}$ as a function of $\tau_{\rm int}$. This ratio gives the fraction by which, in the present measurement configuration, the statistical error in current noise spectral density estimation from $X_R^0$ is lower than the error in the estimation from either $P_1^0$ or $P_2^0$ alone. The geometric mean in the denominator accounts for any small mismatch in the gains $G_1$ and $G_2$. In theory, and in the absence of drift, this ratio is independent of $\tau_{\rm int}$ and equal to $1/\sqrt{2}$ when the uncorrelated amplifier voltage noise [$S_{V,1(2)}$] dominates over the noise common to both amplification lines. The ratio would be unity when the correlated noise dominates over $S_{V,1(2)}$.

The experimental $\sigma_{\rm R}/\sqrt{\sigma_1\sigma_2}$ is close to $1/\sqrt{2}$ (dashed line). This is consistent with the spectral density data in Fig. 5.6, which shows that the backgrounds in $P_1$ and $P_2$ are approximately three times larger than the cross-correlation peak height. The ratio deviates slightly below $1/\sqrt{2}$ at the largest $\tau_{\rm int}$ values. This may result from enhanced sensitivity to error in the substraction of the $P_{1(2)}$ background at the longest integration times.

A similar improvement relative to estimation from either $P_1^0$ or $P_2^0$ alone would also result from estimation with a weighted average $(P_1^0/G_1^2 + P_2^0/G_2^2)G_X^2/2$. The higher resolution attainable from two channel measurement relative to single-channel measurement in this regime has been previously exploited in noise measurements in the kilohertz range [59, 127, 128].

## 5.7 Discussion

We have presented a two-channel noise detection system measuring auto- and cross correlation of current fluctuations near 2 MHz in electronic devices at low temperatures. The system has been implemented in a $^3$He refrigerator where the base device electron temperature, measured by noise thermometry, is 290 mK. Similar integration with a $^3$He -$^4$He dilution refrigerator would enable noise measurement at temperatures of tens of millikelvin.

## 5.8 Acknowledgements

We thank N. J. Craig, J. B. Miller, E. Onitskansky, and S. K. Slater for device fabrication. We also thank H.-A. Engel, D. C. Glattli, P. Horowitz, W. D. Oliver, D. J. Reilly, P. Roche, A. Yacoby, Y. Yamamoto for valuable discussion, and B. D'Urso, F. Molea and H. Steinberg for technical assistance. We acknowledge support from NSF-NSEC, ARDA/ARO, and Harvard University.

# Chapter 6

# Current noise in quantum point contacts

L. DiCarlo[1], Yiming Zhang[1], D. T. McClure[1], D. J. Reilly, C. M. Marcus
*Department of Physics, Harvard University, Cambridge, Massachusetts 02138*
L. N. Pfeiffer, K. W. West
*Alcatel-Lucent, Murray Hill, New Jersey 07974*
M. P. Hanson, A. C. Gossard
*Department of Materials, University of California, Santa Barbara, California 93106*

We present measurements of current noise in QPCs as a function of source-drain bias, gate voltage, and in-plane magnetic field. At zero bias, Johnson noise provides a measure of the electron temperature. At finite bias, shot noise at zero field exhibits an asymmetry related to the 0.7 structure in conductance. The asymmetry in noise evolves smoothly into the symmetric signature of spin-resolved electron transmission at high field. Comparison to a phenomenological model with density-dependent level splitting yields quantitative agreement. Additionally, a device-specific contribution to the finite-bias noise, particularly visible on conductance plateaus (where shot noise vanishes), agrees quantitatively with a model of bias-dependent electron heating.[2]

---

[1]These authors contributed equally to this work.

[2]This chapter is adapted from Ref. [55] and from Phys. Rev. Lett. **97**, 036810 (2006) [with permission, © (2006) by the American Physical Society].

## 6.1 Introduction

The experimental discovery nearly two decades ago [7, 8] of quantized conductance in quantum point contacts (QPCs) suggested the realization of an electron waveguide. Pioneering measurements [58, 59, 119] of noise in QPCs almost a decade later observed suppression of shot noise below the Poissonian value due to Fermi statistics, as predicted by mesoscopic scattering theory [140, 141]. Shot noise has since been increasingly recognized as an important probe of quantum statistics and many-body effects [39, 46, 118], complementing dc transport. For example, shot-noise measurements have been exploited to directly observe quasiparticle charge in strongly correlated systems [47, 48, 49, 50], as well as to study interacting localized states in mesoscopic tunnel junctions [68] and cotunneling [122] and dynamical channel blockade [121, 67] in quantum dots.

Paralleling these developments, a large literature has emerged concerning the appearance of an additional plateau-like feature in transport through a QPC at zero magnetic field, termed 0.7 structure. Experiment [56, 142, 143, 144, 145, 146, 147] and theory [148, 149, 150, 151, 152, 57] suggest that 0.7 structure is a many-body spin effect. Its underlying microscopic origin remains an outstanding problem in mesoscopic physics. This persistently unresolved issue is remarkable given the simplicity of the device.

In this chapter, we review our work [54] on current noise in quantum point contacts—including shot-noise signatures of 0.7 structure and effects of in-plane field $B_{\|}$—and present new results on a device-specific contribution to noise that is well described by a model that includes bias-dependent heating in the vicinity of the QPC. Notably, we observe suppression of shot noise relative to that predicted by theory for spin-degenerate transport [140, 141] near $0.7 \times 2e^2/h$ at $B_{\|} = 0$, consistent with previous work [153, 60]. The suppression near $0.7 \times 2e^2/h$ evolves smoothly with increasing $B_{\|}$ into the signature of spin-resolved transmission. We find quantitative agreement between noise data and a phenomenological model for a density-dependent level splitting [57], with model parameters extracted solely

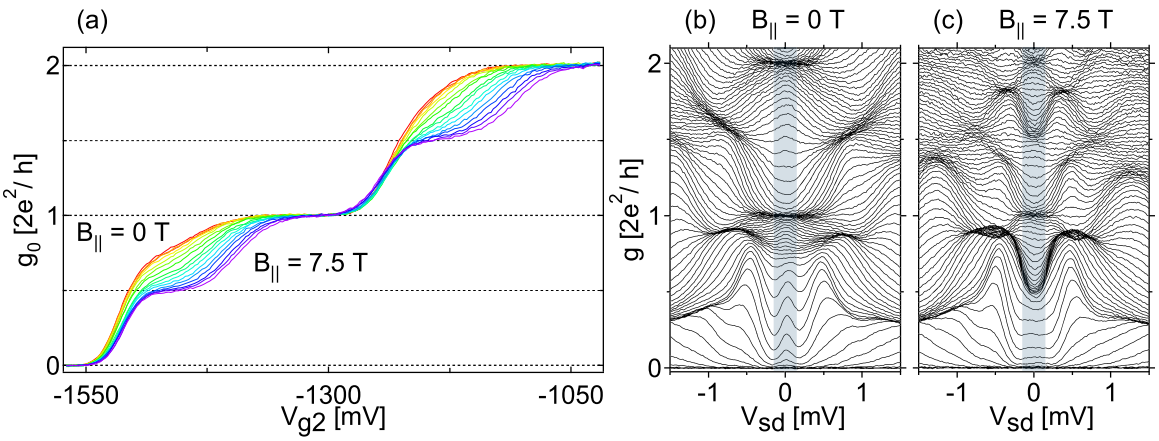


Figure 6.1: (a) Linear conductance $g_0$ as a function of $V_{g2}$ ($V_{g1} = -3.2$ V), for $B_{||}$ ranging from 0 (red) to 7.5 T (purple) in steps of 0.5 T. The series resistance $R_s$ ranging from 430 Ω at $B_{||} = 0$ to 730 Ω at $B_{||} = 7.5$ T has been subtracted to align the plateaus at multiples of $2e^2/h$. (b,c) Nonlinear differential conductance $g$ as a function of $V_{sd}$, at $B_{||} = 0$ (b) and 7.5 T (c), with $V_{g2}$ intervals of 7.5 and 5 mV, respectively. Shaded regions indicate the bias range used for the noise measurements presented in Figs. 6.3(c) and 6.4.

from conductance. In the final section, we investigate a device-specific contribution to the bias-dependent noise, particularly visible on conductance plateaus (where shot noise vanishes), which we account for with a model [59] of Wiedemann-Franz thermal conduction in the reservoirs connecting to the QPC.

## 6.2 QPC characterization

Measurements are presented for two QPCs defined by split gates on GaAs/$Al_{0.3}Ga_{0.7}As$ heterostructures grown by molecular beam epitaxy. For QPC 1(2), the two-dimensional electron gas [2DEG] 190(110) nm below the heterostructure surface has density 1.7(2) × $10^{11}$ $cm^{-2}$ and mobility 5.6(0.2)×$10^6$ $cm^2$/Vs. Except where noted, all data are taken at the base temperature of a $^3$He cryostat, with electron temperature $T_e$ of 290 mK. A magnetic field of 125 mT, applied perpendicular to the plane of the 2DEG, was used to reduce bias-dependent heating [59] (see section below). Each QPC is first characterized at both zero and finite $B_{||}$ using near-dc transport measurements. The differential conductance $g = dI/dV_{sd}$ (where $I$ is the current and $V_{sd}$ is the source-drain bias) is measured by lock-in technique

as discussed in Sec. 5.5.2. The $B_{\|}$-dependent ohmic contact and reservoir resistance $R_s$ in series with the QPC is subtracted.

Figure 6.1 shows conductance data for QPC 1 (see micrograph in Fig. 6.2). Linear-response conductance $g_0 = g(V_{\rm sd} \sim 0)$ as a function of gate voltage $V_{\rm g2}$, for $B_{\|} = 0$ to 7.5 T in steps of 0.5 T, is shown in Fig. 6.1(a). The QPC shows the characteristic quantization of conductance in units of $2e^2/h$ at $B_{\|} = 0$, and the appearance of spin-resolved plateaus at multiples of $0.5 \times 2e^2/h$ at $B_{\|} = 7.5$ T. Additionally, at $B_{\|} = 0$, a shoulder-like 0.7 structure is evident, which evolves continuously into the $0.5 \times 2e^2/h$ spin-resolved plateau at high $B_{\|}$ [56].

Figures 6.1(b) and 6.1(c) show $g$ as a function of $V_{\rm sd}$ for evenly spaced $V_{\rm g2}$ settings at $B_{\|} = 0$ and 7.5 T, respectively. In this representation, linear-response plateaus in Fig. 6.1(a) appear as accumulated traces around $V_{\rm sd} \sim 0$ at multiples of $2e^2/h$ for $B_{\|} = 0$, and at multiples of $0.5 \times 2e^2/h$ for $B_{\|} = 7.5$ T. At finite $V_{\rm sd}$, additional plateaus occur when a sub-band edge lies between the source and drain chemical potentials [154]. The features near $0.8 \times 2e^2/h$ ($V_{\rm sd} \sim \pm 750$ $\mu$V) at $B_{\|} = 0$ cannot be explained within a single-particle picture [155]. These features are related to the 0.7 structure around $V_{\rm sd} \sim 0$ and resemble the spin-resolved finite bias plateaus at $\sim 0.8 \times 2e^2/h$ for $B_{\|} = 7.5$ T [143, 145].

## 6.3 Current noise

QPC current noise is measured using the cross-correlation technique (see Fig. 6.2) discussed in Sec. 5.5.3. Johnson-noise thermometry allows *in situ* calibration of $T_e$ and the amplification gain in the noise detection system by the procedure previously demonstrated in Sec. 5.5.4.

We characterize the QPC noise at finite bias by the excess noise, defined as $S_I^{\rm P}(V_{\rm sd}) = S_I(V_{\rm sd}) - 4k_BT_e g(V_{\rm sd})$, where $S_I$ is the total QPC current noise spectral density. Note that $S_I^{\rm P}$ is the noise in excess of $4k_BT_e g(V_{\rm sd})$ rather than $4k_BT_e g(0)$ and thus differs from excess

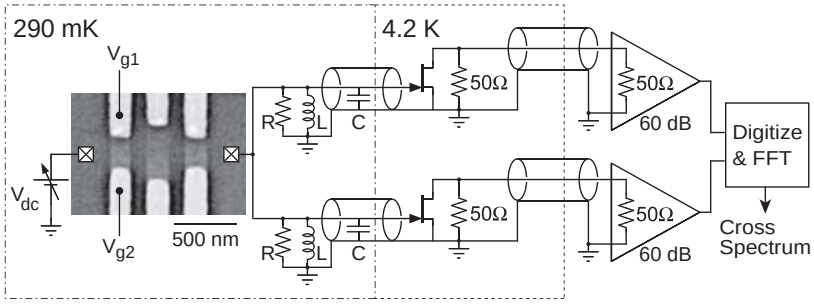


Figure 6.2: Equivalent circuit near 2 MHz of the system measuring QPC noise by cross-correlation on two amplification channels. The scanning electron micrograph shows a device of identical design to QPC 1. The QPC is formed by negative voltages $V_{\rm g1}$ and $V_{\rm g2}$ applied on two facing electrostatic gates. All other gates on the device are grounded.

noise as discussed in Refs. [58] and [60]. In the absence of $1/f$ and telegraph noise as well as bias-dependent electron heating, $S_I^{\rm P}$ originates from the electron partitioning at the QPC.

Experimental values for $S_I^{\rm P}$ are extracted from simultaneous measurements of cross-spectral density and of $g$ as described in Sec. 5.5.3. With an integration time of 60 s, the resolution in $S_I^{\rm P}$ is $1.4 \times 10^{-29}$ A$^2$/Hz, corresponding to full shot noise $2eI$ of $I \sim 40$ pA. $S_I^{\rm P}$ as a function of dc current $I$ for QPC 1 with gates set to very low conductance ($g_0 \sim 0.04 \times 2e^2/h$) [Fig. 6.3(b)] exhibits full shot noise, $S_I^{\rm P} = 2e|I|$, demonstrating an absence of $1/f$ and telegraph noise at the noise measurement frequency [70].

Figure 6.3(c) shows $S_I^{\rm P}(V_{\rm sd})$ in the $V_{\rm sd}$ range $-150$ $\mu$V to $+150$ $\mu$V [shaded regions in Figs. 6.1(b) and 6.1(c)], at $B_{\|} = 0$ and $V_{\rm g2}$ settings corresponding to open markers in Fig. 6.3(a). Similar to when the QPC is fully pinched off, $S_I^{\rm P}$ vanishes on plateaus of linear conductance. This demonstrates that bias-dependent electron heating is not significant in QPC 1. In contrast, for $g \sim 0.5$ and $1.5 \times 2e^2/h$, $S_I^{\rm P}$ grows with $|V_{\rm sd}|$ and shows a transition from quadratic to linear dependence [58, 59, 119]. The linear dependence of $S_I^{\rm P}$ on $V_{\rm sd}$ at high bias further demonstrates the absence of noise due to resistance fluctuations. Solid curves superimposed on the $S_I^{\rm P}(V_{\rm sd})$ data in Fig. 6.3(c) are best-fits to the form

$$S_I^{\rm P}(V_{\rm sd}) = 2\frac{2e^2}{h}\mathcal{N}\left[eV_{\rm sd}\coth\left(\frac{eV_{\rm sd}}{2k_BT_e}\right) - 2k_BT_e\right], \tag{6.1}$$

with the *noise factor* $\mathcal{N}$ as the only free fitting parameter. Note that $\mathcal{N}$ relates $S_I^{\rm P}$ to $V_{\rm sd}$,

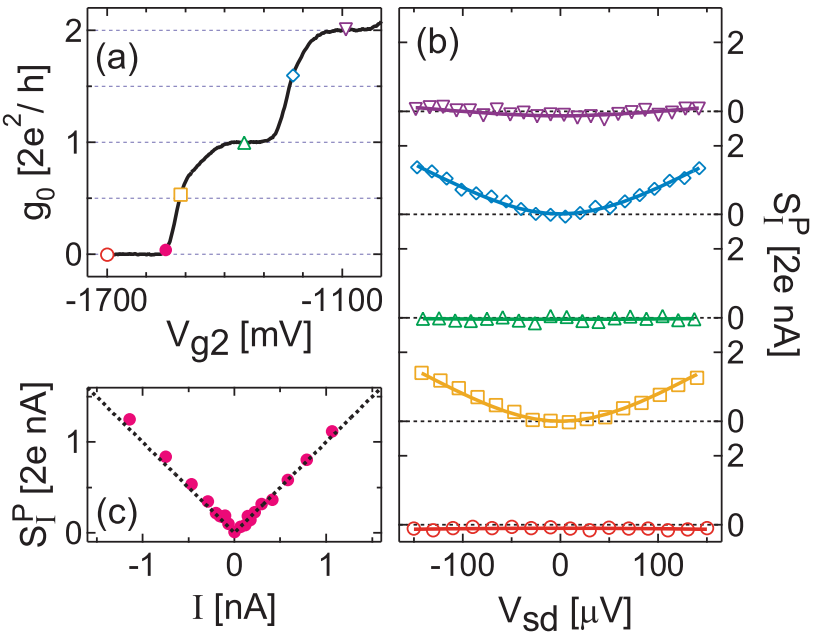


Figure 6.3: (a) Linear conductance $g_0$ as a function of $V_{g2}$ at $B_{\|} = 0$. Solid marker and open markers indicate $V_{g2}$ settings for the noise measurements shown in (b) and (c), respectively. (b) $S_I^P$ as a function of dc current $I$ with the QPC near pinch-off. The dotted line indicates full shot noise $S_I^P = 2e|I|$. (c) Measured $S_I^P$ as a function of $V_{sd}$, for conductances near 0 (circles), 0.5 (squares), 1 (upward triangles), 1.5 (squares), and 2 $\times 2e^2/h$ (downward triangles). Solid lines are best-fits to Eq. (6.1) using $\mathcal{N}$ as the only fitting parameter. In order of increasing conductance, best-fit $\mathcal{N}$ values are 0.00, 0.20, 0.00, 0.19, and 0.03.

in contrast to the Fano factor [39, 118], which relates $S_I^P$ to $I$. This fitting function is motivated by mesoscopic scattering theory [140, 141, 39, 118], where transport is described by transmission coefficients $\tau_{n,\sigma}$ ($n$ is the transverse mode index and $\sigma$ denotes spin) and partition noise originates from the partial transmission of incident electrons. Within scattering theory, the full expression for $S_I^P$ is

$$S_I^P(V_{sd}) = \frac{2e^2}{h} \int \sum_{n,\sigma} \tau_{n,\sigma}(\varepsilon)[1 - \tau_{n,\sigma}(\varepsilon)](f_s - f_d)^2 d\varepsilon, \tag{6.2}$$

where $f_{s(d)}$ is the Fermi function in the source (drain) lead. Equation (6.1) follows from Eq. (6.2) only for the case of constant transmission across the energy window of transport, with $\mathcal{N} = \frac{1}{2}\sum \tau_{n,\sigma}(1 - \tau_{n,\sigma})$. Furthermore, for spin-degenerate transmission, $\mathcal{N}$ vanishes at multiples of $2e^2/h$ and reaches the maximal value 0.25 at odd multiples of $0.5 \times 2e^2/h$. Energy dependence of transmission can reduce the maximal value below 0.25, as discussed

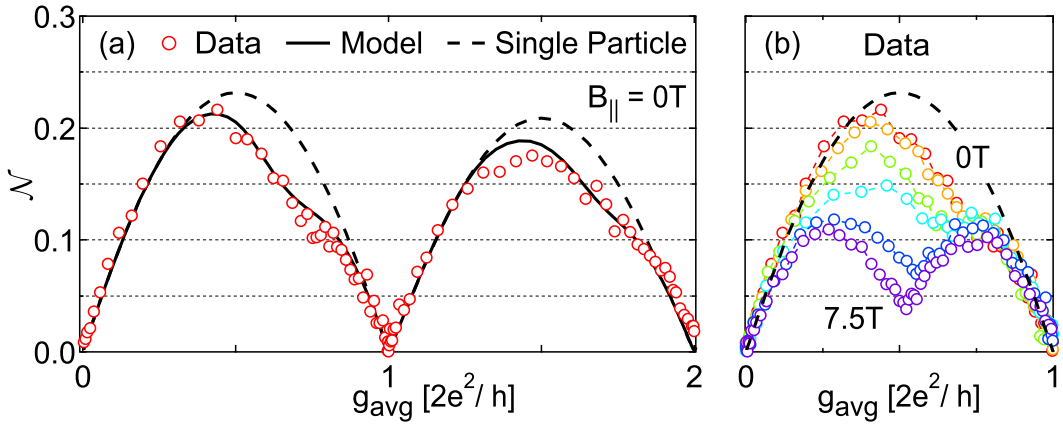


Figure 6.4: (a) Experimental $\mathcal{N}$ as a function of $g_{\rm avg}$ at $B_{\|} = 0$ (red circles) along with model curves for nonzero (solid) and zero (dashed) proportionality of splitting, $\gamma_n$ (see text). (b) Experimental $\mathcal{N}$ as a function of $g_{\rm avg}$ in the range $0 - 1 \times 2e^2/h$, at $B_{\|} = 0$ T (red), 2 T (orange), 3 T (green), 4 T (cyan), 6 T (blue), and 7.5 T (purple). The dashed curve shows the single-particle model ($\gamma_n = 0$) at zero field for comparison.

below.

While Eq. (6.1) is motivated by scattering theory, the value of $\mathcal{N}$ extracted from fitting to Eq. (6.1) simply provides a way to quantify $S_I^{\rm P}(V_{\rm sd})$ experimentally for each $V_{\rm g2}$. We have chosen the bias range $e|V_{\rm sd}| \lesssim 5k_BT_e$ for fitting $\mathcal{N}$ to minimize nonlinear-transport effects while extending beyond the quadratic-to-linear crossover in noise that occurs on the scale $e|V_{\rm sd}| \sim 2k_BT_e$.

The dependence of $\mathcal{N}$ on conductance at $B_{\|} = 0$ is shown in Fig. 6.4(a), where $\mathcal{N}$ is extracted from measured $S_I^{\rm P}(V_{\rm sd})$ at 90 values of $V_{\rm g2}$. The horizontal axis, $g_{\rm avg}$, is the average of the differential conductance over the bias points where noise was measured. $\mathcal{N}$ has the shape of a dome, reaching a maximum near odd multiples of $0.5 \times 2e^2/h$ and vanishing at multiples of $2e^2/h$. The observed $\mathcal{N}(g_{\rm avg})$ deviates from the spin-degenerate, energy-independent scattering theory in two ways. First, there is a reduction in the maximum amplitude of $\mathcal{N}$ below 0.25. Second, there is an asymmetry in $\mathcal{N}$ with respect to $0.5 \times 2e^2/h$, resulting from a noise reduction near the 0.7 feature. A similar but weaker asymmetry is observed about $1.5 \times 2e^2/h$. The reduction in the maximum amplitude can be understood

as resulting from an energy dependence of transmissions $\tau_{n,\sigma}$; the asymmetry is a signature of 0.7 structure, as we now discuss.

### 6.3.1 0.7 structure

We investigate further the relation between the asymmetry in $\mathcal{N}$ and the 0.7 structure by measuring the dependence of $\mathcal{N}(g_{\rm avg})$ on $B_\parallel$. As shown in Fig. 6.4(b), $\mathcal{N}$ evolves smoothly from a single asymmetric dome at $B_\parallel = 0$ to a symmetric double dome at 7.5 T. The latter is a signature of spin-resolved electron transmission. Notably, for $g_{\rm avg}$ between 0.7 and 1 (in units of $2e^2/h$), $\mathcal{N}$ is insensitive to $B_\parallel$, in contrast to the dependence of $\mathcal{N}$ near $0.3 \times 2e^2/h$.

We compare these experimental data to the shot-noise prediction of a phenomenological model [57] for the 0.7 anomaly. This model, originally motivated by dc transport data, assumes a lifting of the twofold spin degeneracy of mode $n$ by an energy splitting $\Delta\varepsilon_{n,\sigma} = \sigma \cdot \rho_n \cdot \gamma_n$ that grows linearly with 1D density $\rho_n$ (with proportionality $\gamma_n$) within that mode. Here, $\sigma = \pm 1$ and $\rho_n = \sqrt{2m^*}/h \sum_\sigma (\sqrt{\mu_{\rm s} - \varepsilon_{n,\sigma}} + \sqrt{\mu_{\rm d} - \varepsilon_{n,\sigma}})$, where $\mu_{\rm s(d)}$ is the source(drain) chemical potential and $m^*$ is the electron effective mass. Parameters of the phenomenological model are extracted solely from conductance. The lever arm converting $V_{\rm g2}$ to energy (and hence $\rho_n$) as well as the transverse mode spacing are extracted from transconductance ($dg/dV_{g2}$) data [Fig. 6.5(a)] [155]. Using an energy-dependent transmission $\tau_{n,\sigma}(\varepsilon) = 1/(1 + e^{2\pi(\varepsilon_{n,\sigma} - \varepsilon)/\hbar\omega_{x,n}})$ for a saddle-point potential [156], the value $\omega_{x,n}$ (potential curvature parallel to the current) is found by fitting linear conductance below $0.5 \times 2e^2/h$ (below $1.5 \times 2e^2/h$ for the second mode), and $\gamma_n$ is obtained by fitting above $0.5(1.5) \times 2e^2/h$, where (within the model) the splitting is largest [see Fig. 6.5(b)]. We find $\hbar\omega_{x,1(2)}$ is $\sim 500(300)$ $\mu$eV and $\gamma_{1(2)} \sim 0.012(0.008)$ $e^2/4\pi\epsilon_0$ for the first (second) mode. Note that the splitting $2 \cdot \rho_n \cdot \gamma_n$ is two orders of magnitude smaller than the direct Coulomb energy of electrons spaced by $1/\rho_n$. Using these parameters, $S_I^{\rm P}(V_{\rm sd})$ is calculated using Eq. (6.2), and $\mathcal{N}$ is then extracted by fitting $S_I^{\rm P}(V_{\rm sd})$ to Eq. (6.1). The calculated values of $\mathcal{N}(g_{\rm avg})$ at $B_\parallel = 0$ are shown along with the experimental data in Fig. 6.4(a). For compar-

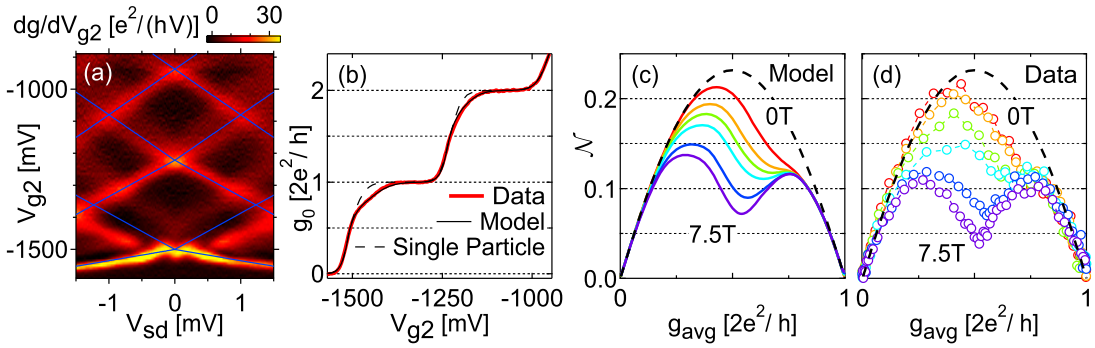


Figure 6.5: (a) Transconductance $dg/dV_{\rm g2}$ as a function of $V_{\rm sd}$ and $V_{\rm g2}$. Blue lines trace the alignment of mode edges with source and drain chemical potentials; their slope and intersection give the conversion from $V_{\rm g2}$ to energy and the energy spacing between modes, respectively. As two crossing points are observed between the first and second modes (the model attributes this to spin-splitting in the first mode), we take the midpoint as the crossing point for the blue lines. (c) Measured linear conductance (red) as a function of $V_{\rm g2}$ at $B_\parallel = 0$, and linear conductance calculated with the model (black solid) with best-fit values for $\omega_{x,n}$ and $\gamma_n$. Single-particle model takes $\gamma_n = 0$ (black dashed). (c) Model $\mathcal{N}$ as a function of $g_{\rm avg}$ in the range $0 - 1 \times 2e^2/h$, at $B_\parallel = 0$, 2, 3, 4, 6, and 7.5 T. (d) Same as Fig. 6.4(b).

ison we include calculation results accounting for energy-dependent transmission without splitting ($\gamma_n = 0$). The overall reduction of $\mathcal{N}$ arises from a variation in transmission across the 150 $\mu$V bias window (comparable to $\hbar\omega_x$), and is a single-particle effect. On the other hand, asymmetry of $\mathcal{N}$ about 0.5 and $1.5 \times 2e^2/h$ requires nonzero $\gamma_n$.

Magnetic field is included in the model by assuming a g-factor of 0.44 and adding the Zeeman splitting to the density-dependent splitting, maintaining the parameters obtained above. Figure 6.5(c) shows calculated $\mathcal{N}(g_{\rm avg})$ at $B_\parallel$ corresponding to the experimental data, reproduced in Fig. 6.5(d). Including the magnetic field in quadrature or as a thermally weighted mixture with the intrinsic density-dependent splitting gives essentially indistinguishable results within this model. Model and experiment show comparable evolution of $\mathcal{N}$ with $B_\parallel$: the asymmetric dome for $B_\parallel = 0$ evolves smoothly into a double dome for 7.5 T, and for conductance $\gtrsim 0.7 \times 2e^2/h$, the curves for all fields overlap closely. Some differences are observed between data and model, particularly for $B_\parallel = 7.5$ T. While the experimental double dome is symmetric with respect to the minimum at $0.5 \times 2e^2/h$, the

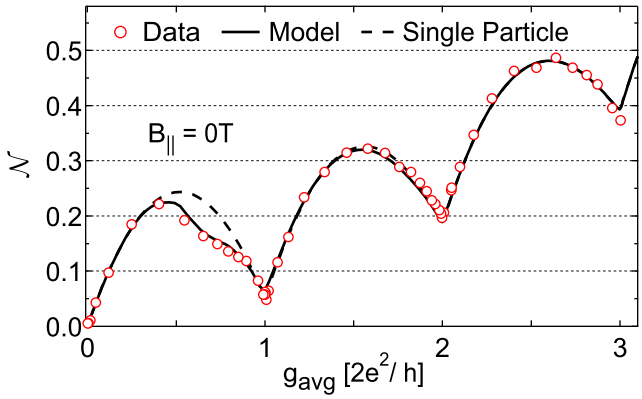


Figure 6.6: Experimental $\mathcal{N}$ as a function of $g_{\rm avg}$ at $B_{\|} = 0$ (red circles) for QPC 2, along with model curves for nonzero (solid) and zero (dashed) proportionality of splitting $\gamma_n$. Model calculations include bias-dependent electron heating.

theory curve remains slightly asymmetric with a less-pronounced minimum. We find that setting the g-factor to $\sim 0.6$ in the model reproduces the measured symmetrical double dome as well as the minimum value of $\mathcal{N}$ at $0.5 \times 2e^2/h$. This observation is consistent with reports of an enhanced g-factor in QPCs at low density [56, 145].

Recent theoretical treatments of 0.7 structure have also addressed its shot-noise signature. Modelling screening of the Coulomb interaction in the QPC, Lassl *et al.* [63] qualitatively reproduce the $B_{\|}$-dependent $\mathcal{N}$. Jaksch *et al.* [64] find a density-dependent splitting in density-functional calculations that include exchange and correlation effects. This theory justifies the phenomenological model and is consistent with the observed shot-noise suppression. Using a generalized single-impurity Anderson model motivated by density-functional calculations that suggest a quasi-bound state [61], Golub *et al.* [62] find quantitative agreement with the $B_{\|}$-dependent $\mathcal{N}$.

### 6.3.2 Bias-dependent electron heating

In contrast to QPC 1, noise data in QPC 2 show evidence of bias-dependent electron heating. Figure 6.6 shows $\mathcal{N}(g_{\rm avg})$ at $B_{\|} = 0$ over the first three conductance steps, extracted from fits using Eq. (6.1) to $S_I^{\rm P}(V_{\rm sd})$ data over the range $|V_{\rm sd}| \leq 400$ $\mu$V at 50

gate voltage settings. As in Fig. 6.4(a), a clear asymmetry in the noise factor is observed, associated with enhanced noise reduction near $0.7 \times 2e^2/h$. For this device, $\mathcal{N}$ remains finite on conductance plateaus, showing super-linear dependence on plateau index. This is consistent with bias-dependent thermal noise resulting from electron heating. Following Ref. [59], we incorporate into our model the bias-dependent electron temperature $T_e^*(V_{\rm sd}) = \sqrt{T_e^2 + (24/\pi^2)(g/g_m)(1 + 2g/g_m)(eV_{\rm sd}/2k_B)^2}$, where $g_m$ is the parallel conductance of the reservoirs connecting to the QPC. This expression [59] models diffusion by Wiedemann-Franz thermal conduction of the heat flux $gV_{\rm sd}^2/2$ on each side of the QPC and of Joule heating in the reservoirs, assuming ohmic contacts thermalized to the lattice at $T_e$. In the absence of independent measurements of reservoir and ohmic contact resistances, we treat $1/g_m$ as a single free parameter.

Theoretical $\mathcal{N}$ curves including effects of bias-dependent heating are obtained from fits to Eq. (6.1) of calculated $S_I(V_{\rm sd}, T_e^*(V_{\rm sd})) - 4k_B T_e g(V_{\rm sd})$. Parameters $\omega_{x,n} = 1.35,\ 1.13,\ 0.86$ meV and $\gamma_n = 0.019,\ 0.008,\ 0\ e^2/4\pi\epsilon_0$ for the first three modes (in increasing order) are extracted from conductance data. To avoid complications arising from a zero-bias anomaly [145] present in this device, $\gamma_0$ is extracted from the splitting of the first sub-band edge in the transconductance image [57], rather than from linear conductance. Other parameters are extracted in the same way as for QPC 1. As shown in Fig. 6.6, quantitative agreement with the $\mathcal{N}$ data is obtained over the three conductance steps with $1/g_m = 75\ \Omega$.

## 6.4 Conclusion and acknowledgements

We have presented measurements of current noise in quantum point contacts as a function of source-drain bias, gate voltage, and in-plane magnetic field. We have observed a shot-noise signature of the 0.7 structure at zero field, and investigated its evolution with increasing field into the signature of spin-resolved transmission. Comparison to a phenomenological model with density-dependent level splitting yielded quantitative agreement, and a device-specific

contribution to bias-dependent noise was shown to be consistent with electron heating.

We thank H.-A. Engel, M. Heiblum, L. Levitov, and A. Yacoby for valuable discussions, and S. K. Slater, E. Onitskansky, N. J. Craig, and J. B. Miller for device fabrication. We acknowledge support from NSF-NSEC, ARO/ARDA/DTO, and Harvard University.

# Chapter 7

# Tunable noise cross-correlations in a double quantum dot

D. T. McClure, L. DiCarlo, Y. Zhang, H.-A. Engel, C. M. Marcus
*Department of Physics, Harvard University, Cambridge, Massachusetts 02138*
M. P. Hanson, A. C. Gossard
*Department of Materials, University of California, Santa Barbara, California 93106*

We report measurements of the cross-correlation between temporal current fluctuations in two capacitively coupled quantum dots in the Coulomb blockade regime. The sign of the cross-spectral density is found to be tunable by gate voltage and source-drain bias. We find good agreement with the data by including inter-dot Coulomb interaction in a sequential-tunneling model.[1]

---

[1]This chapter is adapted with permission from Phys. Rev. Lett. **98**, 056801 (2007). © (2007) by the American Physical Society.

## 7.1 Introduction

Current noise cross-correlation in mesoscopic electronics, the fermionic counterpart of intensity-intensity correlation in quantum optics, is sensitive to quantum indistinguishability as well as many-body interactions [39, 46, 123, 51, 124, 125]. A distinctive feature of fermionic systems is that in the absence of interactions, noise cross-correlation is expected to always be negative [141, 53]. Experimentally, negative correlations have been observed in several solid-state Hanbury-Brown and Twiss-type noise measurements [129, 132, 130]. Since no sign constraint exists for interacting systems, a positive noise cross-correlation in a fermi system is a characteristic signature of interactions.

Sign reversal of noise cross-correlation has been the focus of recent theory and experiment [157, 158, 159, 160, 161, 162, 163, 164, 165, 166, 167, 168, 131, 71]. Theory indicates that positive cross-correlations can arise in the presence of BCS-like interaction [157, 158, 159], dynamical screening [160, 163], dynamical channel blockade [164, 165], and strong inelastic scattering [166, 163, 167, 168]. Experimentally, sign reversal of noise cross-correlation has been realized using a voltage probe to induce inelastic scattering [131], and in a beam-splitter geometry, where the sign reversal was linked to a crossover from sub- to super-Poissonian noise in a tunnel-barrier source [71]. This crossover was attributed to Coulomb interaction between naturally-occurring localized states in the tunnel barrier [70], as has been done in experiments on GaAs MESFETs [68] and stacked, self-assembled quantum dots [69]. In this chapter, we investigate gate-controlled sign reversal of noise cross-correlation in a simple four-terminal device. The structure consists of a parallel, capacitively coupled double quantum dot operated in the Coulomb blockade regime. In this configuration, the double dot acts as a pair of tunable interacting localized states, enabling a systematic study of Coulomb-induced correlation. Turning off inter-dot tunneling by electrically depleting the connection between dots ensures that indistinguishability (i.e., fermi statistics) alone cannot induce any cross-correlation; any cross-correlation, positive

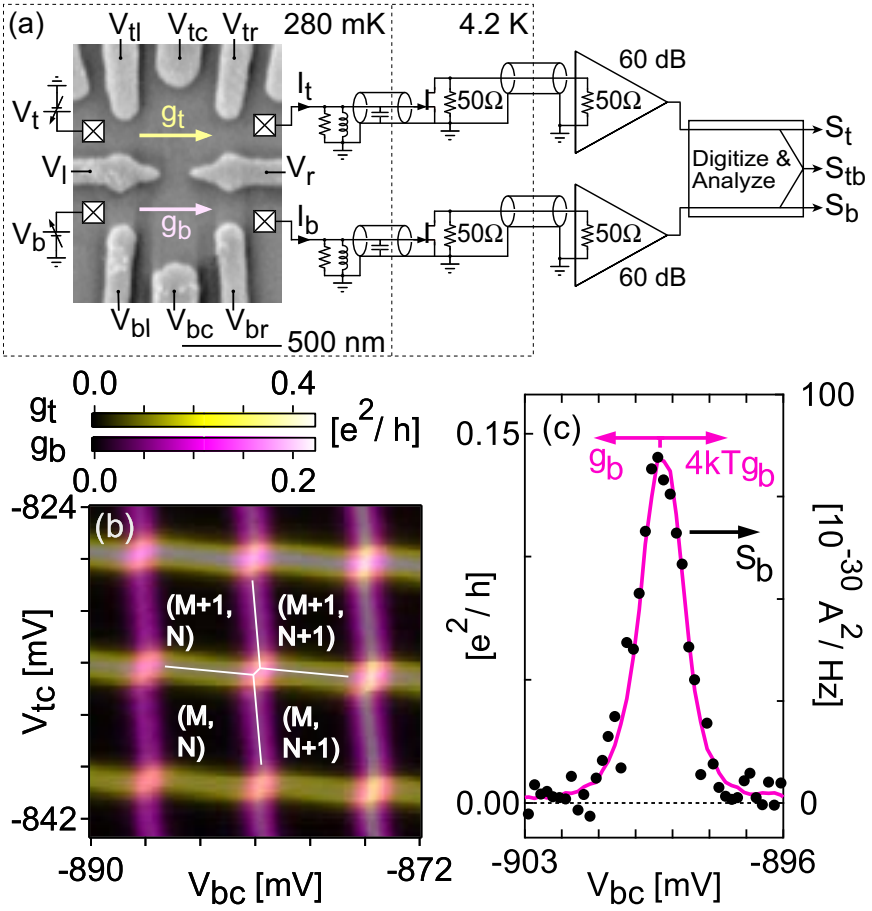


Figure 7.1: (a) Scanning electron micrograph of the double-dot device, and equivalent circuit at 2 MHz of the noise detection system measuring the power spectral densities and cross spectral density of fluctuations in currents $I_t$ and $I_b$. (b) Differential conductances $g_t$ (yellow) and $g_b$ (magenta) as a function of $V_{tc}$ and $V_{bc}$ over a few Coulomb blockade peaks in each dot, at $V_t = V_b = 0$. Black regions correspond to well-defined charge states in the double-dot system. Superimposed white lines indicate the honeycomb structure resulting from the finite inter-dot capacitive coupling. (c) Zero-bias (thermal) noise $S_b$ (black dots, right axis), conductance $g_b$ (magenta curve, left axis), and calculated $4k_BT_eg_b$ (magenta curve, right axis) as a function of gate voltage $V_{bc}$, with $V_{tc} = -852.2$ mV.

or negative, requires inter-dot Coulomb interaction. We find good agreement between the experimental results and a sequential-tunneling model of capacitively coupled single-level dots.

The four-terminal double-dot device [see Fig. 7.1(a)] is defined by top gates on a $GaAs/Al_{0.3}Ga_{0.7}As$ heterostructure grown by molecular beam epitaxy. The two-dimensional electron gas 100 nm below the surface has density $2\times10^{11}$ cm$^{-2}$ and mobility $2\times10^5$ cm$^2$/Vs.

Gate voltages $V_{\rm l} = V_{\rm r} = -1420$ mV fully deplete the central point contact, preventing inter-dot tunneling. Gate voltages $V_{\rm tl}$ ($V_{\rm bl}$) and $V_{\rm tr}$ ($V_{\rm br}$) control the tunnel barrier between the top (bottom) dot and its left and right leads. Plunger gate voltage $V_{\rm tc}$ ($V_{\rm bc}$) controls the electron number $M$ ($N$) in the top (bottom) dot; for this experiment $M \sim N \sim 100$. The lithographic area of each dot is 0.15 $\mu$m$^2$. We estimate level spacing $\Delta_{t(b)} \approx 70$ $\mu$eV in each dot, for $\sim 100$ nm depletion around the gates.

## 7.2 Methods

Measurements are performed in a $^3$He cryostat using a two-channel noise measurement system (Fig. 7.1(a)) [41]. A voltage bias $V_{\rm t}$ ($V_{\rm b}$) is applied to the left lead of the top (bottom) dot, with right leads grounded. Separate resistor-inductor-capacitor resonators ($R = 5$ k$\Omega$, $L = 66$ $\mu$H, $C = 96$ pF) convert fluctuations in currents $I_t$ and $I_b$ through the top and bottom dots around 2 MHz into voltage fluctuations on gates of high electron mobility transistors (HEMTs) at 4.2 K, which in turn produce current fluctuations in two 50 $\Omega$ coaxial lines extending to room temperature, where further amplification is performed. These signals are then simultaneously digitized at 10 MHz, their fast Fourier transforms calculated, and the current noise power spectral densities $S_{\rm t}, S_{\rm b}$ and cross-spectral density $S_{\rm tb}$ extracted following 15 s of integration, except for the data in Fig. 7.1(c), which was averaged for 50 s per point. The total gain of each amplification line and the base electron temperature $T_e = 280$ mK are calibrated *in situ* using Johnson-noise thermometry at base temperature and 1.6 K with the device configured as two point contacts [41]. Differential conductance $g_{\rm t}$ ($g_{\rm b}$) through the top (bottom) dot is measured using standard lock-in techniques with an excitation of 25 (30) $\mu V_{\rm rms}$ at 677 (1000) Hz. Ohmic contact resistances of roughly a few k$\Omega$, much less than the dot resistances, are not subtracted.

## 7.3 Double-dot characterization

Superposed top- and bottom-dot conductances $g_{\rm t}$ and $g_{\rm b}$ as a function of plunger voltages $V_{\rm tc}$ and $V_{\rm bc}$ form the characteristic double-dot honeycomb pattern [111, 108], with dark regions corresponding to well-defined electron number in each dot, denoted $(M, N)$ (first index for top dot), as shown in Fig. 7.1(b). Horizontal (vertical) features in $g_{\rm t}$ ($g_{\rm b}$) are Coulomb blockade (CB) conductance peaks [3], across which $M$ ($N$) increases by one as $V_{\rm tc}$ ($V_{\rm bc}$) is raised. The distance between triple points, i.e., the length of the short edge of the hexagon, provides a measure of the mutual charging energy $U$ due to inter-dot capacitive coupling. By comparing this distance to the CB peak spacing, and using the single-dot charging energy $E_C = 600$ $\mu$eV extracted from finite bias CB diamonds (not shown), we estimate $U \approx 60$ $\mu$eV [108]. We refer to the midpoint of the short edge of a hexagon, midway between triple points, as a "honeycomb vertex." Current noise $S_{\rm b}$ and conductance $g_{\rm b}$, measured simultaneously at zero dc bias, over a CB peak in the bottom dot (with the top dot in a CB valley) are shown in Fig. 7.1(c). Agreement between the measured $S_{\rm b}$ and the Johnson-Nyquist thermal noise value $4k_BT_eg_{\rm b}$ is observed.

## 7.4 Sign-reversal of noise cross correlation

Turning now to finite-bias noise measurements, Fig. 7.2(a) shows the measured cross-correlation $S_{\rm tb}$ as a function of plunger gate voltages $V_{\rm tc}$ and $V_{\rm bc}$, in the vicinity of a honeycomb vertex, with voltage bias of $-100$ $\mu$V applied to both dots. The plot reveals a characteristic quadrupole pattern of cross-correlation centered on the honeycomb vertex, comprising regions of both negative and positive cross-correlation. Similar patterns are observed at all other honeycomb vertices. The precise symmetry of the pattern is found to depend rather sensitively on the relative transparency of each dot's left and right tunnel barriers. Away from the vertices, noise cross-correlation vanishes.

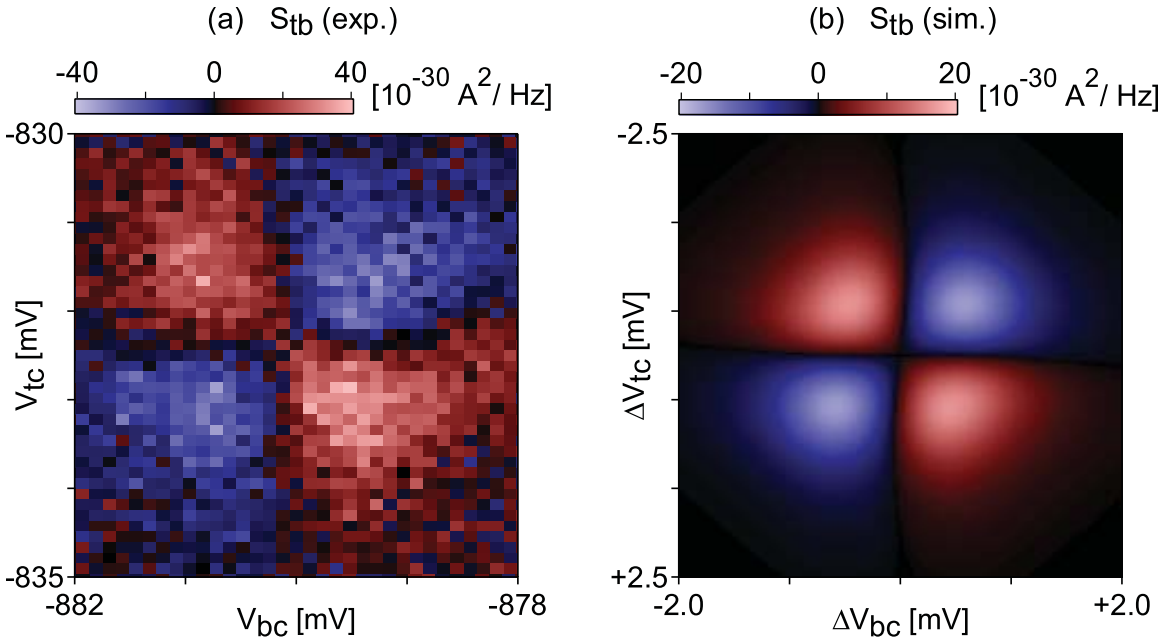


Figure 7.2: Measured (a) and simulated (b) cross-spectral density $S_{\rm tb}$ near a honeycomb vertex, with applied bias $V_{\rm t} = V_{\rm b} = -100$ $\mu$V ($e|V_{t(b)}| \approx 4k_BT_e \approx E_C/6$). Blue regions (lower-left and upper-right) indicate negative $S_{\rm tb}$, while red regions indicate positive $S_{\rm tb}$.

## 7.5 Master equation simulation

To better understand this experimental result, we model the system as single-level dots capacitively coupled by a mutual charging energy $U$, each with weak tunneling to the leads. The energy needed to add electron $M+1$ to the top dot depends on the two plunger gate voltages as well as the electron number $n \in \{N, N+1\}$ on the bottom dot: $E_t = \alpha_t V_{\rm tc} + \beta_t V_{\rm bc} + U \cdot n + \text{const.}$, where lever arms $\alpha_t$ and $\beta_t$ are obtained from the honeycomb plot in Fig. 7.1(b) [111] and the measured $E_C$. The energy $E_b$ to add electron $N+1$ to the bottom dot is given by an analogous formula. Occupation probabilities for charge states $(M, N)$, $(M+1, N)$, $(M, N+1)$, and $(M+1, N+1)$ are given by the diagonal elements of the density matrix, $\rho = (\rho_{00}, \rho_{10}, \rho_{01}, \rho_{11})^T$. The time evolution of $\rho$ is given by

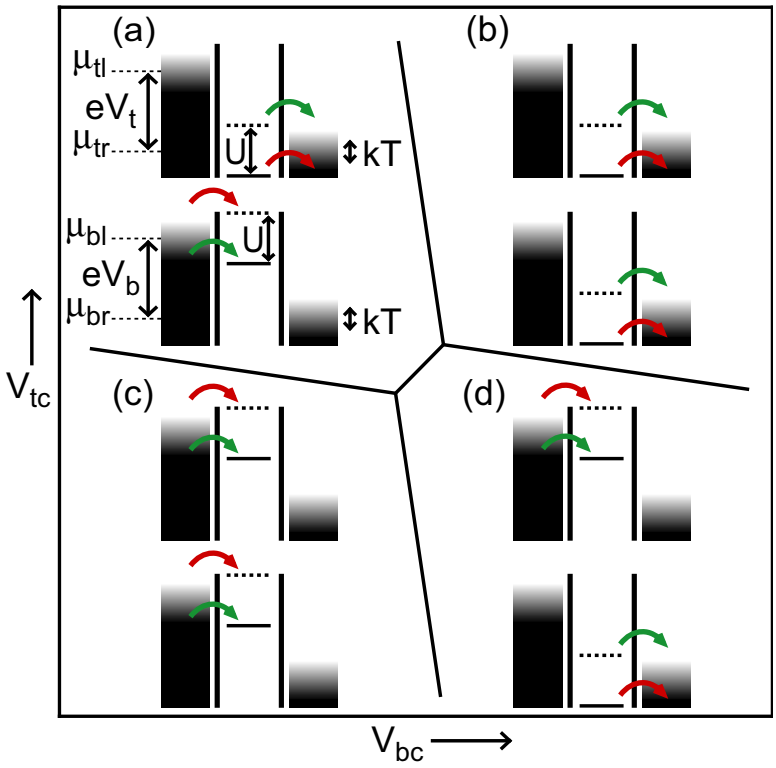


Figure 7.3: Energy level diagrams in the vicinity of a honeycomb vertex, with biases $V_{t(b)} = -100\ \mu$V. (The various energies are shown roughly to scale.) The solid horizontal line in the top (bottom) dot represents the energy $E_{t(b)}$ required to add electron $M+1$ $(N+1)$ when the bottom (top) dot has $N$ $(M)$ electrons. The dashed horizontal line, higher than the solid line by $U$, represents $E_{t(b)}$ when the bottom (top) dot has $N+1$ $(M+1)$ electrons. In each dot, the rate of either tunneling-in from the left or tunneling-out to the right is significantly affected by this difference in the energy level, taking on either a slow value (red arrow) or a fast value (green arrow) depending on the electron number in the other dot. In (a) and (d), where the occurrence of each $U$-sensitive process enhances the rate of the other, we find positive cross-correlation. In (b) and (c), where the occurrence of each $U$-sensitive process suppresses the rate of the other, we find negative cross-correlation.

a master equation $d\rho/dt = \mathcal{M}\rho$, where

$$\mathcal{M} = \begin{pmatrix} -W_{00}^{\text{out}} & W_{00\leftarrow 10} & W_{00\leftarrow 01} & 0 \\ W_{10\leftarrow 00} & -W_{10}^{\text{out}} & 0 & W_{01\leftarrow 11} \\ W_{01\leftarrow 00} & 0 & -W_{01}^{\text{out}} & W_{10\leftarrow 11} \\ 0 & W_{11\leftarrow 10} & W_{11\leftarrow 01} & -W_{11}^{\text{out}} \end{pmatrix}. \tag{7.1}$$

Each diagonal term of $\mathcal{M}$ gives the total loss rate for the corresponding state: $W_{\alpha}^{\text{out}} = \sum_{\beta} W_{\beta\leftarrow\alpha}$. Off-diagonal terms give total rates for transitions between two states. For

example, $W_{10\leftarrow 00} = W^l_{10\leftarrow 00} + W^r_{10\leftarrow 00}$ is the total tunneling rate into $(M+1, N)$ from $(M, N)$, combining contributions from the top-left and top-right leads.

Rates for tunneling between a dot and either of its leads $i \in \{tl, tr, bl, br\}$ depend on both the transparency $\Gamma^i$ of the tunnel barrier to lead $i$ and the Fermi function $f_i(\epsilon) = [1 + \exp\{(\epsilon - \mu_i)/k_B T_e\}]^{-1}$ evaluated at $\epsilon = E_{t(b)}$, where $\mu_i$ is the chemical potential in lead $i$. For example, the rates for tunneling into and out of the top dot from/to the left lead are given by $W^l_{10\leftarrow 00} = \Gamma^{lt} f_{lt}(E_t)$ and $W^l_{00\leftarrow 10} = \Gamma^{lt}[1 - f_{lt}(E_t)]$, respectively. As $E_t$ is lowered across $\mu_{lt}$, $W^l_{10\leftarrow 00}$ increases from 0 to $\Gamma^{lt}$ over a range of a few $k_B T_e$, while $W^l_{00\leftarrow 10}$ does the opposite.

We obtain the steady-state value of $\rho$, denoted $\bar{\rho}$, by solving $\mathcal{M}\bar{\rho} = 0$. Following Refs. [169, 170, 171], we define current matrices $J^{tr}$ and $J^{br}$ for the top- and bottom-right leads, with elements $J^{tr}_{mn,m'n'} = |e|\delta_{nn'}(m - m')W^r_{mn\leftarrow m'n'}$ and $J^{br}_{mn,m'n'} = |e|\delta_{mm'}(n - n')W^r_{mn\leftarrow m'n'}$. We next obtain the average currents $\langle I_{t(b)}\rangle = \sum_i [J^{t(b)r}\bar{\rho}]_i$ and the correlator $\langle I_{\rm t}(\tau) I_{\rm b}(0)\rangle = \sum_i \left[\theta(\tau) J^{\rm tr} e^{\mathcal{M}\tau} J^{\rm br}\bar{\rho} + \theta(-\tau) J^{\rm br} e^{\mathcal{M}\tau} J^{\rm tr}\bar{\rho}\right]_i$ ($\theta$ is the Heaviside step function). The cross-spectral density in the low-frequency limit is then given by $S_{\rm tb} = 2\int_{-\infty}^{\infty} [\langle I_{\rm t}(\tau) I_{\rm b}(0)\rangle - \langle I_{\rm t}\rangle\langle I_{\rm b}\rangle]\, d\tau$. See App. C for an implementation of this code in MATLAB.[2]

Simulation results for cross-correlation $S_{\rm tb}$ as a function of plunger gate voltages are shown in Fig. 7.2(b), with all parameters of the model extracted from experiment: $U = 60\ \mu$eV, $T_e = 280$ mK, $\Gamma^{tl} = \Gamma^{tr} = 1.5\times 10^{10}\ \mathrm{s}^{-1}$, and $\Gamma^{bl} = \Gamma^{br} = 7.2\times 10^{9}\ \mathrm{s}^{-1}$. The $\Gamma^i$ were estimated from the zero-bias conductance peak height using Eq. (6.3) of Ref. [172], taking left and right barriers equal. The simulation shows the characteristic quadrupole pattern of positive and negative cross-correlation, as observed experimentally. We note that the model underestimates $S_{\rm tb}$ by roughly a factor of two. This may be due to transport processes not accounted for in the model. For instance, elastic cotunneling should be present since the $\Gamma^i$

[2]MATLAB is produced by The MathWorks, Inc. (http://mathworks.com/).

are comparable to $k_B T_e/\hbar$. Also, since the voltage-bias energy $|eV_{t(b)}|$ is greater than the level spacing $\Delta_{t(b)}$, transport may occur via multiple levels [173, 164, 165, 121] and inelastic cotunneling [174, 175, 122].

Intuition for how Coulomb interaction in the form of capacitive inter-dot coupling can lead to the observed noise cross-correlation pattern can be gained by examining energy levels in both dots in the space of plunger gate voltages, as shown in Fig. 7.3. With both dots tuned near Coulomb blockade peaks, the fluctuations by one in the electron number of each dot, caused by the sequential tunneling of electrons through that dot, cause the energy level of the other dot to fluctuate between two values separated by $U$. These fluctuations can raise and lower the level across the chemical potential in one of the leads of the dot, strongly affecting either the tunnel-in rate (from the left, for the case illustrated in Fig. 7.3) or the tunnel-out rate (to the right) of that dot. Specifically, the rate of the "$U$-sensitive" process in each dot fluctuates between a slow rate (red arrow), suppressed well below $\Gamma^i$, and a fast rate (green arrow), comparable to $\Gamma^i$. For balanced right and left $\Gamma^i$ in each dot, the $U$-sensitive process becomes the transport bottleneck when its rate is suppressed.

These $U$-sensitive processes correlate transport through the dots. In region (b) of Fig. 7.3, for instance, where $S_{\rm tb}$ is negative, the $U$-sensitive process in each dot is tunneling-out. Here and in (c), where the $U$-sensitive process in each dot is tunneling-in, the $U$-sensitive processes compete: occurrence of one suppresses the other, leading to negative $S_{\rm tb}$. Conversely, in region (a) [(d)], where $S_{\rm tb}$ is positive, the top [bottom] dot's $U$-sensitive process is tunneling-out, but the bottom [top] dot's is tunneling-in. Here, the $U$-sensitive processes cooperate: occurrence of one lifts the suppression of the other, leading to positive $S_{\rm tb}$.

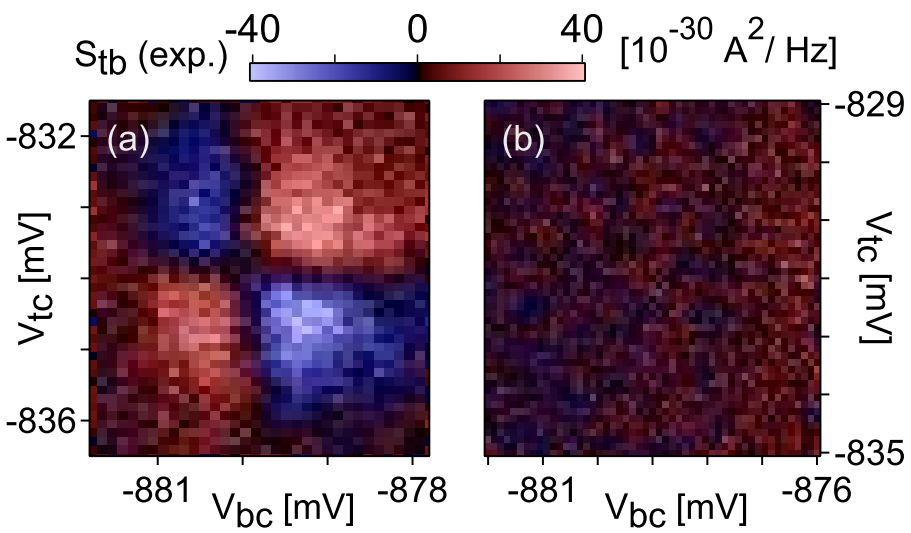


Figure 7.4: (a) Measured $S_{\rm tb}$ near a honeycomb vertex, with opposite biases $V_{\rm t} = -V_{\rm b} = -100$ $\mu$V. Note that the pattern is reversed from Fig. 7.2(a): negative cross-correlation (blue) is now found in the upper-left and lower-right regions, while positive cross-correlation (red) is now found in the lower-left and upper-right. (b) Measured $S_{\rm tb}$ near a honeycomb vertex, with $V_{\rm t} = V_{\rm b} = 0$. Cross-correlation vanishes at zero bias, though the noise in each dot is finite.

## 7.6 Some additional checks

The arguments above also apply when one or both biases are reversed. When both are reversed, we find both experimentally and in the model that the same cross-correlation pattern as in Fig. 7.2 appears (not shown). When only one of the biases is reversed, we find both experimentally [as shown in Fig. 7.4(a)] and in the model that the pattern reverses sign. In the absence of any bias, cross-correlation vanishes both experimentally [as shown in Fig. 7.4(b)] and in the model, despite the fact that noise in the individual dots remains finite [as seen in Fig. 7.1(c)].

## 7.7 Conclusion and acknowledgements

We have observed gate-controlled sign reversal of noise cross-correlation in a double quantum dot in the Coulomb blockade regime with purely capacitive inter-dot coupling. Experimental observations are in good agreement with a sequential-tunneling model, and can

be understood from an intuitive picture of mutual charge-state-dependent tunneling. This study, notable for the simplicity and controllability of the device, may be particularly useful for understanding current noise in systems where interacting localized states occur naturally and uncontrollably.

We thank N. J. Craig for device fabrication and M. Eto, W. Belzig, C. Bruder, E. Sukhorukov, and L. Levitov for valuable discussions. We acknowledge support from the NSF through the Harvard NSEC, PHYS 01-17795, DMR-05-41988, DMR-0501796, as well as support from NSA/DTO and Harvard University.

# Chapter 8

# Noise correlations in a Coulomb blockaded quantum dot

Yiming Zhang, L. DiCarlo, D. T. McClure, C. M. Marcus
*Department of Physics, Harvard University, Cambridge, Massachusetts 02138, USA*
M. Yamamoto, S. Tarucha
*Department of Applied Physics, University of Tokyo, Bunkyoku, Tokyo 113-8656, Japan*
*ICORP-JST, Atsugi-shi, Kanagawa 243-0198, Japan*
M. P. Hanson, A. C. Gossard
*Department of Materials, University of California, Santa Barbara, California 93106, USA*

We report measurements of current noise auto- and cross correlation in a tunable quantum dot with two or three leads. As the Coulomb blockade is lifted at finite source-drain bias, the auto-correlation evolves from super-Poissonian to sub-Poissonian in the two-lead case, and the cross correlation evolves from positive to negative in the three-lead case, consistent with transport through multiple levels. Cross correlations in the three-lead dot are found to be proportional to the noise in excess of the Poissonian value in the limit of weak output tunneling.[1]

---

[1]This chapter is adapted with permission from Phys. Rev. Lett. **99**, 036603 (2007). © (2007) by the American Physical Society.

## 8.1 Introduction

Considered individually, Coulomb repulsion and Fermi statistics both tend to smooth electron flow, thereby reducing shot noise below the uncorrelated Poissonian limit [39, 46, 141, 53]. For similar reasons, Fermi statistics without interactions also induces a negative noise cross correlation in multiterminal devices [39, 141, 53, 129, 132]. It is therefore surprising that under certain conditions, the interplay between Fermi statistics and Coulomb interaction can lead to electron bunching, i.e., super-Poissonian auto-correlation and positive cross correlation of electronic noise.

The specific conditions under which such positive noise correlations can arise has been the subject of numerous theoretical [176, 166, 163, 167, 168, 174, 171, 173, 164, 165, 175] and experimental [176, 68, 69, 70, 71, 131, 122, 121, 177, 66] studies in the past few years. Super-Poissonian noise observed in metal-semiconductor field effect transistors [68], tunnel barriers [70] and self-assembled stacked quantum dots [69] has been attributed to interacting localized states [170, 171, 68] occurring naturally in these devices. In more controlled geometries, super-Poissonian noise has been associated with inelastic cotunneling [174] in a nanotube quantum dot [122], and with dynamical channel blockade [173, 164, 165] in GaAs/AlGaAs quantum dots in the weak-tunneling [121] and quantum Hall regimes [177]. Positive noise cross correlation has been observed in a capacitively coupled double dot [66] as well as in electronic beam splitters following either an inelastic voltage probe [131, 166, 163, 167, 168] or a super-Poissonian noise source [71]. The predicted positive noise cross correlation in a three-lead quantum dot [164, 165] has not been reported experimentally to our knowledge.

This chapter describes measurement of current noise auto- and cross correlation in a Coulomb-blockaded quantum dot configured to have either two or three leads. As a function of gate voltage and bias, regions of super- and sub-Poissonian noise, as well as positive and negative noise cross correlation, are identified. Results are in good agreement with a multi-

level sequential-tunneling model in which electron bunching arises from dynamical channel blockade [173, 164, 165]. For weak-tunneling output leads, noise cross correlation in the three-lead configuration is found to be proportional to the deviation of the auto-correlation from the Poissonian value (either positive or negative) similar to the relation found in electronic Hanbury Brown–Twiss (HBT)–type experiments [129, 132, 71].

## 8.2 Device

The quantum dot is defined by gates on the surface of a $GaAs/Al_{0.3}Ga_{0.7}As$ heterostructure [Fig. 8.1(a)]. The two-dimensional electron gas 100 nm below the surface has density $2 \times 10^{11}$ cm$^{-2}$ and mobility $2 \times 10^5$ cm$^2$/Vs. Leads formed by gate pairs $V_{\rm l}$-$V_{\rm bl}$, $V_{\rm r}$-$V_{\rm br}$, and $V_{\rm l}$-$V_{\rm r}$ connect the dot to three reservoirs labeled 0, 1, and 2, respectively. Plunger gate voltage $V_{\rm bc}$ controls the electron number in the dot, which we estimate to be $\sim 100$. The constriction formed by $V_{\rm tl}$-$V_{\rm l}$ is closed.

## 8.3 Methods

A $^3$He cryostat is configured to allow simultaneous conductance measurement near dc and noise measurement near 2 MHz [41]. For dc measurements, the three reservoirs are each connected to a voltage amplifier, a current source, and a resistor to ground ($r = 5$ k$\Omega$). The resistor $r$ converts the current $I_\alpha$ out of reservoir $\alpha$ to a voltage signal measured by the voltage amplifier; it also converts the current from the current source to a voltage excitation $V_\alpha$ applied at reservoir $\alpha$. The nine raw differential conductance matrix elements $\tilde{g}_{\alpha\beta} = dI_\beta/dV_\alpha$ are measured simultaneously with lock-in excitations of 20 $\mu$V$_{\rm rms}$ at 44, 20 and 36 Hz on reservoirs 0, 1 and 2, respectively. Subtracting $r$ from the matrix $\tilde{\mathbf{g}}$ yields the intrinsic conductance matrix $\mathbf{g} = [\mathbf{E} + r\tilde{\mathbf{g}}]^{-1} \cdot \tilde{\mathbf{g}}$, where $\mathbf{E}$ is the identity matrix. Ohmic contact resistances ($\sim 10^3$ $\Omega$) are small compared to dot resistances ($\gtrsim 10^5$ $\Omega$), and are neglected in the analysis. Values for the currents $I_\alpha$ with bias $V_0$ applied to reservoir 0 are

obtained by numerically integrating $\tilde{g}_{0\alpha}$.

Fluctuations in currents $I_1$ and $I_2$ are extracted from voltage fluctuations around 2 MHz across separate resistor-inductor-capacitor (RLC) resonators [Fig. 8.1(a)]. Power spectral densities $S_{\mathrm{V}1,2}$ and cross-spectral density $S_{\mathrm{V}12}$ of these voltage fluctuations [41] are averaged over 20 s, except where noted. Following the calibration of amplifier gains and electron temperature $T_e$ using noise thermometry [41], the dot's intrinsic current noise power spectral densities $S_{1,2}$ and cross-spectral density $S_{12}$ are extracted by solving the Langevin [39] equations that take into account the feedback [167] and thermal noise from the finite-impedance external circuit:

$$\begin{aligned} S_1 &= a_{11}^2 S_{V1} + a_{21}^2 S_{V2} + 2a_{11}a_{21}S_{V12} - 4k_B T_e/R \\ S_2 &= a_{12}^2 S_{V1} + a_{22}^2 S_{V2} + 2a_{12}a_{22}S_{V12} - 4k_B T_e/R \\ S_{12} &= a_{11}a_{12}S_{V1} + a_{21}a_{22}S_{V2} + (a_{11}a_{22} + a_{12}a_{21})S_{V12}, \end{aligned}$$

where $a_{11(22)} = 1/R - g_{11(22)}$, $a_{12(21)} = -g_{12(21)}$ and $R$ is the RLC resonator parallel resistance.

## 8.4 Noise in the two-lead configuration

Figure 8.1(b) shows conductance $g_{01}$ as a function of $V_{\mathrm{bc}}$ and $V_0$ in a two-lead configuration, i.e., with the $V_{\mathrm{l}}$-$V_{\mathrm{r}}$ constriction closed. The characteristic Coulomb blockade (CB) diamond structure yields a charging energy $E_{\mathrm{C}} = 0.8$ meV and lever arm for the plunger gate $\eta_{\mathrm{bc}} = \Delta\varepsilon_d/(e\Delta V_{\mathrm{bc}}) = 0.069$, where $\varepsilon_d$ is the dot energy. The diamond tilt $\eta_{\mathrm{bc}}/(1/2 - \eta_0)$ gives the lever arm for reservoir 0: $\eta_0 = \Delta\varepsilon_d/(e\Delta V_0) = 0.3$. As shown in Fig. 8.1(d), current noise $S_1$ along selected cuts close to the zero-bias CB peak (red, orange cuts) is below the Poissonian value $2e|I_1|$ at all biases $|I_1|$, while cuts that pass inside the CB diamond (green, blue cuts) exceed $2e|I_1|$ at low currents, then drop below $2e|I_1|$ at high currents. At finite $T_e$, the current noise $S_1^{\mathrm{P}} = 2eI_1 \coth(eV_0/2k_B T_e)$ of an ideal Poissonian noise source at bias $V_0$ may exceed $2e|I_1|$ due to the thermal (Johnson) noise contribution [174]. Accordingly, we

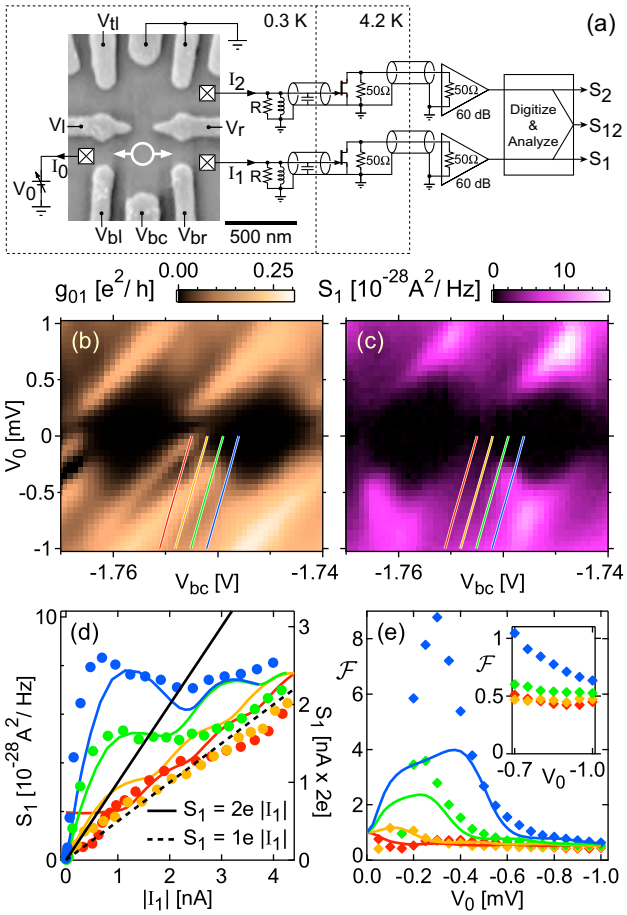


Figure 8.1: (a) Micrograph of the device and equivalent circuit near 2 MHz of the noise detection system (see text for equivalent circuit near dc). For the data in Figs. 8.1 and 8.2, the $V_{\rm l}$-$V_{\rm r}$ constriction is closed and the dot is connected only to reservoirs 0 and 1. (b, c) Differential conductance $g_{01}$ and current noise spectral density $S_1$, respectively, as a function of $V_0$ and $V_{\rm bc}$. (d) $S_1$ versus $|I_1|$ data (circles) and multi-level simulation (solid curves) along the four cuts indicated in (b) and (c) with corresponding colors. Black solid (dashed) line indicates $S_1 = 2e|I_1|$ ($S_1 = 1e|I_1|$). (e) Data (diamonds) and multi-level simulation (solid curves) of the modified Fano factor $\mathcal{F}$ along the same cuts as taken in (d). Inset: detail of $\mathcal{F}$ at high $|V_0|$.

define a modified Fano factor $\mathcal{F} \equiv S_1/S_1^{\rm P}$. Figure 8.1(e) shows regions of super-Poissonian noise ($\mathcal{F} > 1$) when the green and blue cuts are within the CB diamond. For all cuts, $\mathcal{F}$ approaches 1/2 at large bias.

Current noise can also be identified as sub- or super-Poissonian from the excess Poissonian noise $S_1^{\rm EP} \equiv S_1 - S_1^{\rm P}$ being negative or positive, respectively. Unlike $\mathcal{F}$, $S_1^{\rm EP}$ does not have divergent error bars inside the CB diamond, where currents vanish. As shown in

Fig. 8.2(a), in regions where both $I_1$ and $S_1$ vanish, $S_1^{\rm EP}$ also vanishes. Far outside the CB diamonds, $S_1^{\rm EP}$ is negative, indicating sub-Poissonian noise. However, $S_1^{\rm EP}$ becomes positive along the diamond edges, indicating super-Poissonian noise in these regions.

We next compare our experimental results to single-level and multi-level sequential-tunneling models of CB transport. The single-level model yields exact expressions for average current and noise [39, 46, 175, 178]: $I_1 = (e/h)\int d\varepsilon \gamma_0\gamma_1(f_1 - f_0)/[(\gamma_1+\gamma_0)^2/4 + (\varepsilon-\varepsilon_d)^2]$, $S_1 = (2e^2/h)\int d\varepsilon\{\gamma_0^2\gamma_1^2\cdot[f_0(1-f_0)+f_1(1-f_1)] + \gamma_0\gamma_1[(\gamma_1-\gamma_0)^2/4 + (\varepsilon-\varepsilon_d)^2]\cdot[f_0(1-f_1)+f_1(1-f_0)]\}/[(\gamma_1+\gamma_0)^2/4+(\varepsilon-\varepsilon_d)^2]^2$, where $\gamma_{0(1)}$ is the tunneling rate to reservoir 0(1) and $f_{0(1)}$ is the Fermi function in reservoir 0(1). The dot energy $\varepsilon_d$ is controlled by gate and bias voltages: $\varepsilon_d = -eV_{\rm bc}\eta_{\rm bc} - eV_0\eta_0 - eV_1\eta_1 + \text{const}$. For the multi-level sequential-tunneling model, a master equation is used to calculate current and noise, following Refs. [173, 164, 165, 169]. To model transport, we assume simple filling of orbital levels and consider transitions to and from $N$-electron states that differ in the occupation of at most $n$ levels above (indexed 1 through $n$) and $m$ levels below (indexed $-1$ through $-m$) the highest occupied level in the $(N+1)$-electron ground state (level 0). For computational reasons, we limit the calculation to $n = m = 3$. For simplicity, we assume equal level spacings, symmetric tunnel barriers, and an exponential dependence of the tunneling rates on level energy: $\Delta\varepsilon^l \equiv \varepsilon_d^l - \varepsilon_d^0 = l\times\delta$ and $\gamma_0^l = \gamma_1^l = \Gamma\exp(\kappa\Delta\varepsilon^l)$, where $l = -3, ..., 0, ..., 3$ is the level index, $\varepsilon_d^l$ is the energy of level $l$, and $\gamma_{0(1)}^l$ is the tunneling rate from level $l$ to reservoir 0(1). We choose $\delta = 150$ $\mu$eV, $\Gamma = 15$ GHz and $\kappa = 0.001$ $(\mu\text{eV})^{-1}$ to fit the data in Figs. 8.1(d) and 8.1(e).

Super-Poissonian noise in the multi-level model arises from *dynamical channel blockade* [173, 164, 165], illustrated in the diagrams in Fig. 8.2. Consider, for example, the energy levels and transport processes shown in the green-framed diagram, which corresponds to the location of the green dot on the lower-right edge in Fig. 8.2(c). Along that edge, the transport involves transitions between the $N$-electron ground state and $(N+1)$-electron ground or excited states. When an electron occupies level 0, it will have a relatively long lifetime,

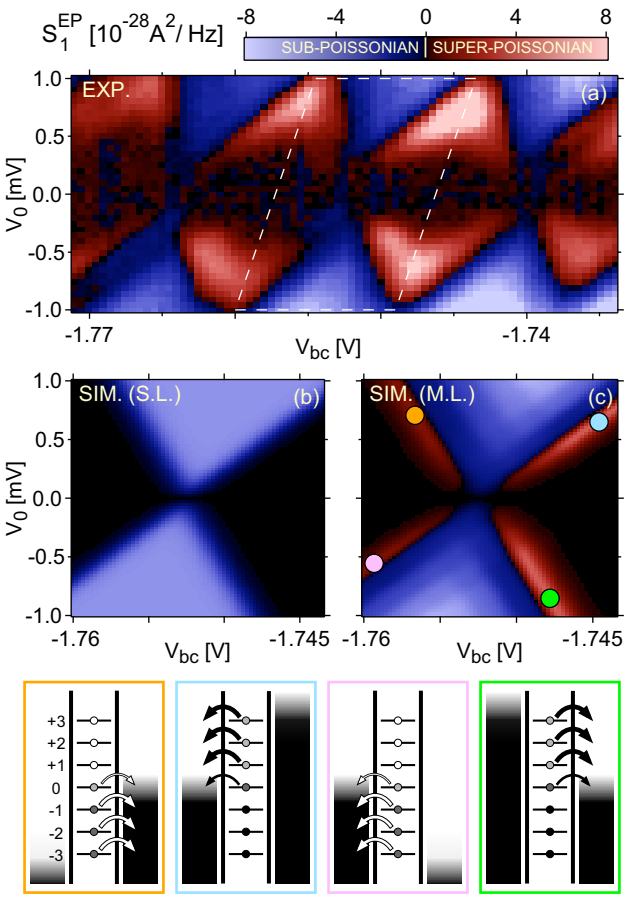


Figure 8.2: (a) Excess Poissonian noise $S_1^{\mathrm{EP}}$ as a function of $V_0$ and $V_{\mathrm{bc}}$. Red (blue) regions indicate super(sub)-Poissonian noise. (b, c) Single-level (S.L.) and multi-level (M.L.) simulation of $S_1^{\mathrm{EP}}$, respectively, corresponding to the data region enclosed by the white dashed parallelogram in (a). At the four colored dots superimposed on (c), where $S_1^{\mathrm{EP}}$ is most positive, energy diagrams are illustrated in the correspondingly colored frames at the bottom. In these diagrams, black (white) arrows indicate electron (hole) transport; the greyscale color in the reservoirs and inside the circles on each level indicates electron population, the darker the higher.

as tunneling out is suppressed by the finite electron occupation in reservoir 1 at that energy. During this time, transport is blocked since the large charging energy prevents more than one non-negative-indexed level from being occupied at a time. This blockade happens dynamically during transport, leading to electron bunching and thus to super-Poissonian noise. At the location of the pink dot on the lower-left edge in Fig. 8.2(c), the transport involves transitions between the $(N+1)$-electron ground state and $N$-electron ground or excited states; a similar dynamical blockade occurs in a complementary hole transport pic-

ture. The hole transport through level 0 is slowed down by the finite hole occupation in reservoir 0, modulating the hole transport through negative-indexed levels, thus leading to hole bunching and super-Poissonian noise. Transport at the blue (orange) dot is similar to transport at the green (pink) dot, but with the chemical potentials in reservoirs 0 and 1 swapped. Both experimentally and in the multi-level simulation, $S_1^{\mathrm{EP}}$ is stronger along electron edges than along hole edges. This is due to the energy dependence of the tunneling rates: since the positive-indexed electron levels have higher tunneling rates than the negative-indexed hole levels, the dynamical modulation is stronger for electron transport than for hole transport.

## 8.5 Noise in the three-lead configuration

We next investigate the three-lead configuration, obtained by opening lead 2 [Fig. 8.3(a)]. At zero bias, thermal noise cross correlation is found to be in good agreement with the theoretical value, $S_{12} = -4k_BT_eg_{12}$, as seen in Fig. 8.3(b)[2].

To minimize this thermal contribution to $S_{12}$, output leads are subsequently tuned to weaker tunneling than the input lead ($g_{01} \sim g_{02} \sim 4g_{12}$), for reasons discussed below. Note that as a function of $V_{\mathrm{bc}}$ and $V_0$, $S_{12}$ [Fig. 8.3(c)] looks similar to $S_1^{\mathrm{EP}}$ [Fig. 8.2(a)] in the two-lead configuration. The slightly positive $S_{12}$ ($\sim 0.2 \times 10^{-28}\mathrm{A}^2/\mathrm{Hz}$) inside the rightmost diamond is due to a small drift in the residual background of $S_{V12}$ over the 13 h of data acquisition for Fig. 3(c). Without drift, as in the shorter measurement of Fig. 8.3(b), $S_{12}$ approaches 0 at zero bias as $g_{12}$ vanishes.

Both the single-level and multi-level models can be extended to include the third lead [178, 164, 165]. Figures 8.3(d) and 8.3(e) show the single-level and multi-level simulations of $S_{12}$, respectively. Similar to the two-lead case, only the multi-level model reproduces

[2]At zero bias, the fluctuation-dissipation theorem requires $S_{12} = -2k_BT_e(g_{12} + g_{21})$, but $g_{12} = g_{21}$ at zero bias and zero magnetic field.

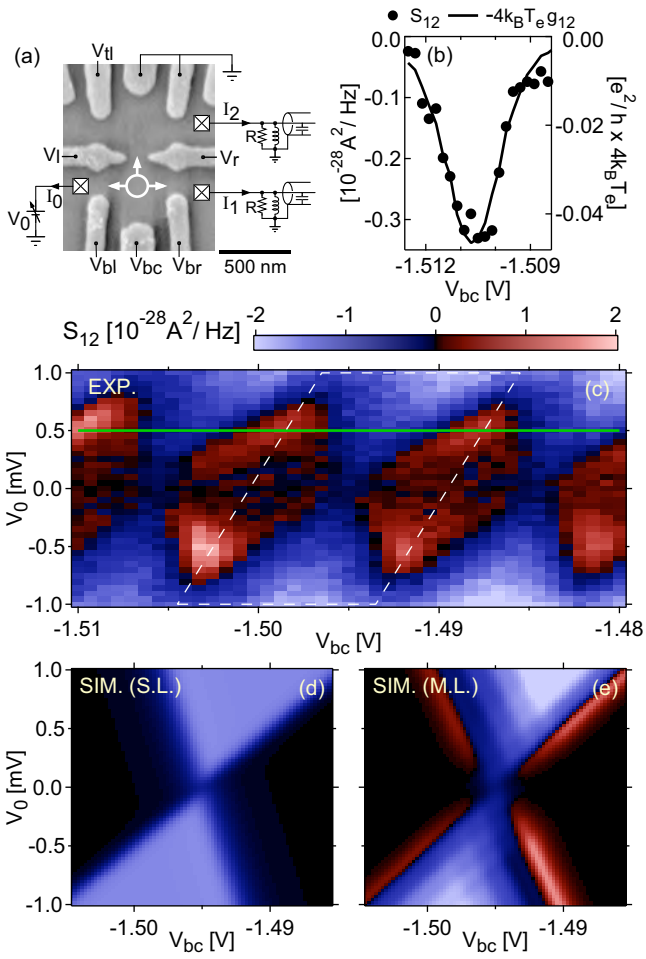


Figure 8.3: (a) The device in the three-lead configuration, in which the data for this figure and for Fig. 8.4 are taken. (b) $S_{12}$, integrated for 200 s, and $-4k_BT_eg_{12}$ over a CB peak at zero bias. Left and right axes are in different units but both apply to the data. (c) $S_{12}$ as a function of $V_0$ and $V_{\rm bc}$. Red (blue) regions indicate positive (negative) cross correlation. (d, e) Single-level (S.L.) and multi-level (M.L.) simulation of $S_{12}$, respectively, corresponding to the data region enclosed by the white dashed parallelogram in (c).

the positive cross correlation along the diamond edges.

To further investigate the relationship between noise auto- and cross correlation, we compare $S_{12}$ to the total excess Poissonian noise, $S^{\rm EP} \equiv S_1+S_2+2S_{12}-2e(I_1+I_2)\coth(eV_0/2k_BT_e)$, measured in the same three-lead configuration. Figure 8.4 shows $S^{\rm EP}$ and $S_{12}$, measured at fixed bias $V_0 = +0.5$ mV. The observed proportionality $S_{12} \sim S^{\rm EP}/4$ is reminiscent of electronic HBT-type experiments [129, 132, 71], where noise cross correlation following a beam splitter was found to be proportional to the total output current noise in excess of the

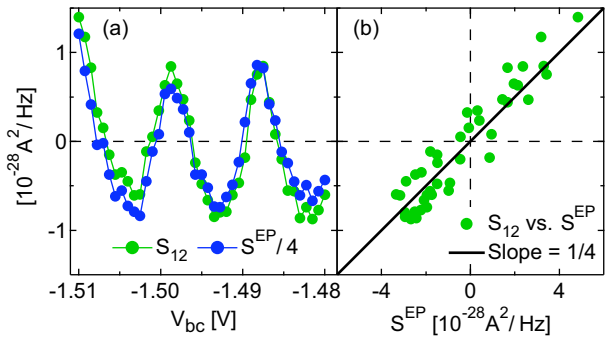


Figure 8.4: (a) $S_{12}$ (green) and $S^{\rm EP}/4$ (blue) as a function of $V_{\rm bc}$ at $V_0 = +0.5$ mV [green horizontal line in Fig. 8.3(c)]. (b) Parametric plot of $S_{12}$ (green circles) versus $S^{\rm EP}$ for the same data as in (a). The solid black line has a slope of 1/4, the value expected for a 50/50 beam splitter.

Poissonian value, with a ratio of 1/4 for a 50/50 beam splitter. In simulation, we find that this HBT-like relationship holds in the limit $g_{01} \sim g_{02} \gg g_{12}$ (recall that $g_{01} \sim g_{02} \sim 4g_{12}$ in the experiment); on the other hand, when $g_{01} \sim g_{02} \sim g_{12}$, thermal noise gives a negative contribution that lowers $S_{12}$ below $S^{\rm EP}/4$, as we have also observed experimentally (not shown). The implications are that first, with weak-tunneling output leads, the three-lead dot behaves as a two-lead dot followed by an ideal beam splitter, and second, the dynamical channel blockade that leads to super-Poissonian noise in the two-lead dot also gives rise to positive cross correlation in the three-lead dot.

## 8.6 Acknowledgements

We thank N. J. Craig for device fabrication and H.-A. Engel for valuable discussions. We acknowledge support from the NSF through the Harvard NSEC, PHYS 01-17795, DMR-05-41988, DMR-0501796. M. Yamamoto and S. Tarucha acknowledge support from the DARPA QuIST program, the Grant-in-Aid for Scientific Research A (No. 40302799), the MEXT IT Program and the Murata Science Foundation.

# Chapter 9

# Shot noise in graphene

L. DiCarlo[†], J. R. Williams[‡], Yiming Zhang[†], D. T. McClure[†], C. M. Marcus[†]
[†]*Department of Physics, Harvard University, Cambridge, Massachusetts 02138, USA*
[‡]*School of Engineering and Applied Sciences, Harvard University, Cambridge, Massachusetts 02138, USA*

We report measurements of current noise in single- and multi-layer graphene devices. In four single-layer devices, including a *p*-*n* junction, the Fano factor remains constant to within ±10% upon varying carrier type and density, and averages between 0.35 and 0.38. The Fano factor in a multi-layer device is found to decrease from a maximal value of 0.33 at the charge-neutrality point to 0.25 at high carrier density. These results are compared to theories for shot noise in ballistic and disordered graphene.[1]

[1]This chapter is adapted from Ref. [65] (submitted to Phys. Rev. Lett.).

## 9.1 Introduction

Shot noise, the temporal fluctuation of electric current out of equilibrium, originates from the partial transmission of quantized charge [39]. Mechanisms that can lead to shot noise in mesoscopic conductors include tunneling, quantum interference, and scattering from impurities and lattice defects. Shot noise yields information about transmission that is not available from the dc current alone.

In graphene [75, 76], a zero-gap two-dimensional semi-metal in which carrier type and density can be controlled by gate voltages [82], density-dependent shot-noise signatures under various conditions have been investigated theoretically [179, 180]. For wide samples of ballistic graphene (width-to-length ratio $W/L \gtrsim 4$) the Fano factor, $\mathcal{F}$, i. e., the current noise normalized to the noise of Poissonian transmission statistics, is predicted to be 1/3 at the charge-neutrality point and $\sim 0.12$ in both electron ($n$) and hole ($p$) regimes [179]. The value $\mathcal{F} = 1-1/\sqrt{2} \approx 0.29$ is predicted for shot noise across a ballistic $p$-$n$ junction [180]. For strong, smooth "charge-puddle" disorder, theory predicts $\mathcal{F} \approx 0.30$ both at and away from the charge-neutrality point, for all $W/L \gtrsim 1$ [181]. Disorder may thus have a similar effect on noise in graphene as in diffusive metals, where $\mathcal{F}$ is universally 1/3 [182, 183, 184, 43, 44, 126] regardless of shape and carrier density. Recent theory investigates numerically the evolution from a density-dependent to a density-independent $\mathcal{F}$ with increasing disorder [185]. To our knowledge, experimental data for shot noise in graphene has not yet been reported.

This chapter presents an experimental study of shot noise in graphene at low temperatures and zero magnetic field. Data for five devices, including a locally gated $p$-$n$ junction, are presented. For three globally-gated, single-layer samples, we find $\mathcal{F} \sim 0.35 - 0.37$ in both electron and hole doping regions, with essentially no dependence on electronic sheet density, $n_s$, in the range $|n_s| \lesssim 10^{12}$ cm$^{-2}$. Similar values are obtained for a locally-gated single-layer $p$-$n$ junction in both unipolar ($n$-$n$ or $p$-$p$) and bipolar ($p$-$n$ or $n$-$p$) regimes. In a multi-layer sample, the observed $\mathcal{F}$ evolves from 0.33 at the charge-neutrality point to

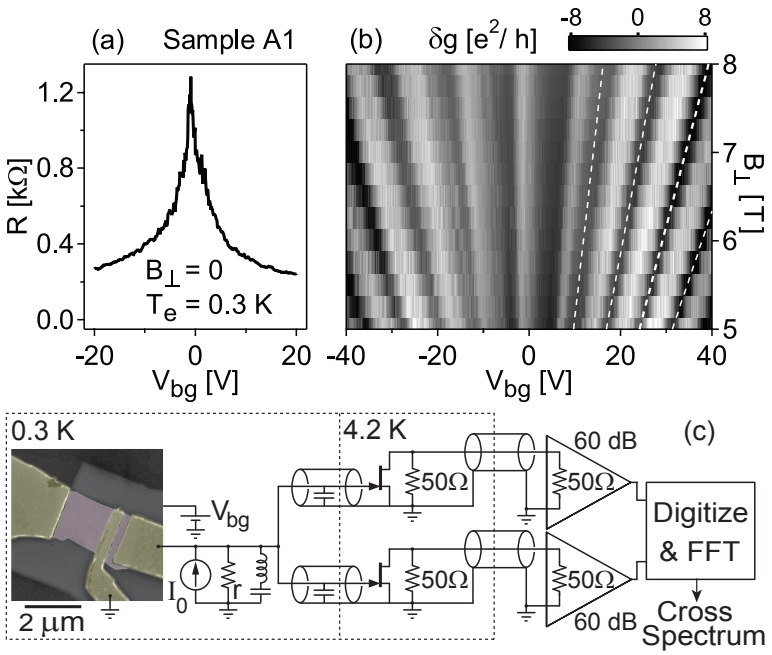


Figure 9.1: (a) Differential resistance $R$ of sample A1 as a function of back-gate voltage $V_{\rm bg}$ at electron temperature $T_e = 0.3$ K, perpendicular field $B_\perp = 0$, and source-drain voltage $V_{\rm sd} = 0$. (b) Differential two-terminal conductance $g(V_{\rm sd} = 0)$ as a function of $B_\perp$ and $V_{\rm bg}$ in the quantum Hall regime, after subtracting a quadratic fit at each $B_\perp$. Lines of constant filling factors 6, 10, 14, and 18 (dashed lines) indicate a single-layer sample. (c) Equivalent circuit near 1.5 MHz of the system measuring current noise using cross correlation of two channels [41]. Current bias $I_o$ contains a 7.5 $\mathrm{nA_{rms}}$, 20 Hz part for lock-in measurements and a controllable dc part generating the dc component of $V_{\rm sd}$ via the shunt resistance $r = 5$ kΩ. False-color scanning electron micrograph of a three-lead pattern defining two devices similar to A1 and A2. Purple indicates single-layer graphene and gold indicates metallic contacts.

0.25 at $n_{\rm s} \sim 6 \times 10^{12}$ $\mathrm{cm^{-2}}$.

## 9.2 Methods

Devices were fabricated by mechanical exfoliation of highly-oriented pyrolytic graphite [82]. Exfoliated sheets were deposited on a degenerately-doped Si substrate capped with 300 nm of thermally grown $SiO_2$. Regions identified by optical microscopy as potential single-layer graphene were contacted with thermally evaporated Ti/Au leads (5/40 nm) patterned by electron-beam lithography. Additional steps in the fabrication of the $p$-$n$ junction device are detailed in Ref. [86]. Devices were measured in two $^3$He cryostats, one allowing dc (lock-

in) transport measurements in fields $|B_\perp| \leq 8$ T perpendicular to the graphene plane, and another allowing simultaneous measurements of dc transport and noise [41] near 1.5 MHz, but limited to $B_\perp \sim 0$.

## 9.3 Shot noise in single-layer devices

Differential resistance $R = dV_{\rm sd}/dI$ ($I$ is the current, and $V_{\rm sd}$ is the source-drain voltage) of a wide, short sample [A1, $(W, L) = (2.0, 0.35)$ $\mu$m] is shown as a function of back-gate voltage $V_{\rm bg}$ at $V_{\rm sd} = 0$ and $B_\perp = 0$ in Fig. 9.1(a). While the width of the peak is consistent with A1 being single-layer graphene [77, 78], more direct evidence is obtained from the QH signature shown in Fig. 9.1(b). The grayscale image shows differential conductance $g = 1/R$ as a function of $V_{\rm bg}$ and $B_\perp$, following subtraction of the best-fit quadratic polynomial to $g(V_{\rm bg})$ at each $B_\perp$ setting to maximize contrast. Dashed lines correspond to filling factors $n_{\rm s}h/eB_\perp = 6$, 10, 14, and 18, with $n_{\rm s} = \alpha(V_{\rm bg}+1.1\ {\rm V})$ and lever arm $\alpha = 6.7\times10^{10}$ cm$^{-2}$/V. Their alignment with local minima in $\delta g(V_{\rm bg})$ identifies A1 as single-layer graphene [186, 83]. The Drude mean free path $\ell = h/2e^2\cdot\sigma/k_{\rm F}$ [187], where $k_{\rm F} = \sqrt{\pi|n_{\rm s}|}$, is found to be $\sim 40$ nm away from the charge-neutrality point using the $B_\perp = 0$ conductivity $\sigma = (RW/L)^{-1}$ [Fig. 9.2(a) inset].

Current noise spectral density $S_I$ is measured using a cross-correlation technique described in Ref. [41] [see Fig. 9.1(c)]. Following calibration of amplifier gains and electron temperature $T_e$ using Johnson noise thermometry (JNT) for each cooldown, the excess noise $S_I^{\rm e} \equiv S_I - 4k_BT_eg(V_{\rm sd})$ is extracted. $S_I^{\rm e}(V_{\rm sd})$ for sample A1 is shown in Fig. 9.2(a). Linearity of $S_I^{\rm e}$ at high bias indicates negligible extrinsic ($1/f$ or telegraph) resistance fluctuations within the measurement bandwidth. For these data, a single-parameter fit to the scattering-theory form (for energy-independent transmission) [140, 53],

$$S_I^{\rm e} = 2eI\mathcal{F}\left[\coth\left(\frac{eV_{\rm sd}}{2k_BT_e}\right) - \frac{2k_BT_e}{eV_{\rm sd}}\right], \tag{9.1}$$

gives a best-fit Fano factor $\mathcal{F} = 0.349$. Simultaneously measured conductance $g \approx 22.2\ e^2/h$

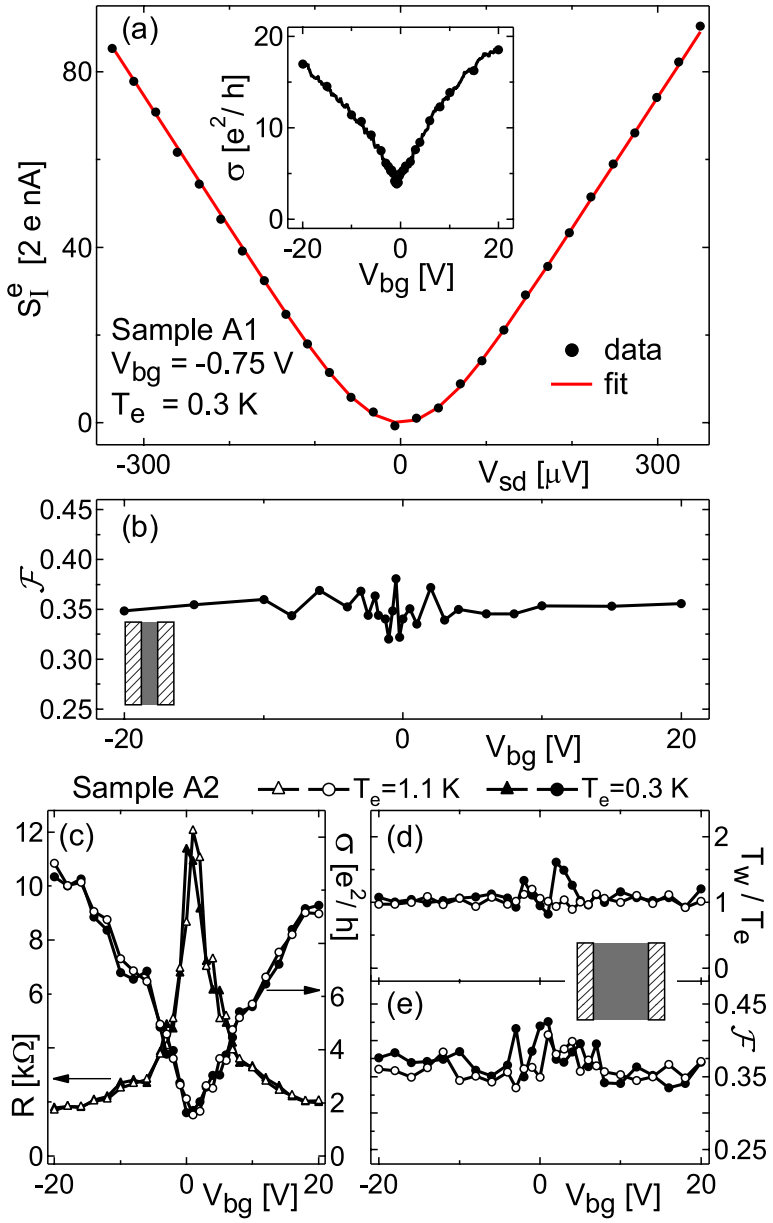


Figure 9.2: (a) Inset: Conductivity $\sigma = (RW/L)^{-1}$ calculated using $R(V_{\rm bg})$ data in Fig. 9.1(a) and $W/L = 5.7$. Solid black circles correspond to $\sigma(V_{\rm sd} = 0)$ at the $V_{\rm bg}$ settings of noise measurements shown in (b). Main: Excess noise $S_I^{\rm e}$ as function of $V_{\rm sd}$ near the charge-neutrality point, $V_{\rm bg} = -0.75$ V. The solid red curve is the single-parameter best fit to Eq. (9.1), giving Fano factor $\mathcal{F} = 0.349$ (using $T_e = 303$ mK as calibrated by JNT). (b) Best-fit $\mathcal{F}$ at 25 $V_{\rm bg}$ settings across the charge-neutrality point for electron and hole densities reaching $|n_{\rm s}| \sim 1.4 \times 10^{12}$ cm$^{-2}$. (c) $R$ (left axis) and $\sigma$ (right axis) of sample A2 as a function of $V_{\rm bg}$ ($W/L = 1.4$), with $V_{\rm sd} = 0$, at 0.3 K (solid markers) and at 1.1 K (open markers). (d), (e) Crossover width $T_{\rm w}$ (normalized to JNT-calibrated $T_e$) and $\mathcal{F}$, obtained from best-fits using Eq. (9.1) to $S_I^{\rm e}(V_{\rm sd})$ data over $|V_{\rm sd}| \leq 350(650)$ $\mu$V for $T_e = 0.3(1.1)$ K.

was independent of bias within $\pm 0.5\%$ (not shown) in the $|V_{\rm sd}| \leq 350$ $\mu$V range used for the fit. Note that the observed quadratic-to-linear crossover agrees well with that in the curve fit, indicating weak inelastic scattering in A1 [43, 44], and negligible series resistance (e. g., from contacts), which would broaden the crossover by reducing the effective $V_{\rm sd}$ across the sample.

Figure 9.2(b) shows similarly measured values for $\mathcal{F}$ as a function of $V_{\rm bg}$. $\mathcal{F}$ is observed to remain nearly constant for $|n_{\rm s}| \lesssim 10^{12}$ cm$^{-2}$. Over this density range, the average $\mathcal{F}$ is 0.35 with standard deviation 0.01. The estimated error in the best-fit $\mathcal{F}$ at each $V_{\rm bg}$ setting is $\pm 0.002$, comparable to the marker size and smaller than the variation in $\mathcal{F}$ near $V_{\rm bg} = 0$, which we believe results from mesoscopic fluctuations of $\mathcal{F}$. Nearly identical noise results (not shown) were found for a similar sample (B), with dimensions $(2.0, 0.3)$ $\mu$m and a QH signature consistent with a single layer.

Transport and noise data for a more square single-layer sample [A2, patterned on the same graphene sheet as A1, with dimensions $(1.8, 1.3)$ $\mu$m] at $T_e = 0.3$ K (solid circles) and $T_e = 1.1$ K (open circles) are shown in Figs. 9.2(c-e). At both temperatures, the conductivity shows $\sigma_{\rm min} \approx 1.5$ $e^2/h$ and gives $\ell \sim 25$ nm away from the charge-neutrality point. That these two values differ from those in sample A1 is particularly notable as samples A1 and A2 were patterned on the same piece of graphene. Results of fitting Eq. (9.1) to $S_I^{\rm e}(V_{\rm sd})$ for sample A2 are shown in Figs. 9.2(d) and 9.2(e). To allow for possible broadening of the quadratic-to-linear crossover by series resistance and/or inelastic scattering, we treat electron temperature as a second fit parameter (along with $\mathcal{F}$) and compare the best-fit value, $T_{\rm w}$, with the $T_e$ obtained from Johnson noise. Figure 9.2(d) shows $T_{\rm w}$ tracking the calibrated $T_e$ at both temperatures. Small deviations of $T_{\rm w}/T_e$ from unity near the charge-neutrality point at $T_e = 0.3$ K can be attributed to conductance variations up to $\pm 20\%$ in the fit range $|V_{\rm sd}| \leq 350$ $\mu$V at these values of $V_{\rm bg}$. As in sample A1, $\mathcal{F}$ is found to be independent of carrier type and density over $|n_{\rm s}| \lesssim 10^{12}$ cm$^{-2}$, averaging 0.37(0.36) with standard deviation 0.02(0.02) at $T_e = 0.3(1.1)$ K. Evidently, despite its different aspect

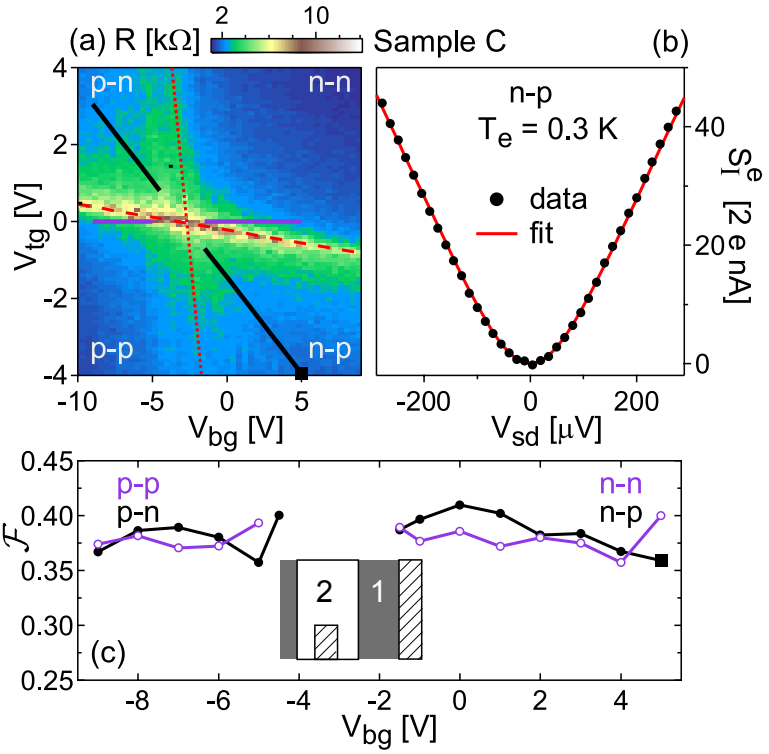


Figure 9.3: (a) Differential resistance $R$ of sample C, a single-layer $p$-$n$ junction, as a function of back-gate voltage $V_{\rm bg}$ and top-gate voltage $V_{\rm tg}$. The skewed-cross pattern defines quadrants of $n$ and $p$ carriers in regions 1 and 2. Red lines indicate charge-neutrality lines in region 1 (dotted) and region 2 (dashed). (b) $S_I^{\rm e}(V_{\rm sd})$ measured in $n$-$p$ regime with $(V_{\rm bg}, V_{\rm tg}) = (5, -4)$ V (solid dots) and best fit to Eq. (9.1) (red curve), with $\mathcal{F} = 0.36$. (c) Main: Best-fit $\mathcal{F}$ along the cuts shown in (a), at which $n_{s1} \sim n_{s2}$ (purple) and $n_{s1} \sim -4\, n_{s2}$ (black). Inset: Schematic of the device. The top gate covers region 2 and one of the contacts.

ratio, A2 exhibits a noise signature similar to that of A1.

## 9.4 Shot noise in a *p*-*n* junction

Transport and noise measurements for a single-layer graphene $p$-$n$ junction [86], sample C, are shown in Fig. 9.3. The color image in Fig. 9.3(a) shows differential resistance $R$ as a function of $V_{\rm bg}$ and local top-gate voltage $V_{\rm tg}$. The two gates allow independent control of charge densities in adjacent regions of the device [see Fig. 9.3(c) inset]. In the bipolar regime, the best-fit $\mathcal{F}$ shows little density dependence and averages 0.38, equal to the average value deep in the unipolar regime, and similar to results for the back-gate-only single-layer

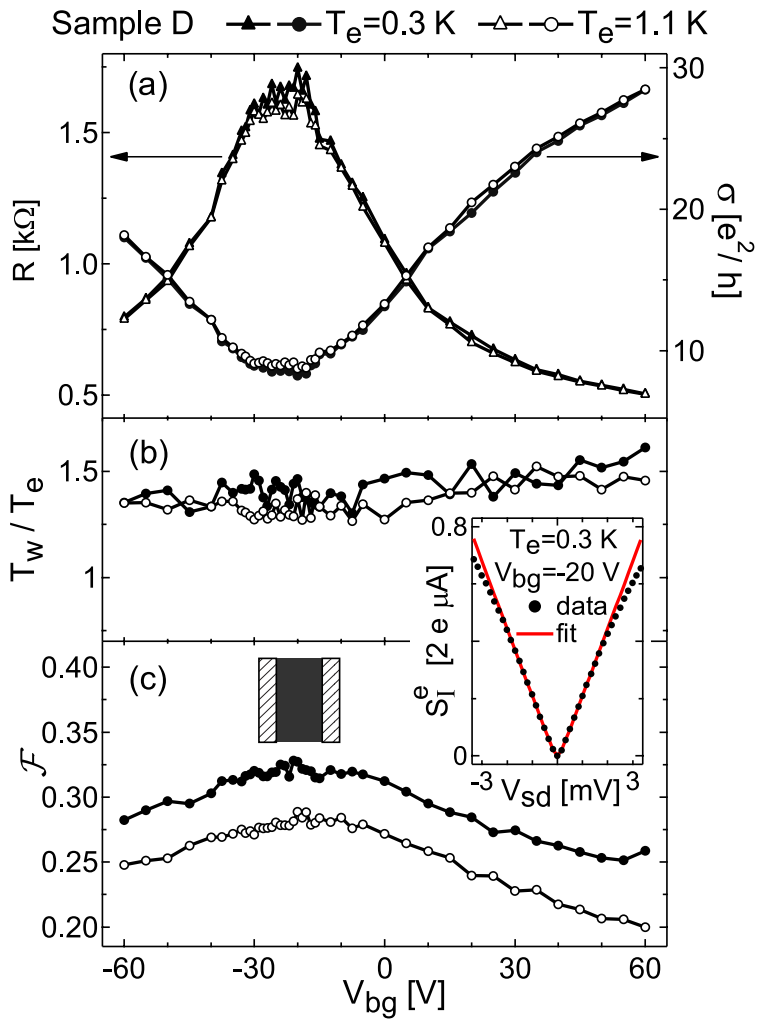


Figure 9.4: (a) Differential resistance $R$ (left axis) and conductivity $\sigma$ (right axis) of sample D as a function of $V_{\rm bg}$, with $V_{\rm sd} = 0$, at 0.3 K (solid markers) and at 1.1 K (open markers). (b),(c) Best-fit $T_{\rm w}$ (normalized to JNT-calibrated $T_e$) and $\mathcal{F}$ to $S_I^{\rm e}(V_{\rm sd})$ data over $|V_{\rm sd}| \leq 0.5(1)$ mV for $T_e = 0.3(1.1)$ K. Inset: Sublinear dependence of $S_I^{\rm e}$ on $V_{\rm sd}$ is evident in data taken over a larger bias range. Solid red curve is the two-parameter best fit of Eq. (9.1) over $|V_{\rm sd}| \leq 0.5$ mV.

samples (A1, A2 and B). Close to charge neutrality in either region (though particularly in the region under the top gate), $S_I^{\rm e}(V_{\rm sd})$ deviates from the form of Eq. (9.1) (data not shown). This is presumably due to resistance fluctuation near charge neutrality, probably due mostly to mobile traps in the $Al_2O_3$ insulator beneath the top gate.

## 9.5 Shot noise in a multi-layer device

Measurements at 0.3 K and at 1.1 K for sample D, of dimensions $(1.8, 1.0)$ $\mu$m, are shown in Fig. 9.4. A $\sim$ 3 nm step height between $SiO_2$ and carbon surfaces measured by atomic force microscopy prior to electron-beam lithography [188] suggests this device is likely multi-layer. Further indications include the broad $R(V_{\rm bg})$ peak [189] and the large minimum conductivity, $\sigma_{\rm min} \sim 8\ e^2/h$ at $B_\perp = 0$ [Fig. 9.4(a)], as well as the absence of QH signature for $|B_\perp| \leq 8$ T at 250 mK (not shown). Two-parameter fits of $S_I^{\rm e}(V_{\rm sd})$ data to Eq. (9.1) show three notable differences from results in the single-layer samples [Figs. 9.4(b) and 9.4(c)]: First, $\mathcal{F}$ shows a measurable dependence on back-gate voltage, decreasing from 0.33 at the charge-neutrality point to 0.25 at $n_{\rm s} \sim 6 \times 10^{12}$ cm$^{-2}$ for $T_e = 0.3$ K; Second, $\mathcal{F}$ decreases with increasing temperature; Finally, $T_{\rm w}/T_e$ is 1.3-1.6 instead of very close to 1. We interpret the last two differences, as well as the sublinear dependence of $S_I^{\rm e}$ on $V_{\rm sd}$ (see Fig. 9.4 inset) as indicating sizable inelastic scattering [182, 183] in sample D. (An alternative explanation in terms of series resistance would require it to be density, bias, and temperature dependent, which is inconsistent with the independence of $g$ on $V_{\rm sd}$ and $T_e$).

## 9.6 Summary and acknowledgements

Summarizing the experimental results, we find that in four single-layer samples, $\mathcal{F}$ is insensitive to carrier type and density, temperature, aspect ratio, and the presence of a $p$-$n$ junction. In one multi-layer sample, $\mathcal{F}$ does depend on density and temperature, and $S_I^{\rm e}(V_{\rm sd})$ shows a broadened quadratic-to-linear crossover and is sublinear in $V_{\rm sd}$ at high bias. We may now compare these results to expectations based on theoretical and numerical results for ballistic and disordered graphene.

Theory for ballistic single-layer graphene with $W/L \gtrsim 4$ gives a universal $\mathcal{F} = 1/3$ at the charge-neutrality point, where transmission is evanescent, and $\mathcal{F} \sim 0.12$ for $|n_{\rm s}| \gtrsim \pi/L^2$, where propagating modes dominate transmission [179]. While the measured $\mathcal{F}$ at the charge-

neutrality point in samples A1 and B ($W/L = 5.7$ and 6.7, respectively) is consistent with this prediction, the absence of density dependence is not: $\pi/L^2 \sim 3\times10^9$ cm$^{-2}$ is well within the range of carrier densities covered in the measurements. Theory for ballistic graphene $p$-$n$ junctions [180] predicts $\mathcal{F} \approx 0.29$, lower than the value $\sim 0.38$ observed in sample C in both $p$-$n$ and $n$-$p$ regimes. We speculate that these discrepancies likely arise from the presence of disorder. Numerical results for strong, smooth disorder [181] predict a constant $\mathcal{F}$ at and away from the charge-neutrality point for $W/L \gtrsim 1$, consistent with experiment. However, the predicted value $\mathcal{F} \approx 0.30$ is $\sim 20\%$ lower than observed in all single-layer devices. Recent numerical simulations [185] of small samples ($L = W \sim 10$ nm) investigate the vanishing of carrier dependence in $\mathcal{F}$ with increasing disorder strength. In the regime where disorder makes $\mathcal{F}$ density-independent, the value $\mathcal{F} \sim 0.35 - 0.40$ is found to depend weakly on disorder strength and sample size.

Since theory for an arbitrary number of layers is not available for comparison to noise results in the multi-layer sample D, we compare only to existing theory for ballistic bi-layer graphene [190]. It predicts $\mathcal{F} = 1/3$ over a much narrower density range than for the single layer, and abrupt features in $\mathcal{F}$ at finite density due to transmission resonances. A noise theory beyond the bi-layer ballistic regime may thus be necessary to explain the observed smooth decrease of $\mathcal{F}$ with increasing density in sample D.

We thank C. H. Lewenkopf, L. S. Levitov, and D. A. Abanin for useful discussions. Research supported in part by the IBM Ph.D. Fellowship program (L.D.C.), INDEX, an NRI Center, and Harvard NSEC.

# Chapter 10

# Quantum Hall effect in a gate-controlled $p$-$n$ junction in graphene

J. R. Williams
*School of Engineering and Applied Sciences, Harvard University, Cambridge, Massachusetts 02138*
L. DiCarlo, C. M. Marcus
*Department of Physics, Harvard University, Cambridge, Massachusetts 02138*

The unique band structure of graphene allows reconfigurable electric-field control of carrier type and density, making graphene an ideal candidate for bipolar nanoelectronics. We report the realization of a single-layer graphene $p$-$n$ junction in which carrier type and density in two adjacent regions are locally controlled by electrostatic gating. Transport measurements in the quantum Hall regime reveal new plateaus of two-terminal conductance across the junction at 1 and 3/2 times the quantum of conductance, $e^2/h$, consistent with recent theory. Beyond enabling investigations in condensed matter physics, the local-gating technique demonstrated here sets the foundation for a future graphene-based bipolar technology.[1]

---

[1]This chapter is adapted with permission from Science **317**, 638 (2007). © (2007) by the American Association for the Advancement of Science.

## 10.1 Introduction

Graphene, a single-layer hexagonal lattice of carbon atoms, has recently emerged as a fascinating system for fundamental studies in condensed matter physics [75], as well as a candidate for novel sensors [191, 192] and post-silicon electronics [81, 193, 194, 195, 84, 85, 82]. The unusual band structure of single-layer graphene makes it a zero-gap semiconductor with a linear (photon-like) energy-momentum relation near the points where valence and conduction bands meet. Carrier type—electron-like or hole-like—and density can be controlled using the electric-field effect [82], obviating conventional semiconductor doping, for instance via ion implantation. This feature, doping via local gates, would allow graphene-based bipolar technology—devices comprising junctions between hole-like and electron-like regions, or $p$-$n$ junctions—to be reconfigurable, using only gate voltages to distinguish $p$ (hole-like) and $n$ (electron-like) regions within a single sheet. While global control of carrier type and density in graphene using a single back gate has been investigated by several groups [77, 78, 196], local control [84, 85] of single-layer graphene has remained an important technological milestone. In addition, $p$-$n$ junctions are of great interest for low-dimensional condensed matter physics. For instance, recent theory predicts that a local step in potential would allow solid-state realizations of relativistic ("Klein") tunneling [197, 180], and a surprising scattering effect known as Veselago lensing [198], comparable to scattering of electromagnetic waves in negative-index materials [199].

We report the realization of local top gating in a single-layer graphene device which, combined with global back gating, allows individual control of carrier type and density in adjacent regions of a single atomic layer. Transport measurements at zero perpendicular magnetic field $B_\perp$ and in the quantum Hall (QH) regime demonstrate that the functionalized aluminum oxide ($Al_2O_3$) separating the graphene from the top gate does not significantly dope the layer nor affect its low-frequency transport properties. We study the QH signature of the graphene $p$-$n$ junction, finding new conductance plateaus at 1 and 3/2 $e^2/h$, consistent

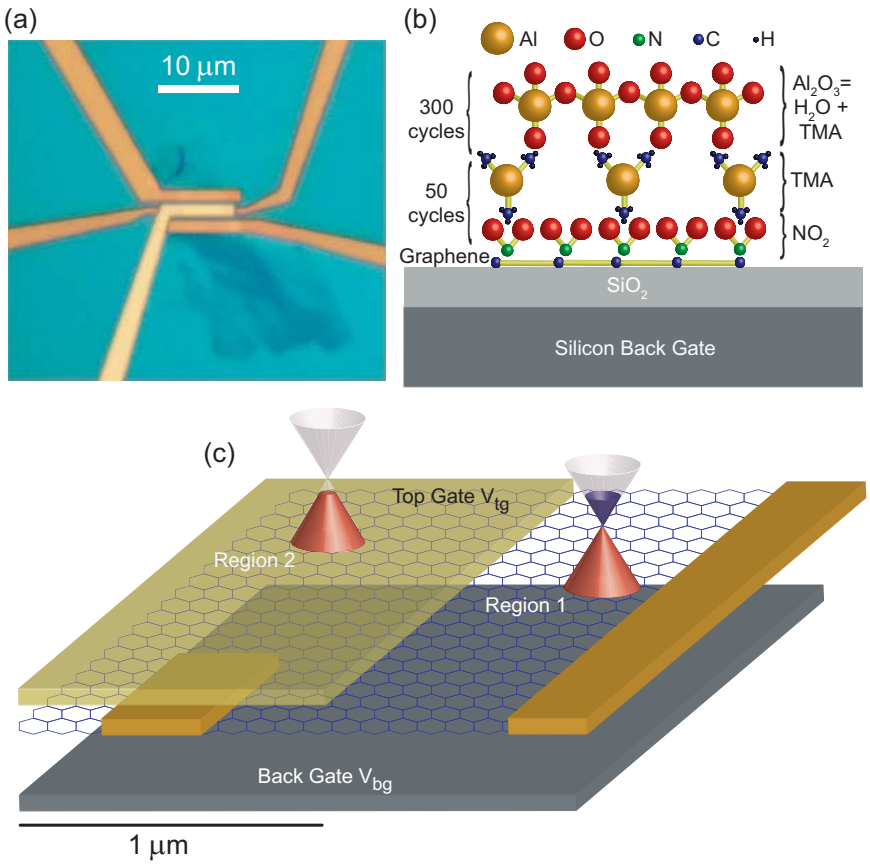


Figure 10.1: (a) Optical micrograph of a device similar to the one measured. Metallic contacts and top gate appear in orange and yellow, respectively. Darker regions below the contacts are thicker graphite from which the contacted single layer of graphene extends. (b) Illustration of the oxide deposition process. A non-covalent functionalization layer is first deposited using $NO_2$ and TMA (50 cycles) and $Al_2O_3$ is then grown by atomic layer deposition using $H_2O$-TMA (305 cycles yielding $\sim 30$ nm thickness). (c) Schematic diagram of the device measured in this experiment.

with recent theory addressing equilibration of edge states at the $p$-$n$ interface [200].

## 10.2 Device fabrication

Graphene sheets are prepared via mechanical exfoliation using a method similar to that used in Ref. [82]. Graphite flakes are deposited on 300 nm of $SiO_2$ on a degenerately doped Si substrate. Inspection with an optical microscope allows potential single-layer regions of graphene to be identified by a characteristic coloration that arises from thin-film interference. These micron-scale regions are contacted with thermally evaporated Ti/Au

(5/40 nm), and patterned using electron-beam lithography. Next, a $\sim 30$ nm layer of oxide is deposited atop the entire substrate. As illustrated [Fig. 10.1(b)], the oxide consists of two parts: a non-convalent functionalization layer (NCFL) and $Al_2O_3$. This deposition technique is based on a recipe successfully applied to carbon nanotubes [201]. The NCFL serves two purposes. One is to create a non-interacting layer between the graphene and the $Al_2O_3$ and the other is to obtain a layer that is catalytically suitable for the formation of $Al_2O_3$ by atomic layer deposition (ALD). The NCFL is synthesized by 50 pulsed cycles of $NO_2$ and trimethylaluminum (TMA) at room temperature inside an ALD reactor. Next, 5 cycles of $H_2O$-TMA are applied at room temperature to prevent desorption of the NCFL. Finally, $Al_2O_3$ is grown at 225°C with 300 $H_2O$-TMA ALD cycles. To complete the device, a second step of electron-beam lithography defines a local top gate (5/40 nm Ti/Au) covering a region of the device that includes one of the metallic contacts.

## 10.3 Measurement setup

A completed device, similar in design to that shown in the optical image in Fig. 10.1(a), was cooled in a $^3$He refrigerator and characterized at temperatures $T$ of 250 mK and 4.2 K. Differential resistance $R = dV/dI$, where $I$ is the current and $V$ the source-drain voltage, was measured by standard lock-in techniques with a current bias of 1 (10) $nA_{rms}$ at 95 Hz for $T = 250$ mK (4.2 K). The voltage across two contacts on the device, one outside the top-gate region and one underneath the top gate, was measured in a four-wire configuration, eliminating series resistance of the cryostat lines. A schematic of the device is shown in Fig. 10.1(c).

## 10.4 Transport at zero magnetic field

The differential resistance $R$ as a function of back-gate voltage $V_{bg}$ and top-gate voltage $V_{tg}$ at $B_\perp = 0$ [Fig. 10.2(a)], demonstrates independent control of carrier type and density

in the two regions. This two-dimensional (2D) plot reveals a skewed, cross-like pattern that separates the space of top-gate and back-gate voltages into four quadrants of well-defined carrier type in the two regions of the sample. The horizontal (diagonal) ridge corresponds to charge neutrality, i.e., the Dirac point, in region 1 (2). The slope of the charge-neutral line in region 2, along with the known distances to the top gate and back gate, gives a dielectric constant $\kappa \sim 6$ for the functionalized $Al_2O_3$. The center of the cross at $(V_{tg}, V_{bg}) \sim (-0.2\ \text{V}, -2.5\ \text{V})$ corresponds to charge neutrality across the entire graphene sample. Its proximity to the origin of gate voltages demonstrates that the functionalized oxide does not chemically dope the graphene significantly.

Slices through the 2D conductance plot at fixed $V_{tg}$ are shown in Fig. 10.2(c). The slice at $V_{tg} = 0$ shows a single peak commonly observed in devices with only a global back gate [82, 77, 78, 196]. Using a Drude model away from the charge-neutrality region, mobility is estimated at $\sim 7000\ \text{cm}^2/\text{Vs}$ [82]. The peak width, height, and back-gate position are consistent with single-layer graphene [77, 78, 196] and provides evidence that the electronic structure and degree of disorder of the graphene is not strongly affected by the oxide. Slices at finite $|V_{tg}|$ reveal a doubly-peaked structure. The weaker peak, which remains near $V_{bg} \sim -2.5$ V at all $V_{tg}$, corresponds to the Dirac point of region 1. The stronger peak, which moves linearly with $V_{tg}$, is the Dirac point for region 2. The difference in peak heights is a consequence of the different aspect ratios of regions 1 and 2. Horizontal slices at fixed $V_{bg}$ corresponding to the horizontal lines in Fig. 10.2(a) are shown in Fig. 10.2(b). These slices show a single peak corresponding to the Dirac point of region 2. This peak becomes asymmetric away from the charge-neutrality point in region 1. We note that the $V_{bg}$ dependence of the asymmetry is opposite to that observed in Ref. [85], where the asymmetry is studied in greater detail. The changing background resistance results from the different density in region 1 at each $V_{bg}$ setting. Current-voltage ($I$-$V$) characteristics, measured throughout the $(V_{tg}, V_{bg})$ plane, show no sign of rectification in any of the four quadrants or at either of the charge-neutral boundaries between quadrants [Fig. 10.2(d)],

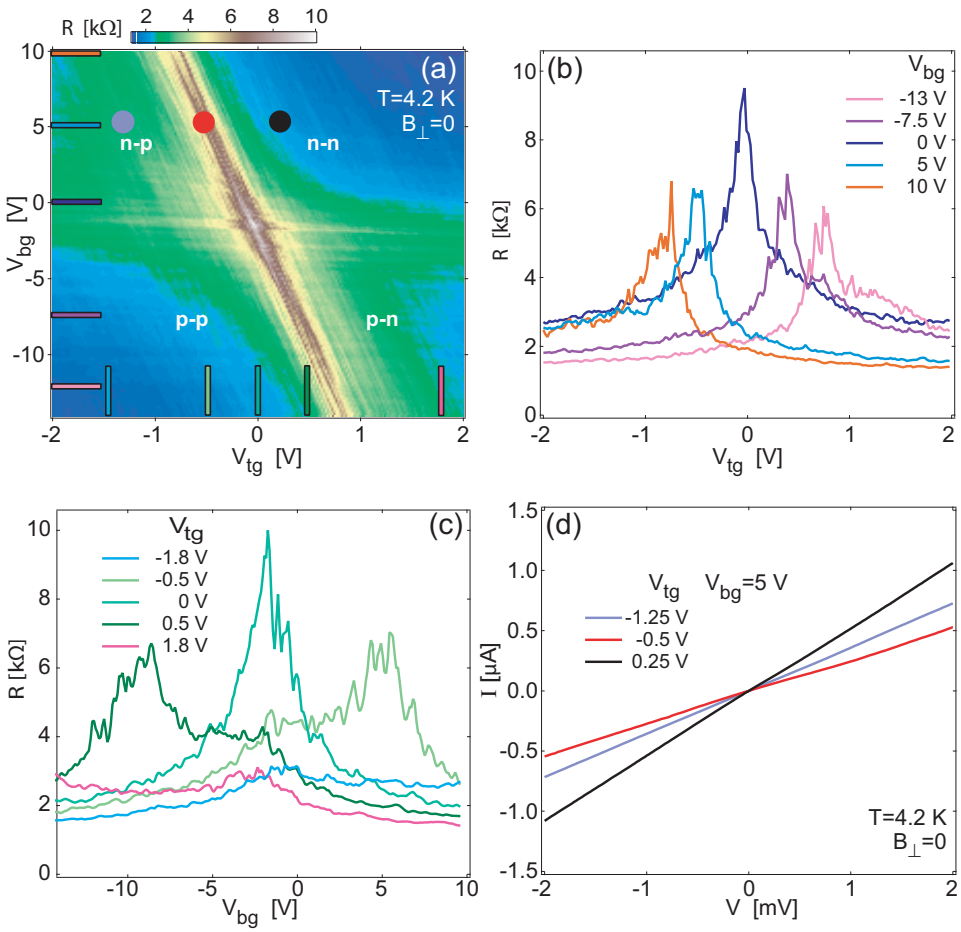


Figure 10.2: (a) Two-terminal differential resistance $R$ as a function of the top-gate voltage $V_{\rm tg}$ and back-gate voltage $V_{\rm bg}$ at $B_\perp = 0$ and $T = 4.2$ K, demonstrating independent control of carrier type and density in regions 1 and 2. Labels in each of the four quadrants indicate the carrier type (first letter indicates carrier type in region 1). (b and c) Horizontal (Vertical) slices at $V_{\rm bg}$ ($V_{\rm tg}$) settings corresponding to the colored lines superimposed on Fig. 10.2(a). (d) $I$-$V$ curves at the gate voltage settings corresponding to the solid circles in Fig. 10.2(a) are representative of the linear characteristics observed everywhere in the plane of gate voltages.

as expected for reflectionless ("Klein") tunneling at the $p$-$n$ interface [197, 180].

## 10.5 Transport in the quantum Hall regime

At large $B_\perp$, the Dirac-like energy spectrum of graphene gives rise to a characteristic series of QH plateaus in conductance, reflecting the presence of a zero-energy Landau level, that includes only odd multiples of 2 $e^2/h$ (that is, 2, 6, 10,... $\times e^2/h$) for uniform carrier density

in the sheet [202, 203, 204]. These plateaus can be understood in terms of an odd number of QH edge states (including a zero-energy edge state) at the edge of the sheet, circulating in a direction determined by the direction of $B_\perp$ and the carrier type. The situation is somewhat more complicated when varying local density and carrier type across the sample.

A 2D color plot of differential conductance $g = 1/R$ as a function of $V_{\rm bg}$ and $V_{\rm tg}$ at $B_\perp = 4$ T is shown in Fig. 10.3(a). A vertical slice at $V_{\rm tg} = 0$ through the *p*-*p* and *n*-*n* quadrants [Fig. 10.3(b)] reveals conductance plateaus at 2, 6, and 10 $e^2/h$ in both quadrants, demonstrating that the sample is single-layer and that the oxide does not significantly distort the Dirac spectrum.

QH features are investigated for differing filling factors $\nu_1$ and $\nu_2$ in regions 1 and 2 of the graphene sheet. A horizontal slice through Fig. 10.3(a) at filling factor $\nu_1 = 6$ is shown in Fig. 10.3(c). Starting from the *n*-*n* quadrant, plateaus are observed at 6 $e^2/h$ and 2 $e^2/h$ at top-gate voltages corresponding to filling factors $\nu_2 = 6$ and 2, respectively. Crossing over to the *n*-*p* quadrant by further decreasing $V_{\rm tg}$, a new plateau at 3/2 $e^2/h$ appears for $\nu_2 = -2$. In the $\nu_2 = -6$ region, no clear QH plateau is observed. Another horizontal slice at $\nu_1 = 2$ shows 2 $e^2/h$ plateaus at both $\nu_2 = 6$ and 2 [see Fig. 10.3(d)]. Crossing into the *n*-*p* quadrant, the conductance exhibits QH plateaus at 1 $e^2/h$ for $\nu_2 = -2$ and near 3/2 $e^2/h$ for $\nu_2 = -6$.

For $\nu_1$ and $\nu_2$ of the same sign (*n*-*n* or *p*-*p*), the observed conductance plateaus follow

$$g = \min(|\nu_1|, |\nu_2|) \times e^2/h. \tag{10.1}$$

This relation suggests that the edge states common to both regions propagate from source to drain while the remaining $|\nu_1 - \nu_2|$ edge states in the region of highest absolute filling factor circulate internally within that region and do not contribute to the conductance. This picture is consistent with known results on conventional 2D electron gas systems with inhomogeneous electron density [205, 206, 207].

Recent theory [200] addresses QH transport for filling factors with opposite sign in

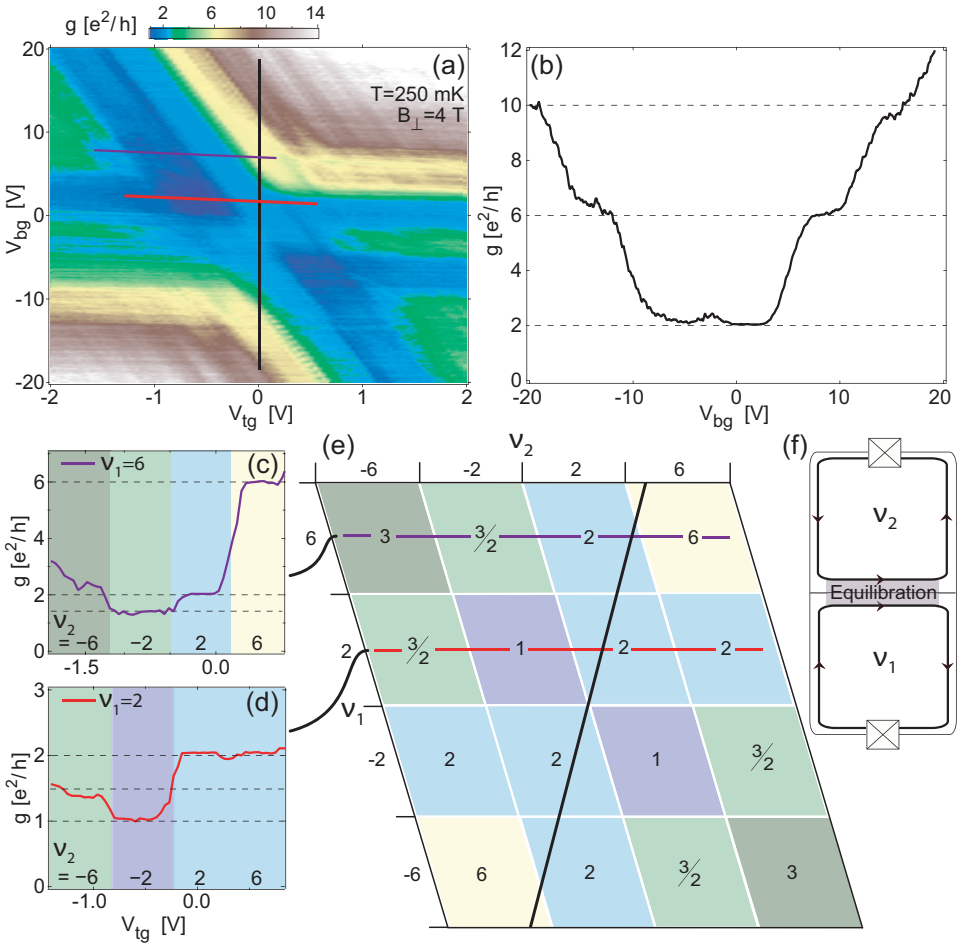


Figure 10.3: (a) Differential conductance $g$ as a function of $V_{\rm tg}$ and $V_{\rm bg}$ at $B_\perp = 4$ T and $T = 250$ mK. (b) Vertical slice at $V_{\rm tg} = 0$, traversing $p$-$p$ and $n$-$n$ quadrants. Plateaus are observed at 2 $e^2/h$ and 6 $e^2/h$, the quantum Hall signature of single-layer graphene. (c) Horizontal slice at $\nu_1 = 6$ showing conductance plateaus at 6, 2 and 3/2 $e^2/h$. (d) Horizontal slice at $\nu_2$ showing QH plateaus at 2, 1 and 3/2 $e^2/h$. (e) Table of conductance plateau values as a function of filling factors calculated using Eqs. (10.1) and (10.2). Black, purple and red lines correspond to slices in (b), (c) and (d), respectively. (f) Schematic of counter-circulating edge states at filling factors $\nu_1 = -\nu_2 = 2$.

regions 1 and 2 ($n$-$p$ and $p$-$n$). In this case, counter-circulating edge states in the two regions travel in the same direction along the $p$-$n$ interface [Fig. 10.3(f)], which presumably facilitates mode mixing between parallel-traveling edge states. For the case of complete mode-mixing—that is, when current entering the junction region becomes uniformly distributed among the $|\nu_1| + |\nu_2|$ parallel-traveling modes—quantized plateaus are expected

[200] at values

$$g = \frac{|\nu_1||\nu_2|}{|\nu_1| + |\nu_2|} \times e^2/h. \tag{10.2}$$

A table of the conductance plateau values given by Eqs. (10.1) and (10.2) is shown in Fig. 10.3(e). Plateau values at 1 $e^2/h$ for $\nu_1 = -\nu_2 = 2$ and at 3/2 $e^2/h$ for $\nu_1 = 6$ and $\nu_2 = -2$ are observed in experiment. Notably, the 3/2 $e^2/h$ plateau suggests uniform mixing among four edge stages (three from region 1 and one from region 2). All observed conductance plateaus are also seen at $T = 4$ K and for $B_\perp$ in the range 4 to 8 T.

We do find some departures between the experimental data and Eqs. (10.1) and (10.2), as represented in the grid of Fig. 10.3(e). For instance, the plateau near 3/2 $e^2/h$ in Fig. 10.3(d) is seen at a value of $\sim$ 1.4 $e^2/h$ and no clear plateau at 3 $e^2/h$ is observed for $\nu_1 = -\nu_2 = 6$. We speculate that the conductance in these regions being lower than their expected values is an indication of incomplete mode mixing. We also observe an unexpected peak in conductance at a region in gate voltage between the two 1 $e^2/h$ plateaus at $\nu_1 = \pm\nu_2 = 2$. This rise in conductance is clearly seen for $|V_{\rm tg}|$ values between $\sim$ 1 and 2 V and $V_{\rm bg}$ values between $\sim$ -5 and -2 V. This may result from the possible existence of puddles of electrons and holes near the charge-neutrality points of regions 1 and 2, as previously suggested [208].

## 10.6 Acknowledgements

We thank L. S. Levitov, D. A. Abanin, C. H. Lewenkopf, and P. Jarillo-Herrero for useful discussions. We thank Z. Chen at IBM T. J. Watson Research Center for suggesting the $NO_2$ functionalization process and D. Monsma for assistance in implementing it. Research supported in part by INDEX, an NRI Center, and by the Harvard NSEC.

# Appendix A

# High-frequency wiring

## A.1 Coaxial lines for dilution refrigerator

High-frequency excitations, be them continuous-wave (CW) at frequencies $f \gtrsim 1$ MHz or pulses with rise times $\tau_{\mathrm{r}} \lesssim 1$ $\mu$s, are coupled from room temperature to a sample at the coldfinger of a dilution refrigerator using coaxial lines. Aspects to consider when designing a coaxial line include

- frequency range of interest (pass band),
- signal amplitude needed,
- thermal loads at the sample, which affect electron temperature,
- thermal loads at each cryostat stage (1 K pot, still, mixing chamber), which can affect cryostat performance and thus also the electron temperature,
- coupling of thermal radiation from the various cryostat stages to the sample.

A very useful discussion on coaxial lines for the dilution refrigerator can be found in Ap. B of Alex Johnson's thesis [74]. Specifically, Alex describes the design for a coaxial line that is mainly used for pulsed-gating of single and double GaAs quantum dots. That design is based on a line that Heather Lynch, Lily Childress and I assembled when attempting Rabi oscillations of charge in tunnel-coupled double quantum dots during 2002-03. The purpose

of this appendix is to complement the information on high-frequency wiring already given by Alex.

### A.1.1 An early approach

The coaxial line used in the photocurrent/rectification experiment presented in Ch. 3 is shown in Fig. A.1. This configuration is essentially the dilution-refrigerator version of the configuration used earlier by Michael Switkes in a $^3$He system. The line consists of three segments of semi-rigid coax[1]: (1) $\sim$ 1 m UT34-SS/SS [meaning Uniform Tube .034" outer conductor diameter, stainless steel (SS) inner conductor / SS outer conductor] from room temperature to the 1 K pot, (2) $\sim$ 30 cm UT34-SS/SS from the 1 K pot to the mixing chamber, and (3) $\sim$ 50 cm UT34-C (silver-plated Cu/Cu) from the mixing chamber to the sample holder. Stainless steel was chosen for the first two segments in order to minimize heat load at the thermal sinks located at the 1 K pot and mixing chamber. These sinks[2] – striplines of Au on sapphire substrate – help thermalize the coax inner conductor without introducing a resistance path to ground. The outer conductor is easily thermalized at both heat sinks and by tightly wound bare copper wire anchored to the 4 K plate and to the still. The coax inner and outer conductors are soldered directly to two pins of the sample holder.

This coax line was useful for applying CW at $f \lesssim 6$ GHz without requiring precise calibration of the ac power at the sample. The insertion loss in the lines was strongly frequency-dependent, partly due to strong attenuation in the SS coax segments[3], and partly

[1]With the exception of superconducting coax, all semi-rigid coax described in this appendix was purchased from Microstock, Inc. (http://www.microstock-inc.com).

[2]The design and fabrication of the heat sinks used are discussed in detail in Ap. C of Michael's thesis [106].

[3]To a good approximation, and due to the skin effect, the insertion loss (in dB) in a coax is proportional to $(f/\sigma)^{1/2} l/d$, with $\sigma$ and $d$ the conductivity and diameter of the inner conductor (keeping the impedance and dielectric fixed!) and $l$ the length [209]. For example, the insertion loss (in dB/m) at 1 GHz and room temperature is 10.4 in UT34-SS/SS, 4.1 in UT85-SS/SS. and 1.6 in UT34-C.

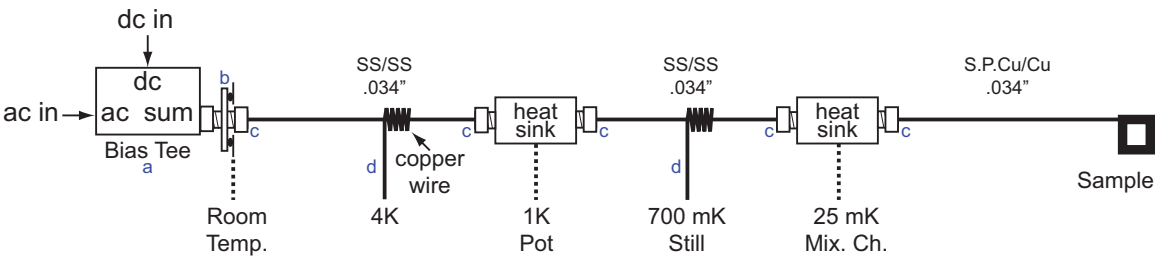


Description

a Bias tee (65 kHz - 20 GHz), Picosecond Pulse Labs 5545-107.

b SMA f-f hermetic feedthrough, Huber-Suhner (H-S) 34-SMA-50-0-3.

c SMA plug for .034" semi-rigid (s-r) coax, H-S 11-SMA-50-1-2, captivated with H-S 74-Z-0-0-116 epoxy, soldered.

d 30 or 24 AWG bare-copper wire, Arcor.

Figure A.1: Schematic of the coaxial line configuretion used in the photocurrent/rectification experiment (see Ch. 3).

due to resonances associated with the heat sinks (see black curve in Fig. A.3) and with the sample holder. A key feature of this line worth noting in view of the above-mentioned limitations is that the electrical isolation of the inner conductor allowed a dc signal to be coupled to the line using a bias tee at room temperature.

### A.1.2 Evolution

Following the photocurrent/rectification work, I teamed with Heather and Lily in a project aiming to measure Rabi oscillations of charge in tunnel-coupled double quantum dots in the Coulomb blockade regime. We did not obtain a single oscillation that we could link to charge-Rabi with certainty, but we did learn how to send broadband signals down the fridge. We were using a HP 8133a pulse generator with $\tau_r < 100$ ps and aimed to keep $\tau_r < 1$ ns for pulses after propagating down the line.

The initial effort was to minimize the frequency-dependent insertion loss in the existing setup. To this end, we redesigned the sapphire heat sinks using SMA jack launchers (see below). Another modest step included replacing segment 1 with CR85-B/SS (UT85-size, BeCu/SS). To maximize coupling to the dot gates without sacrificing the use of the Plastronics sample holder used ubiquitously in the lab fridges, we bypassed the sample holder pins by soldering UT34-C coax directly on the chip carrier (and holding carrier and coax

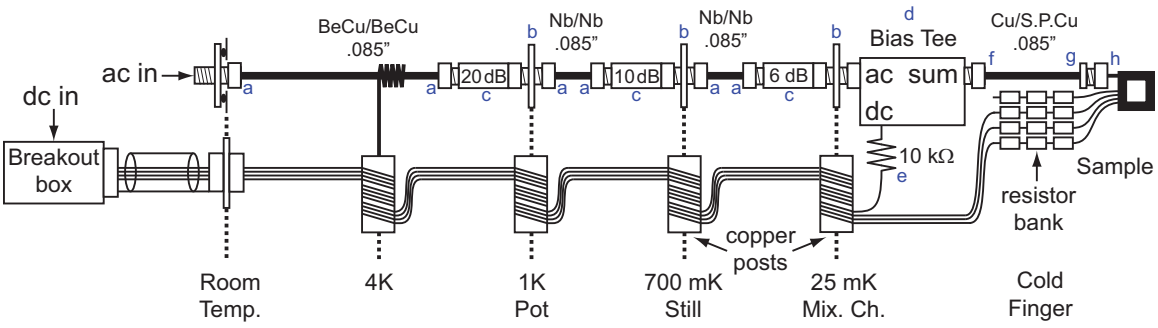


Description

a SMA crimp plug for .085" semi-rigid (s-r) coax, Tyco 1050611-1. Requires crimping tool (Tyco 1055835-1).
b SMA f-f feedthrough, H-S 34-SMA-50-0-51.
c SMA attenuator (DC-26.5 GHz), Midwest Microwave ATT-0298-XX-HEX-02 (XX=20,10,06).
d Bias Tee (50 kHz - 40 GHz), Anritsu K251 (50 kHz - 40 GHz).
e Vishay RN55D (non-magnetic), potted with Stycast 2850 on SMC plug (Midisco 8123-31-1).
f SMA plug for .085" s-r coax, H-S 11-SMA-50-2-15.
g SMA jack for .085" s-r coax, H-S 21-SMA-50-2-15.
h SMA plug for .034" s-r coax, H-S 11-SMA-50-1-2, captivated with H-S 74-Z-0-0-116 epoxy, soldered.

Figure A.2: Schematic diagram of the coaxial line implemented with the cold attenuator/bias tee technique. Unlabeled microwave components are already described in Fig. A.1. A dc signal is coupled to the dc port of the cold bias tee via a wire taken from the Oxford constantan loom that provides low-frequency wiring. This schematic is adapted from Fig. B.1 of Alex Johnson's thesis [74].

together using a drop of Stycast 2850). We did cut/file away a few pins from the sample holder.

Soon we recognized a better approach. Several groups had solved the technical problem of thermalizing the inner conductor by using broadband in-line attenuators (which provide a low resistance path to ground) at each stage of the cryostat. This approach also provided an easy solution to attenuating the thermal noise radiated by each cryostat stage toward the sample, at least for frequencies $f < k_B T_{\rm mc}/h$ ($T_{\rm mc}$ being the mixing-chamber temperature). The solution is to use power attenuation values at each cryostat stage (1 K pot, still and mixing chamber) roughly equal to the ratio of temperatures between each stage and the previous one. One disadvantge of this approach is that coupling a dc signal to the line requires placing a bias tee at the mixing chamber. Konrad Lehnert, at that time a post-doc with Prof. Robert Schoelkopf at Yale University, recommended Midwest Microwave attenuators and the Anritsu K251 ultra-wideband bias tee. This advice saved us much time and money! Many groups were struggling with more expensive attenuators

(in particular one from HP/Agilent) that shorted to ground at low temperature (by TaN going superconducting). Also, at 900 USD for each K251, knowing that this bias tee would still work when cooled was valuable.

Other changes made in order to flatten the frequency response of the line included replacing segment 1 with CR05BB (UT85-size BeCu/BeCu), using UT85-size Nb/Nb between the 1 K pot and the still, and between the still and the mixing chamber[4], and replacing segment 3 with UT85-C (silver-plated Cu/Cu). It is worth emphasizing that the Nb/Nb coax segments between the 1 K pot and the mixing chamber were not chosen to minimize thermal loads. It is a rather suprising fact (see Fig. 3.18 of Ref. [40]) that Nb is less thermally conductive than SS only below $\sim 80$ mK (see Fig. 3.18 of Ref. [40]). A final change involved using crimp SMA connectors on all non-Cu coax, partly out of the inability to solder to materials like Nb, and partly to make SMA connections more reliable [5].

A schematic of the finalized coaxial line is shown in Fig. A.2. This general scheme has been used widely by the group since then, mainly for pulsed-gated measurements in double quantum dots [35, 36], with small modifications. The required $\tau_r$ is typically a few ns and so more attenuating coax can be used, for example CR085BSS (UT85-size BeCu/SS) for segment 1 and UT85-SS/SS between the 1 K pot and the mixing chamber.

## A.2 Broadband sapphire heat sinks

The heat sinks that Heather, Lily and I made are shown in Fig. A.2. This design shares many similarities with Michael's, in particular the sapphire stripline and a machined copper

[4]We thank Keith Schwab, then at the Laboratory of Physical Sciences, for sending us some Nb/Nb coax at a time when purchasing small lengths of this coax in the U. S. was seemingly impossible.

[5]In my experience, it is easier to find unwanted wiggles in the insertion loss of a coax when connectors are soldered. Also, I have not had thermal-cycling problems with crimp connectors.

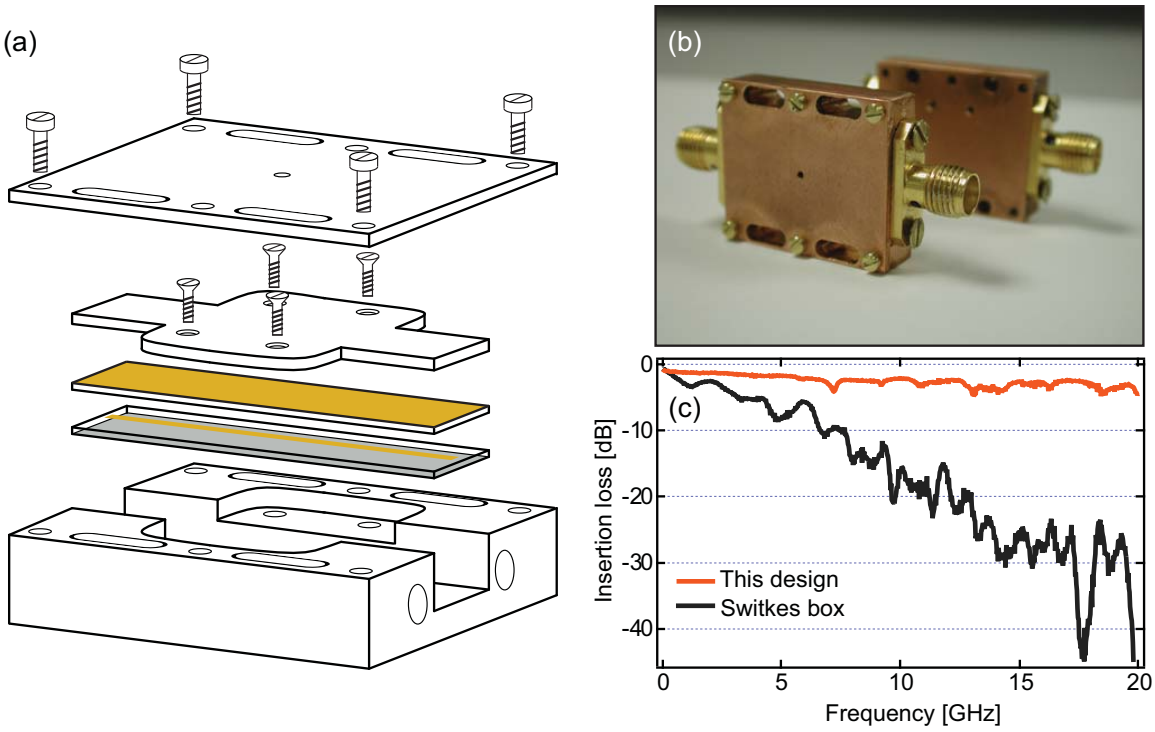


Figure A.3: (a) Schematic diagram of the broadband sapphire heat sinks. (b) Photograph of two assembled boxes (courtesy of Jeffrey Miller). (c) Insertion loss for this design and for the Switkes original, measured with the Tinkham/Westervelt HP 8510B network analyzer.

box[6]. The main difference is the use of a SMA panel jack launcher (H-S 23-SMA-50-0-166) rather than a segment of UT34-SS/SS connecting to the stripline (see App. C in [106]). Sapphire substrates[7] are .020" thick, 1.000" long and .250" wide, with polished surfaces and random optical-axis orientation. Each substrate has 10/200 nm of Cr/Au thermally evaporated on its back plane to maximize thermal contact to the copper box. On the front side of one substrate, a 10/200 nm Cr/Au , $\sim 0.18$ mm wide stripline is deposited by masked thermal evaporation[8]. This width makes the stripline impedance close to 50 Ω (see Section

[6]The three parts to the box (main body, cross-shaped top-plane and lid) were machined from oxygen-free high conductivity copper by Louis DeFeo's shop. Detailed drawings of these parts are available at the Marcus Lab wiki.

[7]Purchased at various times from Boston Piezo Optics and by University Wafer.

[8]All thermal evaporation is done using the Edwards Auto 306 evaporator in the Marcus Lab sample prep room.

3.7 in Ref. [209]).

During assembly, the lower substrate is first placed on the trench in the box main body. The SMA jack launchers are then screwed on at the sides. Thin launcher pins previously attached to the launchers are next aligned with the stripline. The top substrate is then positioned. The cross-shaped top-plane is then gently screwed in, mechanically securing the launcher pins between the two substrates. The top lid is then screwed on to the main body.

Initially we used commercial launcher pins, finding frequency-periodic oscillations in the insertion and return loss. Simulations using Sonnet-lite confirmed that these resulted from the pins being too wide. To mitigate the problem, short pieces of 0.2 mm-diameter silver plated copper wire (the inner conductor removed from a piece of UT34-C) were used as pins instead. A typical insertion loss for the completed heat sink is shown in Fig. A.3(c) and compared to that of the original Switkes design.

As mentioned, we did not get much use from these broadband heat sinks as we switched to the cold attenuator/bias-tee approach. However, the broadband heat sink has recently found application in David Reilly's rf-qpc reflectometry setup [37]. David uses the heat sink to thermalize (at the still) a UT85-size Nb/Nb coax segment extending from the sample to a cryogenic amplifier anchored to the 4 K plate. Here, the in-line attenuator approach is not an option since the attenuation would result in excessive signal loss. The signal transmitted on this line is $\sim -100$ dBm at $\sim 220$ MHz, CW. The insertion loss of the heat sink at this frequency is $< 1$ dB.

# Appendix B

# Derivation of double-dot equations (4.1) and (4.3)

## B.1 Equation (4.1)

This equation gives $\langle m \rangle$ and $\langle n \rangle$, the average electron number on the left and right dots, along the detuning diagonal [see Fig. 4.3(a)] at fixed total charge $M + N + 1$.

### B.1.1 Two-level Hamiltonian

We assume that the single-particle level spacing for the individual dots is large compared to (1) the electrostatic detuning $\epsilon$ between charge states $(M + 1, N)$ and $M, N + 1)$, (2) the tunnel coupling $t$ mixing the $(M + 1, N)$ and $(M, N + 1)$ states with lowest quantum confinement energy, and (3) the electron temperature $T_e$. We also assume that charge states with total electron number different from $M + N + 1$ are energy forbidden. In this limit, the double-dot can be modeled as a two-level system with Hamiltonian

$$H = \begin{pmatrix} \epsilon/2 & t \\ t & -\epsilon/2 \end{pmatrix}$$

in the basis $\{|M + 1, N\rangle, |M, N + 1\rangle\}$. The ground (excited) state of $H$ has energy $\mp\Omega/2$ and wavefunction

$$\begin{aligned} |\Psi_{\rm gnd}\rangle &= \left(\sqrt{1 - \epsilon/\Omega}\,|M + 1, N\rangle - \sqrt{1 + \epsilon/\Omega}\,|M, N + 1\rangle\right)/\sqrt{2} \\ |\Psi_{\rm exc}\rangle &= \left(\sqrt{1 + \epsilon/\Omega}\,|M + 1, N\rangle + \sqrt{1 - \epsilon/\Omega}\,|M, N + 1\rangle\right)/\sqrt{2} \end{aligned} .$$

Here, $\Omega = \sqrt{\epsilon^2 + 4t^2}$. The probability for finding the system in $(M+1, N)$ and $(M, N+1)$ while in the ground (excited) state is

$$\begin{aligned} P_{(M+1,N)|\mathrm{gnd(exc)}} &= \tfrac{1}{2}\left(1 \mp \epsilon/\Omega\right) \\ P_{(M,N+1)|\mathrm{gnd(exc)}} &= \tfrac{1}{2}\left(1 \pm \epsilon/\Omega\right) \end{aligned} .$$

### B.1.2 Thermal equilibrium

In thermal equilibrium, the probability $P_{\mathrm{gnd(exc)}}$ of the system being in the ground (excited) state is

$$\begin{aligned} P_{\mathrm{gnd}} &= \tfrac{1}{1+e^{-\Omega/k_BT_e}} = \tfrac{1}{2}\left[1 + \tanh\left(\tfrac{\Omega}{2k_BT_e}\right)\right] \\ P_{\mathrm{exc}} &= \tfrac{e^{-\Omega/k_BT_e}}{1+e^{-\Omega/k_BT_e}} = \tfrac{1}{2}\left[1 - \tanh\left(\tfrac{\Omega}{2k_BT_e}\right)\right] \end{aligned} .$$

The probability of finding the system in each of the charge states is

$$\begin{aligned} P_{M+1,N} &= P_{\mathrm{gnd}}P_{(M+1,N)|\mathrm{gnd}} + P_{\mathrm{exc}}P_{(M+1,N)|\mathrm{exc}} = \tfrac{1}{2}\left[1 - \tfrac{\epsilon}{\Omega}\tanh\left(\tfrac{\Omega}{2k_BT_e}\right)\right] \\ P_{M,N+1} &= P_{\mathrm{gnd}}P_{(M,N+1)|\mathrm{gnd}} + P_{\mathrm{exc}}P_{(M,N+1)|\mathrm{exc}} = \tfrac{1}{2}\left[1 + \tfrac{\epsilon}{\Omega}\tanh\left(\tfrac{\Omega}{2k_BT_e}\right)\right] \end{aligned} .$$

Finally, the average electron number on the left and right dots is

$$\begin{aligned} \langle m\rangle &= (M+1)P_{M+1,N} + MP_{M,N+1} = M + \tfrac{1}{2}\left[1 - \tfrac{\epsilon}{\Omega}\tanh\left(\tfrac{\Omega}{2k_BT_e}\right)\right] \\ \langle n\rangle &= NP_{M+1,N} + (N+1)P_{M,N+1} = N + \tfrac{1}{2}\left[1 + \tfrac{\epsilon}{\Omega}\tanh\left(\tfrac{\Omega}{2k_BT_e}\right)\right] \end{aligned} .$$

## B.2 Equation (4.3)

We use the model for electrostatic charging in a double-dot system developed in Ref. [111] (including notation) to derive Eq. (4.3). This equation gives the components $(\delta V_{g1}, \delta V_{g2})$ in the plane of plunger-gate voltages of the line connecting the two triple points at a honeycomb vertex. This triple-point separation results from finite interdot mutual capacitance $C_m$ and interdot tunnel coupling $t$. We find it convenient to use dimensionless gate voltages, defined as $\delta x_{1(2)} = \frac{C_{\mathrm{g1(g2)}}}{|e|}\delta V_{\mathrm{g1(g2)}}$. For simplicity, we assume dots 1 and 2 have the same individual charging energies, $E_{C1} = E_{C2} = E_C$, consistent with the experiment presented in Ch. 4.

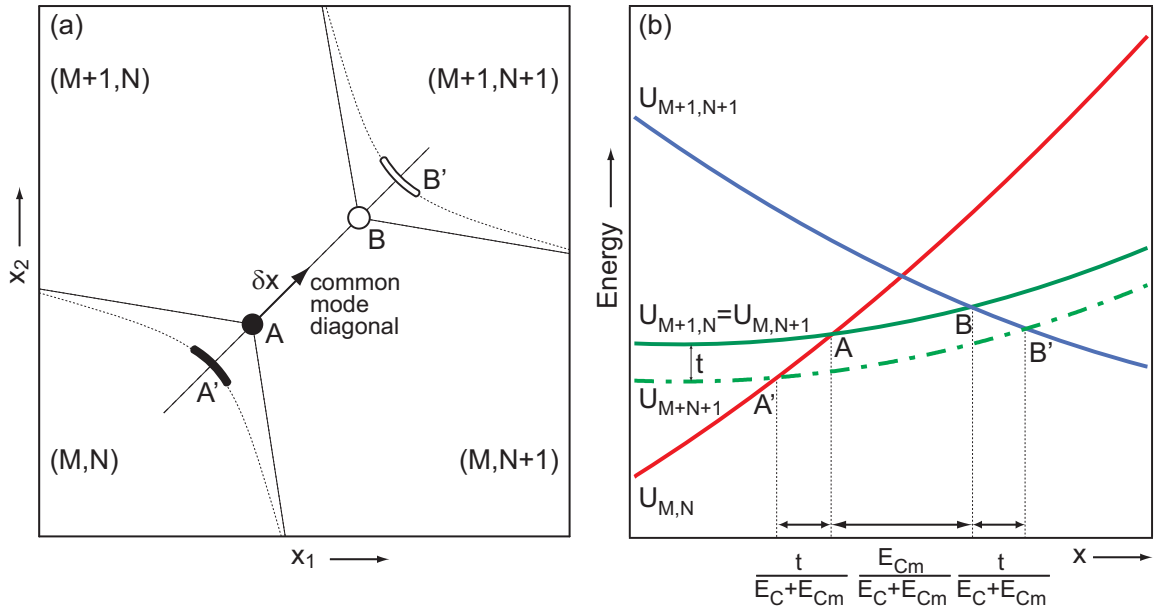


Figure B.1: (a) Diagram illustrating the separation between triple points at a honeycomb vertex in the space of dimensionless gate voltages. Circles (labeled A and B) represent the triple points at zero interdot tunnel coupling $t$. Cusps (labeled A' and B') represent the triple points at finite $t$. (b) Solid curves: total energy of charge states $(M,N)$, $(M+1,N)$, $(M,N+1)$, and $(M+1,N+1)$ along the common-mode diagonal for $t=0$. Finite $t$ hybridizes states $(M+1,N)$ and $(M,N+1)$ and lowers by $t$ the total energy of the $M+N+1$-electron ground state (dot-dashed curve).

### B.2.1 Triple-point separation for $t = 0$

Let us define the lower triple point (labeled A in Fig. B.1) as the origin of relative coordinates, i.e., $(\delta x_1, \delta x_2)$=(0,0). At triple point A, states $(M,N)$, $(M+1,N)$ and $(M,N+1)$ are degenerate, so that the total energies of these states (including both electrostatic and quantum confinement energies) satisfy $U_{M,N} = U_{M+1,N} = U_{M,N+1}$. We now find the coordinates of the upper triple point (labeled B), at which $U_{M+1,N} = U_{M,N+1} = U_{M+1,N+1}$. Energies $U_{M+1,N}$, $U_{M,N+1}$, and $U_{M+1,N+1}$, relative to $U_{M,N}$, depend on $\delta x_1$ and $\delta x_2$ as

$$\begin{pmatrix} U_{M+1,N} - U_{M,N} \\ U_{M,N+1} - U_{M,N} \\ U_{M+1,N+1} - U_{M,N} \end{pmatrix} = \begin{pmatrix} -E_C & -E_{Cm} \\ -E_{Cm} & -E_C \\ -(E_C + E_{Cm}) & -(E_C + E_{Cm}) \end{pmatrix} \begin{pmatrix} \delta x_1 \\ \delta x_2 \end{pmatrix} + \begin{pmatrix} 0 \\ 0 \\ E_{Cm} \end{pmatrix}.$$

The upper triple point must lie on the common-mode diagonal $\delta x_1 = \delta x_2 = \delta x$, along which $U_{M+1,N} = U_{M,N+1}$ and

$$\begin{pmatrix} U_{M+1,N} - U_{M,N} \\ U_{M+1,N+1} - U_{M,N} \end{pmatrix} = \begin{pmatrix} -(E_C + E_{Cm}) \\ -2(E_C + E_{Cm}) \end{pmatrix} \delta x + \begin{pmatrix} 0 \\ E_{Cm} \end{pmatrix}.$$

Thus, $U_{M+1,N} = U_{M,N+1} = U_{M+1,N+1}$ at $\delta x = E_{Cm}/(E_C + E_{Cm})$.

### B.2.2 Triple-point separation for $t \neq 0$

Along the common-mode diagonal, finite interdot coupling hybridizes states $(M+1, N)$ and $(M, N+1)$, lowering by an amount $t$ the energy $U_{M+N+1}$ of the (no-longer degenerate) M+N+1 electron ground state. Along the common-mode diagonal,

$$\begin{pmatrix} U_{M+N+1} - U_{M,N} \\ U_{M+1,N+1} - U_{M,N} \end{pmatrix} = \begin{pmatrix} -(E_C + E_{Cm}) \\ -2(E_C + E_{Cm}) \end{pmatrix} \delta x + \begin{pmatrix} -t \\ E_{Cm} \end{pmatrix}.$$

The lower triple point (labeled A' in Fig. B.1) occurs at $\delta x = -t/(E_C + E_{Cm})$, while the upper triple point (labeled B') occurs at $\delta x = (E_{Cm} + t)/(E_C + E_{Cm})$. The components of the line connecting points A' and B' are thus $\delta x_1 = \delta x_2 = (E_{Cm} + 2t)/(E_C + E_{Cm})$. Using the relation $E_{C(Cm)} = e^2 C_{o(m)}/(C_o^2 - C_m^2)$ ($C_o$ is the self-capacitance of each dot), we obtain

$$\delta x_1 = \delta x_2 = \frac{C_m}{C_o + C_m} + 2t\frac{C_o - C_m}{e^2},$$

which is Eq. (4.3).

# Appendix C

# Simulating transport through single and double quantum dots in the Coulomb-blockade regime

Simulations of sequential tunneling through quantum dots in the Coulomb blockade regime were very useful to our (the Noise Team) investigations (see Chapters 7 and 8) of noise cross-correlations in a double-quantum dot and of noise correlations in a multi-lead, multi-level dot. This appendix presents the code that implements our master equation simulations in MATLAB. When implementing these, I chose MATLAB over Igor as the platform because I was more familiar with matrix operations in MATLAB at the time. Yiming then translated this code into Igor's programming language, adding beautiful features along the way. For example, he generalized the code for the multi-level quantum dot so that the number of levels (limited to three in the code below) was user defined.

## C.1 Capacitively-coupled double quantum dot

This code simulates sequential tunneling through two capacitively-coupled, single-level quantum dots as described in Chapter 7. The code consists of three separate m-files: `ParamsDD`, `CoreDD`, and `GateGateDD`. `ParamsDD` defines (globally) the double-dot parameters. `CoreDD` computes the mean currents and noise spectral densities for the current bias conditions and double-dot parameters. `GateGateDD` does a two-dimensional 'sweep'

of plunger gate voltages at fixed bias, calling `ParamsDD` in the beginning and `CoreDD` at each step. To run a simulation, place the three m-files in one directory, which you then specify as the current working directory for MATLAB. Open `ParamsDD` in the editor, set the double-dot parameters, and save the file. Finally, run `GateGateDD` from the MATLAB prompt.

```
% File: ParamsDD.m
% -----------------
% This .m file defines parameters for two capacitively-coupled, single-level
% quantum dots.
% ------------------------------------------------------------------------
% Leo DiCarlo, Noise Team, Marcus Lab, Harvard University
%
% Notes:
% ------
% TL=top-left      TR=top-right
% BL=bottom-left   BR=bottom-right

clear all;  % clears all variables

% some constants
% --------------
q=1.6e-19;     % absolute electron charge, in Coulombs
kb=1.38e-23;   % Boltzmann constant, in Joules/Kelvin

Te=.28;                             % temperature, in K
U=q*60e-6;                          % mutual charging energy, in Joules
GammaTL=1.5e10; GammaTR=1.5e10;     % tunnel barrier transparencies, in inverse seconds
GammaBL=7.2e9; GammaBR=7.2e9;
BetaT=0.5; BetaB=0.5;               % capacitive divider for the leads, dimensionless

% dc bias on reservoirs, in uV
% ----------------------------
VbiasTL=+100; VbiasTR=0;
VbiasBL=+100; VbiasBR=0;

% plunger gates, in ueV
% ---------------------
VTC=0;  VBC=0;


% File: CoreDD.m
% ----------------------
% This .m file calculates the mean currents and current noise spectral
% densities for two capacitively-coupled, single-level dots.
% ------------------------------------------------------------------
% Leo DiCarlo, Noise Team, Marcus Lab, Harvard University
%
% Notes:
% ------
% - All matrices are in the {0,0), (1,0), (0,1), (1,1) basis, with the
% first (second) index indicating excess charge on the top (bottom) dot.
% - Notation is "to-from". For example, 0010 means 00<-10,  to (0,0)
% from 10.

% number operator
% ---------------
Ndd=[0 0 0 0;
     0 1 0 0;
     0 0 1 0;
     0 0 0 2];
```

```
% chemical potentials in the leads, in Joules
% ----------------------------------------
muTL=-q*1e-6*VbiasTL; muTR=-q*1e-6*VbiasTR;
muBL=-q*1e-6*VbiasBL; muBR=-q*1e-6*VbiasBR;

% energy levels in top and bottom dots.
% -------------------------------------
ET=-q*1e-6*((VbiasTL+VbiasTR)*BetaT + VTC+VBC/10)-U/2;   %ET=EB=0 at center of honeycomb vertex
EB=-q*1e-6*((VbiasBL+VbiasBR)*BetaB + VBC+VTC/10)-U/2;

% rates: (0,0) <-> (1,0)
% ----------------------
WL1000=GammaTL*(1/(exp((ET-muTL)/kb/Te)+1));
WR1000=GammaTR*(1/(exp((ET-muTR)/kb/Te)+1));
WL0010=GammaTL*(1-1/(exp((ET-muTL)/kb/Te)+1));
WR0010=GammaTR*(1-1/(exp((ET-muTR)/kb/Te)+1));

% rates: (0,0) <-> (0,1)
% ----------------------
WL0100=GammaBL*(1/(exp((EB-muBL)/kb/Te)+1));
WR0100=GammaBR*(1/(exp((EB-muBR)/kb/Te)+1));
WL0001=GammaBL*(1-1/(exp((EB-muBL)/kb/Te)+1));
WR0001=GammaBR*(1-1/(exp((EB-muBR)/kb/Te)+1));

% rates: (1,0) <-> (1,1)
% ----------------------
WL1110=GammaBL*(1/(exp((EB+U-muBL)/kb/Te)+1));
WR1110=GammaBR*(1/(exp((EB+U-muBR)/kb/Te)+1));
WL1011=GammaBL*(1-1/(exp((EB+U-muBL)/kb/Te)+1));
WR1011=GammaBR*(1-1/(exp((EB+U-muBR)/kb/Te)+1));

% rates: (0,1) <-> (1,1)
% ----------------------
WL1101=GammaTL*(1/(exp((ET+U-muTL)/kb/Te)+1));
WR1101=GammaTR*(1/(exp((ET+U-muTR)/kb/Te)+1));
WL0111=GammaTL*(1-1/(exp((ET+U-muTL)/kb/Te)+1));
WR0111=GammaTR*(1-1/(exp((ET+U-muTR)/kb/Te)+1));

GammaTot=GammaTL+GammaTR+GammaBL+GammaBR;
W1000=WL1000+WR1000;
W0010=WL0010+WR0010;
W0100=WL0100+WR0100;
W0001=WL0001+WR0001;
W1110=WL1110+WR1110;
W1011=WL1011+WR1011;
W1101=WL1101+WR1101;
W0111=WL0111+WR0111;

% the master matrix
% -----------------
Wmat=1/GammaTot*[   -(W1000+W0100)           W0010            W0001                0;
                           W1000  -(W0010+W1110)                0           W1011;
                           W0100                0  -(W0001+W1101)           W0111;
                               0           W1110            W1101  -(W1011+W0111)];

% steady state probability vector
% -------------------------------
rho_o=(null(Wmat))/sum(null(Wmat));

% current operators
% -----------------
JTL=-q*[             0   +WL0010          0            0;
              -WL1000          0          0            0;
                    0          0          0      +WL0111;
                    0          0    -WL1101            0];

JTR=-q*[             0   +WR0010          0            0;
              -WR1000          0          0            0;
```

```
                    0         0          0      +WR0111;
                    0         0    -WR1101            0];

JBL=-q*[            0         0    +WL0001            0;
                    0         0          0      +WL1011;
               -WL0100        0          0            0;
                    0   -WL1110          0            0];

JBR=-q*[            0         0    +WR0001            0;
                    0         0          0      +WR1011;
               -WR0100        0          0            0;
                    0   -WR1110          0            0];

% mean currents, in A
% -------------------
ITL=sum(JTL*rho_o); ITR=sum(JTR*rho_o);
IBL=sum(JBL*rho_o); IBR=sum(JBR*rho_o);

% spectral densities
% ------------------
sizeWmat=size(Wmat,1);
[Umat,Dmat]=eig(Wmat,'nobalance');
for m=1:sizeWmat
    currLambda=Dmat(m,m);
    if abs(currLambda)>1e-9;
        Dmat(m,m)=1/(currLambda*GammaTot);
    else
        Dmat(m,m)=0;
    end
end

invUmat=inv(Umat);

%power spectral densities, in A^2/Hz
%-----------------------------------
SITLTL= -2*sum(JTL*Umat*Dmat*invUmat*JTL*rho_o + JTL*Umat*Dmat*invUmat*JTL*rho_o - q*(Ndd*JTL-JTL*Ndd)*rho_o);
SITRTR= -2*sum(JTR*Umat*Dmat*invUmat*JTR*rho_o + JTR*Umat*Dmat*invUmat*JTR*rho_o - q*(Ndd*JTR-JTR*Ndd)*rho_o);
SIBLBL= -2*sum(JBL*Umat*Dmat*invUmat*JBL*rho_o + JBL*Umat*Dmat*invUmat*JBL*rho_o - q*(Ndd*JBL-JBL*Ndd)*rho_o);
SIBRBR= -2*sum(JBR*Umat*Dmat*invUmat*JBR*rho_o + JBR*Umat*Dmat*invUmat*JBR*rho_o - q*(Ndd*JBR-JBR*Ndd)*rho_o);
%cross spectral densities, in A^2/Hz
SITRTL= -2*sum(JTR*Umat*Dmat*invUmat*JTL*rho_o + JTL*Umat*Dmat*invUmat*JTR*rho_o);
SIBLTL= -2*sum(JBL*Umat*Dmat*invUmat*JTL*rho_o + JTL*Umat*Dmat*invUmat*JBL*rho_o);
SIBRTL= -2*sum(JBR*Umat*Dmat*invUmat*JTL*rho_o + JTL*Umat*Dmat*invUmat*JBR*rho_o);
SITLTR=SITRTL;
SIBLTR= -2*sum(JBL*Umat*Dmat*invUmat*JTR*rho_o + JTR*Umat*Dmat*invUmat*JBL*rho_o);
SIBRTR= -2*sum(JBR*Umat*Dmat*invUmat*JTR*rho_o + JTR*Umat*Dmat*invUmat*JBR*rho_o);
SITLBL= SIBLTL;
SITRBL= SIBLTR;
SIBRBL= -2*sum(JBR*Umat*Dmat*invUmat*JBL*rho_o + JBL*Umat*Dmat*invUmat*JBR*rho_o);
SITLBR= SIBRTL;
SITRBR= SIBRTR;
SIBLBR= SIBRBL;


% File: GateGateDD.m
% ------------------
% This .m file calculates mean currents, current noise spectral densitites,
% and conductance matrix elements for two capacitively-coupled single-level quantum
% dot as a function of two plunger gate voltage, at fixed bias.
% ---------------------------------------------------------------------------
% Leo DiCarlo, Noise Team, Marcus Lab, Harvard University

ParamsDD;  % run .m file with double-dot parameters

% initialize output matrices
% --------------------------
ITLmat=[]; ITRmat=[];
IBLmat=[]; IBRmat=[];
```

```
SITLTLmat=[];   SITLTRmat=[];   SITLBLmat=[];   SITLBRmat=[];
SITRTLmat=[];   SITRTRmat=[];   SITRBLmat=[];   SITRBRmat=[];
SIBLTLmat=[];   SIBLTRmat=[];   SIBLBLmat=[];   SIBLBRmat=[];
SIBRTLmat=[];   SIBRTRmat=[];   SIBRBLmat=[];   SIBRBRmat=[];

GTLTLmat=[]; GTLTRmat=[]; GTLBLmat=[];GTLBRmat=[];
GTRTLmat=[]; GTRTRmat=[]; GTRBLmat=[];GTRBRmat=[];
GBLTLmat=[]; GBLTRmat=[]; GBLBLmat=[];GBLBRmat=[];
GBRTLmat=[]; GBRTRmat=[]; GBRBLmat=[];GBRBRmat=[];

% specify 2D range to cover
% -------------------------
VTCvec=linspace(-200,200,51); % in ueV
VBCvec=linspace(-200,200,51); % in ueV

for VBC=VBCvec;
    ITLvec=[]; ITRvec=[];
    IBLvec=[]; IBRvec=[];

    SITLTLvec=[];   SITLTRvec=[];   SITLBLvec=[];   SITLBRvec=[];
    SITRTLvec=[];   SITRTRvec=[];   SITRBLvec=[];   SITRBRvec=[];
    SIBLTLvec=[];   SIBLTRvec=[];   SIBLBLvec=[];   SIBLBRvec=[];
    SIBRTLvec=[];   SIBRTRvec=[];   SIBRBLvec=[];   SIBRBRvec=[];

    GTLTLvec=[]; GTLTRvec=[]; GTLBLvec=[];GTLBRvec=[];
    GTRTLvec=[]; GTRTRvec=[]; GTRBLvec=[];GTRBRvec=[];
    GBLTLvec=[]; GBLTRvec=[]; GBLBLvec=[];GBLBRvec=[];
    GBRTLvec=[]; GBRTRvec=[]; GBRBLvec=[];GBRBRvec=[];

    for VTC=VTCvec;
        CoreDD;
        % get mean currents, in A
        % -----------------------
        ITLvec=[ITLvec; ITL]; ITRvec=[ITRvec; ITR];
        IBLvec=[IBLvec; IBL]; IBRvec=[IBRvec; IBR];

        % get spectral densities, in A^2/Hz
        % ---------------------------------
        SITLTLvec=[SITLTLvec;SITLTL];SITLTRvec=[SITLTRvec;SITLTR];
                                SITLBLvec=[SITLBLvec;SITLBL];SITLBRvec=[SITLBRvec;SITLBR];
        SITRTRvec=[SITRTLvec;SITRTL];SITRTRvec=[SITRTRvec;SITRTR];
                                SITRBLvec=[SITRBLvec;SITRBL];SITRBRvec=[SITRBRvec;SITRBR];
        SIBLTLvec=[SIBLTLvec;SIBLTL];SIBLTRvec=[SIBLTRvec;SIBLTR];
                                SIBLBLvec=[SIBLBLvec;SIBLBL];SIBLBRvec=[SIBLBRvec;SIBLBR];
        SIBRTLvec=[SIBRTLvec;SIBRTL];SIBRTRvec=[SIBRTRvec;SIBRTR];
                                SIBRBLvec=[SIBRBLvec;SIBRBL];SIBRBRvec=[SIBRBRvec;SIBRBR];

        % get differential conductances, in e^2/h
        % ----------------------------------------
        ITLm=ITL; ITRm=ITR;
        IBLm=IBL; IBRm=IBR;

        VbiasTL=VbiasTL+1; CoreDD; VbiasTL=VbiasTL-1;
        ITLp=ITL; ITRp=ITR;
        IBLp=IBL; IBRp=IBR;
        GTLTLvec=[GTLTLvec; (ITLp-ITLm)/1e-6*25812]; GTRTLvec=[GTRTLvec; (ITRp-ITRm)/1e-6*25812];
        GBLTLvec=[GBLTLvec; (IBLp-IBLm)/1e-6*25812]; GBRTLvec=[GBRTLvec; (IBRp-IBRm)/1e-6*25812];

        VbiasTR=VbiasTR+1; CoreDD; VbiasTR=VbiasTR-1;
        ITLp=ITL; ITRp=ITR;
        IBLp=IBL; IBRp=IBR;
        GTLTRvec=[GTLTRvec; (ITLp-ITLm)/1e-6*25812]; GTRTRvec=[GTRTRvec; (ITRp-ITRm)/1e-6*25812];
        GBLTRvec=[GBLTRvec; (IBLp-IBLm)/1e-6*25812]; GBRTRvec=[GBRTRvec; (IBRp-IBRm)/1e-6*25812];

        VbiasBL=VbiasBL+1; CoreDD; VbiasBL=VbiasBL-1;
        ITLp=ITL; ITRp=ITR;
        IBLp=IBL; IBRp=IBR;
        GTLBLvec=[GTLBLvec; (ITLp-ITLm)/1e-6*25812]; GTRBLvec=[GTRBLvec; (ITRp-ITRm)/1e-6*25812];
```

```
        GBLBLvec=[GBLBLvec; (IBLp-IBLm)/1e-6*25812]; GBRBLvec=[GBRBLvec; (IBRp-IBRm)/1e-6*25812];

        VbiasBR=VbiasBR+1; CoreDD; VbiasBR=VbiasBR-1;
        ITLp=ITL; ITRp=ITR;
        IBLp=IBL; IBRp=IBR;
        GTLBRvec=[GTLBRvec; (ITLp-ITLm)/1e-6*25812]; GTRBRvec=[GTRBRvec; (ITRp-ITRm)/1e-6*25812];
        GBLBRvec=[GBLBRvec; (IBLp-IBLm)/1e-6*25812]; GBRBRvec=[GBRBRvec; (IBRp-IBRm)/1e-6*25812];
    end

    ITLmat=[ITLmat ITLvec];  ITRmat=[ITRmat ITRvec];
    IBLmat=[IBLmat IBLvec];  IBRmat=[IBRmat IBRvec];

    SITLTLmat=[SITLTLmat SITLTLvec];SITLTRmat=[SITLTRmat SITLTRvec];
                                SITLBLmat=[SITLBLmat SITLBLvec];SITLBRmat=[SITLBRmat SITLBRvec];
    SITRTLmat=[SITRTLmat SITRTLvec];SITRTRmat=[SITRTRmat SITRTRvec];
                                SITRBLmat=[SITRBLmat SITRBLvec];SITRBRmat=[SITRBRmat SITRBRvec];
    SIBLTLmat=[SIBLTLmat SIBLTLvec];SIBLTRmat=[SIBLTRmat SIBLTRvec];
                                SIBLBLmat=[SIBLBLmat SIBLBLvec];SIBLBRmat=[SIBLBRmat SIBLBRvec];
    SIBRTLmat=[SIBRTLmat SIBRTLvec];SIBRTRmat=[SIBRTRmat SIBRTRvec];
                                SITLBLmat=[SIBRBLmat SIBRBLvec];SIBRBRmat=[SIBRBRmat SIBRBRvec];

    GTLTLmat=[GTLTLmat GTLTLvec];GTLTRmat=[GTLTRmat GTLTRvec];
                                GTLBLmat=[GTLBLmat GTLBLvec];GTLBRmat=[GTLBRmat GTLBRvec];
    GTRTLmat=[GTRTLmat GTRTLvec];GTRTRmat=[GTRTRmat GTRTRvec];
                                GTRBLmat=[GTRBLmat GTRBLvec];GTLBRmat=[GTRBRmat GTRBRvec];
    GBLTLmat=[GBLTLmat GBLTLvec];GBLTRmat=[GBLTRmat GBLTRvec];
                                GBLBLmat=[GBLBLmat GBLBLvec];GBLBRmat=[GBLBRmat GBLBRvec];
    GBRTLmat=[GBRTLmat GBRTLvec];GBRTRmat=[GBRTRmat GBRTRvec];
                                GBRBLmat=[GBRBLmat GBRBLvec];GBRBRmat=[GBRBRmat GBRBRvec];
end

% plot some of the results
% ------------------------
figure(1);
    pcolor(VBCvec,VTCvec,real(SITRBRmat));
    colormap(jet); colorbar('vert'); shading interp;
    xlabel('Vbc [ueV] '); ylabel('Vtc [ueV] '); title('Cross-spectral density [Asq/Hz]');
figure(2);
    pcolor(VBCvec,VTCvec,real(GTRTLmat))
    colormap(hot); colorbar('vert'); shading interp;
    xlabel('Vbc [ueV]'); ylabel('Vtc [ueV]'); title('Gtrtl [e^2/h]');
figure(3);
    pcolor(VBCvec,VTCvec,real(GBRBLmat))
    colormap(hot); colorbar('vert'); shading interp;
    xlabel('Vbc [ueV] '); ylabel('Vtc [ueV] '); title('Gbrbl [e^2/h]');
```

## C.2 Three-lead, multi-level quantum dot

This code simulates sequential tunneling through a three-lead, three-level quantum dot. While this code is a 'poor-man's' version of the one finally used in Chapter 8 (which uses a user-specified number of levels), it suffices for illustrating dynamical channel blockade.

The code consists of four separate m-files: `Params3L`, `Core3L`, and `vsGate3L`, and `Diamond3L`. `Params3L` defines (globally) the dot parameters. `Core3L` computes the mean currents and noise spectral densities for the current bias conditions and dot parameters.

vsGate3L does a 'sweep' of plunger gate voltage at fixed bias, calling Core3L at each step. Diamond3L does a two-dimensional 'sweep' of plunger gate voltage and bias, calling Params3L at the start and then vsGate3L inside a loop, and producing the so-called Coulomb diamonds of mean current, differential conductance and current noise spectral density. To run a simulation, open Params3L in the editor, set the dot parameters, and save the file. Finally, run Diamond3L from the MATLAB prompt.

```
%% File: Params3L.m
%% ----------------
%% This .m file defines parameters of
%% the 3-lead dot parameters
%% ------------------------------------------------
%% Leo DiCarlo, Noise Team, Marcus Lab, Harvard University

clear all; % clears all variables

% some constants
% --------------
q=1.6e-19;      % absolute electron charge, in Coulombs
kb=1.38e-23;    % Boltzmann constant, in Joules/Kelvin

Te=0.05;        % temperature, in K

% dot level structure
% ---------------------
Ep1=q*100e-6;   % single particle level (+1), in Joules
E0=q*0e-6;      % single particle level (+0), in Joules
Em1=q*-100e-6;  % single particle level (-1), in Joules

% tunnel barrier transparencies, in inverse seconds
% -------------------------------------------------
Gamma0p1=1e9; Gamma1p1=1e9;   Gamma2p1=0;       % for Level +1
Gamma00=1e9;  Gamma10=1e9;    Gamma20=0;        % for level 0
Gamma0m1=1e9; Gamma1m1=1e9;   Gamma2m1=0;       % for level -1

Beta=0.3;   % Capacitive divider for the leads,

% dc bias on reservoirs, in uV
% ----------------------------
Vbias0=0; Vbias1=0; Vbias2=0;

% plunger gate voltage, in ueV
% ----------------------------
Vg=0;

% File: Core3L.m
% --------------
% This .m file calculates the mean current and noise spectral densities for
% the 3-lead, 3 level quantum dot.
% ------------------------------------------------------------------------
% Leo DiCarlo, NoiseTeam, Marcus Lab, Harvard University
%
% Notes:
% ------
%
% - electron levels are labeled as
%   ----- p1
%   ----- 0
%   ----- m1
%
```

```
% - 1-electron states are labeled as
%     A        B        C
%   -----    -----    --x--
%   -----    --x--    -----
%   --x--    -----    -----
%
% - 2-electron states will be labeled as
%     X        Y        Z
%   -----    --x--    --x--
%   --x--    -----    --x--
%   --x--    --x--    -----
%
% - all matrices below are in the A, B, C, X, Y, Z basis

% allowed transitions and their energies
% --------------------------------------
EXA=E0;
EYA=Ep1;
EXB=Em1;
EZB=Ep1;
EYC=Em1;
EZC=E0;

% number operator
% ---------------
Nd=[1 0 0 0 0 0;
    0 1 0 0 0 0;
    0 0 1 0 0 0;
    0 0 0 2 0 0;
    0 0 0 0 2 0;
    0 0 0 0 0 2];

% dot chemical potential
% ----------------------
muD=-q*1e-6*((Vbias0+Vbias1+Vbias2)*Beta+Vg);

% chemical potentials in the leads, in Joules
% -------------------------------------------
mu0=-q*1e-6*Vbias0; mu1=-q*1e-6*Vbias1; mu2=-q*1e-6*Vbias2;

% rates A <-> X
% --------------
W0XA=Gamma00*(1/(exp((muD+EXA-mu0)/kb/Te)+1));
W1XA=Gamma10*(1/(exp((muD+EXA-mu1)/kb/Te)+1));
W2XA=Gamma20*(1/(exp((muD+EXA-mu2)/kb/Te)+1));
W0AX=Gamma00*(1-1/(exp((muD+EXA-mu0)/kb/Te)+1));
W1AX=Gamma10*(1-1/(exp((muD+EXA-mu1)/kb/Te)+1));
W2AX=Gamma20*(1-1/(exp((muD+EXA-mu2)/kb/Te)+1));

% rates A <-> Y
% --------------
W0YA=Gamma0p1*(1/(exp((muD+EYA-mu0)/kb/Te)+1));
W1YA=Gamma1p1*(1/(exp((muD+EYA-mu1)/kb/Te)+1));
W2YA=Gamma2p1*(1/(exp((muD+EYA-mu2)/kb/Te)+1));
W0AY=Gamma0p1*(1-1/(exp((muD+EYA-mu0)/kb/Te)+1));
W1AY=Gamma1p1*(1-1/(exp((muD+EYA-mu1)/kb/Te)+1));
W2AY=Gamma2p1*(1-1/(exp((muD+EYA-mu2)/kb/Te)+1));

% rates B <-> X
% --------------
W0XB=Gamma0m1*(1/(exp((muD+EXB-mu0)/kb/Te)+1));
W1XB=Gamma1m1*(1/(exp((muD+EXB-mu1)/kb/Te)+1));
W2XB=Gamma2m1*(1/(exp((muD+EXB-mu2)/kb/Te)+1));
W0BX=Gamma0m1*(1-1/(exp((muD+EXB-mu0)/kb/Te)+1));
W1BX=Gamma1m1*(1-1/(exp((muD+EXB-mu1)/kb/Te)+1));
W2BX=Gamma2m1*(1-1/(exp((muD+EXB-mu2)/kb/Te)+1));

% rates B <-> Z
```

```
% --------------
W0ZB=Gamma0p1*(1/(exp((muD+EZB-mu0)/kb/Te)+1));
W1ZB=Gamma1p1*(1/(exp((muD+EZB-mu1)/kb/Te)+1));
W2ZB=Gamma2p1*(1/(exp((muD+EZB-mu2)/kb/Te)+1));
W0BZ=Gamma0p1*(1-1/(exp((muD+EZB-mu0)/kb/Te)+1));
W1BZ=Gamma1p1*(1-1/(exp((muD+EZB-mu1)/kb/Te)+1));
W2BZ=Gamma2p1*(1-1/(exp((muD+EZB-mu2)/kb/Te)+1));

% rates C <-> Y
% --------------
W0YC=Gamma0m1*(1/(exp((muD+EYC-mu0)/kb/Te)+1));
W1YC=Gamma1m1*(1/(exp((muD+EYC-mu1)/kb/Te)+1));
W2YC=Gamma2m1*(1/(exp((muD+EYC-mu2)/kb/Te)+1));
W0CY=Gamma0m1*(1-1/(exp((muD+EYC-mu0)/kb/Te)+1));
W1CY=Gamma1m1*(1-1/(exp((muD+EYC-mu1)/kb/Te)+1));
W2CY=Gamma2m1*(1-1/(exp((muD+EYC-mu2)/kb/Te)+1));

% rates C <-> Z
% -------------
W0ZC=Gamma0p1*(1/(exp((muD+EZC-mu0)/kb/Te)+1));
W1ZC=Gamma1p1*(1/(exp((muD+EZC-mu1)/kb/Te)+1));
W2ZC=Gamma2p1*(1/(exp((muD+EZC-mu2)/kb/Te)+1));
W0CZ=Gamma0p1*(1-1/(exp((muD+EZC-mu0)/kb/Te)+1));
W1CZ=Gamma1p1*(1-1/(exp((muD+EZC-mu1)/kb/Te)+1));
W2CZ=Gamma2p1*(1-1/(exp((muD+EZC-mu2)/kb/Te)+1));

GammaTot=(Gamma0m1+Gamma1m1+Gamma2m1)+(Gamma00+Gamma10+Gamma20)+(Gamma0p1+Gamma1p1+Gamma2p1);
WXA=(W0XA+W1XA+W2XA); WAX=(W0AX+W1AX+W2AX);
WYA=(W0YA+W1YA+W2YA); WAY=(W0AY+W1AY+W2AY);
WXB=(W0XB+W1XB+W2XB); WBX=(W0BX+W1BX+W2BX);
WZB=(W0ZB+W1ZB+W2ZB); WBZ=(W0BZ+W1BZ+W2BZ);
WYC=(W0YC+W1YC+W2YC); WCY=(W0CY+W1CY+W2CY);
WZC=(W0ZC+W1ZC+W2ZC); WCZ=(W0CZ+W1CZ+W2CZ);

% the master matrix
% -----------------
Wmat=1/GammaTot*[-(WXA+WYA)         0             0         WAX        WAY            0;
                          0 -(WXB+WZB)            0         WBX          0          WBZ;
                          0         0   -(WYC+WZC)           0        WCY          WCZ;
                        WXA       WXB             0  -(WAX+WBX)          0            0;
                        WYA         0           WYC           0 -(WAY+WCY)            0;
                          0       WZB           WZC           0          0   -(WBZ+WCZ)];

% steady state probability vector
% -------------------------------
rho_o=(null(Wmat))/sum(null(Wmat));

% current operators
% -----------------
J0=-q*[     0      0      0  +W0AX  +W0AY      0;
            0      0      0  +W0BX      0  +W0BZ;
            0      0      0      0  +W0CY  +W0CZ;
        -W0XA  -W0XB      0      0      0      0;
        -W0YA      0  -W0YC      0      0      0;
            0  -W0ZB  -W0ZC      0      0      0];

J1=-q*[     0      0      0  +W1AX  +W1AY      0;
            0      0      0  +W1BX      0  +W1BZ;
            0      0      0      0  +W1CY  +W1CZ;
        -W1XA  -W1XB      0      0      0      0;
        -W1YA      0  -W1YC      0      0      0;
            0  -W1ZB  -W1ZC      0      0      0];

J2=-q*[    0      0      0   +W2AX  +W2AY      0;
            0      0      0  +W2BX      0  +W2BZ;
            0      0      0      0  +W2CY  +W2CZ;
        -W2XA  -W2XB      0      0      0      0;
        -W2YA      0  -W2YC      0      0      0;
```

```
            0  -W2ZB  -W2ZC      0      0      0];

% average currents, in A
% ----------------------
I0=sum(J0*rho_o); I1=sum(J1*rho_o); I2=sum(J2*rho_o);

%power spectral densities (in A^2/Hz)
% -----------------------------------
sizeWmat=size(Wmat,1);
[Umat,Dmat]=eig(Wmat);

for m=1:sizeWmat
   currLambda=Dmat(m,m);
   if abs(currLambda)>1e-9;
       Dmat(m,m)=1/currLambda/GammaTot;
   else
       Dmat(m,m)=0;
   end
end

invUmat=inv(Umat);

SI00= -2*sum(J0*Umat*Dmat*invUmat*J0*rho_o + J0*Umat*Dmat*invUmat*J0*rho_o - q*(Nd*J0-J0*Nd)*rho_o);
SI11= -2*sum(J1*Umat*Dmat*invUmat*J1*rho_o + J1*Umat*Dmat*invUmat*J1*rho_o - q*(Nd*J1-J1*Nd)*rho_o);
SI22= -2*sum(J2*Umat*Dmat*invUmat*J2*rho_o + J2*Umat*Dmat*invUmat*J2*rho_o - q*(Nd*J2-J2*Nd)*rho_o);
SI10= -2*sum(J1*Umat*Dmat*invUmat*J0*rho_o + J0*Umat*Dmat*invUmat*J1*rho_o);
SI20= -2*sum(J2*Umat*Dmat*invUmat*J0*rho_o + J0*Umat*Dmat*invUmat*J2*rho_o);
SI01= SI10;
SI21= -2*sum(J2*Umat*Dmat*invUmat*J1*rho_o + J1*Umat*Dmat*invUmat*J2*rho_o);
SI02= SI20;
SI12= SI21;


% File: vsGate3L.m
% ----------------
% This .m file calculates the average currents and noise spectral densities
% as a function of gate voltage, at fixed bias, for a 3-lead quantum dot.
% ------------------------------------------------------------------------
% Leo DiCarlo, Noise Team, Marcus Lab, Harvard University

% initialize output vectors
I0vec=[]; I1vec=[]; I2vec=[];

SI00vec=[]; SI01vec=[]; SI02vec=[];
SI10vec=[]; SI11vec=[]; SI12vec=[];
SI20vec=[]; SI21vec=[]; SI22vec=[];

Fano0vec=[]; Fano1vec=[]; Fano2vec=[];
ExPs0vec=[]; ExPs1vec=[]; ExPs2vec=[];

G00vec=[]; G01vec=[]; G02vec=[];
G10vec=[]; G11vec=[]; G12vec=[];
G20vec=[]; G21vec=[]; G22vec=[];

for Vg=Vgvec;
    Core3L;   % calculate mean currents and spectral densities at current Vg.
    % mean currents, in A
    % -------------------
    I0vec=[I0vec; I0]; I1vec=[I1vec; I1]; I2vec=[I2vec; I2];
    % spectral densities, in 2eA
    % --------------------------
    SI00vec=[SI00vec; SI00/2/q]; SI01vec=[SI01vec; SI01/2/q]; SI02vec=[SI02vec; SI02/2/q];
    SI10vec=[SI10vec; SI10/2/q]; SI11vec=[SI11vec; SI11/2/q]; SI12vec=[SI12vec; SI12/2/q];
    SI20vec=[SI20vec; SI20/2/q]; SI21vec=[SI21vec; SI21/2/q]; SI22vec=[SI22vec; SI22/2/q];

    % Fano factors, dimensionless
    % ---------------------------
    Fano0vec=[Fano0vec; SI00/2/q/abs(I1)];
    Fano1vec=[Fano1vec; SI11/2/q/abs(I1)];
```

```
    Fano2vec=[Fano2vec; SI22/2/q/abs(I2)];

    % excess Poissonian noise, in 2eA
    % -------------------------------
    ExPs0vec=[ExPs0vec; SI00/2/q-abs(I0)];
    ExPs1vec=[ExPs1vec; SI11/2/q-abs(I1)];
    ExPs2vec=[ExPs2vec; SI22/2/q-abs(I2)];

    % Differential conductance matrix, e^2/h
    % ---------------------------------------
    I0m=I0; I1m=I1; I2m=I2;

    Vbias0=Vbias0+1; Core3L; Vbias0=Vbias0-1;
    I0p=I0; I1p=I1; I2p=I2;
    G00=(I0p-I0m)/1e-6*25812; G10=(I1p-I1m)/1e-6*25812; G20=(I2p-I2m)/1e-6*25812;

    Vbias1=Vbias1+1; Core3L; Vbias1=Vbias1-1;
    I0p=I0; I1p=I1; I2p=I2;
    G01=(I0p-I0m)/1e-6*25812; G11=(I1p-I1m)/1e-6*25812; G21=(I2p-I2m)/1e-6*25812;

    Vbias2=Vbias2+1; Core3L; Vbias2=Vbias2-1;
    I0p=I0; I1p=I1; I2p=I2;
    G02=(I0p-I0m)/1e-6*25812; G12=(I1p-I1m)/1e-6*25812; G22=(I2p-I2m)/1e-6*25812;

    G00vec=[G00vec; -G00]; G01vec=[G01vec; G01]; G02vec=[G02vec; G02]; %multiplied diagonal elements by -1 to make them
    G10vec=[G10vec; G10]; G11vec=[G11vec; -G11]; G12vec=[G12vec; G12];
    G20vec=[G20vec; G20]; G21vec=[G21vec; G21]; G22vec=[G22vec; -G22];
end

% File: Diamond3L.m
% -----------------
% This .m file calculates differential conductance, mean current and current
% noise spectral density  as a function of gate voltage and bias for a
% 3-lead quantum dot with 3 quantum levels.
% ------------------------------------------------------------------------
% Leo DiCarlo, Noise Team, Harvard University

params3L; % run .m file with 3-lead dot parameters

% specify the gate voltage range, in ueV
% --------------------------------------
Vgvec=linspace(-300,300,201);

% specify the source-drian bias range, in uV
% ------------------------------------------
Vsdvec=linspace(-400,400,201);

% initialize output matrices
% --------------------------
I0mat=[]; I1mat=[]; I2mat=[];

SI00mat=[]; SI10mat=[]; SI20mat=[];
SI01mat=[]; SI11mat=[]; SI21mat=[];
SI02mat=[]; SI12mat=[]; SI22mat=[];

Fano0mat=[]; Fano1mat=[]; Fano2mat=[];
ExPs0mat=[]; ExPs1mat=[]; ExPs2mat=[];

G00mat=[]; G01mat=[]; G02mat=[];
G10mat=[]; G11mat=[]; G12mat=[];
G20mat=[]; G21mat=[]; G22mat=[];

for Vsd=Vsdvec;
   Vbias0=Vsd; Vbias1=0; Vbias2=0;
   vsGate3L;  %sweep of gate voltage
   I0mat=[I0mat I0vec]; I1mat=[I1mat I1vec]; I2mat=[I2mat I2vec];

   SI00mat=[SI00mat SI00vec]; SI01mat=[SI01mat SI01vec]; SI02mat=[SI02mat SI02vec];
```

```
   SI10mat=[SI10mat SI10vec]; SI11mat=[SI11mat SI11vec]; SI02mat=[SI12mat SI12vec];
   SI20mat=[SI20mat SI20vec]; SI21mat=[SI21mat SI21vec]; SI02mat=[SI22mat SI22vec];

   Fano0mat=[Fano0mat Fano0vec]; Fano1mat=[Fano1mat Fano1vec]; Fano2mat=[Fano2mat Fano2vec];
   ExPs0mat=[ExPs0mat ExPs0vec]; ExPs1mat=[ExPs1mat ExPs1vec]; ExPs2mat=[ExPs2mat ExPs2vec];

   G00mat=[G00mat G00vec]; G01mat=[G01mat G01vec]; G02mat=[G02mat G02vec];
   G10mat=[G10mat G10vec]; G11mat=[G11mat G11vec]; G12mat=[G12mat G12vec];
   G20mat=[G20mat G20vec]; G21mat=[G21mat G21vec]; G22mat=[G22mat G22vec];
end

% display some of the results
% ---------------------------
figure(1);
    pcolor(Vgvec,Vsdvec,real(SI00mat'));
    colormap(hot);  colorbar('vert'); shading interp;
    xlabel('Vg [ueV] '); ylabel('Vsd [uV] '); title('Si0  [2eA]');
figure(2);
    pcolor(Vgvec,Vsdvec,real(SI11mat'));
    colormap(hot); colorbar('vert'); shading interp;
    xlabel('Vg [ueV] '); ylabel('Vsd [uV] '); title('Si1  [2eA]');
figure(3);
    pcolor(Vgvec,Vsdvec,real(abs(I0mat)'));
    colormap(hot); colorbar('vert'); shading interp;
    xlabel('Vg [ueV] '); ylabel('Vsd [uV] '); title('|I0| [A]');
figure(4);
    pcolor(Vgvec,Vsdvec,real(G10mat'));
    colormap(hot); colorbar('vert'); shading interp;
    xlabel('Vg [ueV] '); ylabel('Vsd [uV] '); title('G10 [e^2/h]');
figure(5);
    pcolor(Vgvec,Vsdvec,real(G01mat'));
    colormap(hot); colorbar('vert'); shading interp;
    xlabel('Vg [ueV] '); ylabel('Vsd [uV] '); title('G01 [e^2/h]');
```

# Bibliography


[1] C. W. J. Beenakker and H. van Houten, *Quantum transport in semiconductor nanostructures*, Solid State Phys. **44**, 1 (1991).

[2] S. Datta, *Electronic tansport in mesoscopic systems* (Cambridge University Press, Cambridge, 1995).

[3] L. P. Kouwenhoven, C. M. Marcus, P. L. McEuen, S. Tarucha, R. M. Westervelt, and N. S. Wingreen, *Electron transport in quantum dots*, in *Mesoscopic Electron Transport*, edited by L. L. Sohn, L. P. Kouwenhoven, and G. Schön, NATO ASI Series E, Vol. 345 (Kluwer, Dordrecht, 1997).

[4] *Mesoscopic phenomena in solids*, edited by B. L. Altshuler, P. A. Lee, and R. A. Webb (North-Holland, Amsterdam, 1991).

[5] K. von Klitzing, *The quantized Hall effect*, Rev. Mod. Phys. **58**, 519 (1986).

[6] H. L. Stormer, D. C. Tsui, and A. C. Gossard, *The fractional quantum Hall effect*, Rev. Mod. Phys. **71**, S298 (1999).

[7] B. J. van Wees, H. van Houten, C. W. J. Beenakker, J. G. Williamson, L. P. Kouwenhoven, D. van der Marel, and C. T. Foxon, *Quantized conductance of point contacts in a two-dimensional electron gas*, Phys. Rev. Lett. **60**, 848 (1988).

[8] D. A. Wharam, T. J. Thornton, R. Newbury, M. Pepper, H. Ahmed, J. E. F. Frost, D. G. Hasko, D. C. Peacock, D. A. Ritchie, and G. A. C. Jones, *One-dimensional transport and the quantization of the ballistic resistance*, J. Phys. C **21**, L209 (1988).

[9] D. Goldhaber-Gordon, H. Shtrikman, D. M. andD. Abusch-Magder, U. Meirav, and M. A. Kastner, *Kondo effect in a single-electron transistor*, Nature **391**, 156 (1998).

[10] S. M. Cronenwett, O. T. H., and L. P. Kouwenhoven, *A tunable Kondo effect in quantum dots*, Science **281**, 540 (1998).

[11] P. Horowitz and W. Hill, *The art of electronics*, 2nd Ed. (Cambridge University Press, Cambridge, 1989).

[12] H. Pothier, P. Lafarge, C. Urbina, D. Esteve, and M. H. Devoret, *Single-electron pump based on charging effects*, Europhys. Lett. **17**, 249 (1992).

[13] M. Moskalets and M. Büttiker, *Floquet scattering theory of quantum pumps*, Phys. Rev. B **66**, 205320 (2002).

[14] M. Moskalets and M. Büttiker, *Adiabatic quantum pump in the presence of external ac voltages*, Phys. Rev. B **69**, 205316 (2004).

[15] M. Moskalets and M. Büttiker, *Magnetic-field symmetry of pump currents of adiabatically driven mesoscopic structures*, Phys. Rev. B **72**, 035324 (2005).

[16] L. DiCarlo, C. M. Marcus, and J. S. Harris, *Photocurrent, rectification, and magnetic field symmetry of induced current through quantum dots*, Phys. Rev. Lett. **91**, 246804 (2003).

[17] M. Switkes, C. M. Marcus, K. Campman, and A. C. Gossard, *An adiabatic quantum electron pump*, Science **283**, 1905 (1999).

[18] F. Zhou, B. Spivak, and B. Altshuler, *Mesoscopic mechanism of adiabatic charge transport*, Phys. Rev. Lett. **82**, 608 (1999).

[19] T. A. Shutenko, I. L. Aleiner, and B. L. Altshuler, *Mesoscopic fluctuations of adiabatic charge pumping in quantum dots*, Phys. Rev. B **61**, 10366 (2000).

[20] I. L. Aleiner, B. L. Altshuler, and A. Kamenev, *Quantum pumping in the magnetic field: Role of discrete symmetries*, Phys. Rev. B **62**, 10373 (2000).

[21] P. W. Brouwer, *Rectification of displacement currents in an adiabatic electron pump*, Phys. Rev. B **63**, 121303 (2001).

[22] M. G. Vavilov, V. Ambegaokar, and I. L. Aleiner, *Charge pumping and photovoltaic effect in open quantum dots*, Phys. Rev. B **63**, 195313 (2001).

[23] M. G. Vavilov, L. DiCarlo, and C. M. Marcus, *Photovoltaic and rectification currents in quantum dots*, Phys. Rev. B **71**, 241309 (2005).

[24] M. Field, C. G. Smith, M. Pepper, D. A. Ritchie, J. E. F. Frost, G. A. C. Jones, and D. G. Hasko, *Measurements of coulomb blockade with a noninvasive voltage probe*, Phys. Rev. Lett. **70**, 1311 (1993).

[25] D. S. Duncan, C. Livermore, R. M. Westervelt, K. D. Maranowski, and A. C. Gossard, *Direct measurement of the destruction of charge quantization in a single-electron box*, Appl. Phys. Lett. **74**, 1045 (1999).

[26] Y. Hu, H. O. H. Churchill, D. J. Reilly, J. Xiang, C. M. Lieber, and C. M. Marcus, *A Ge/Si heterostructure nanowire-based double quantum dot with integrated charge sensor*, Nature Nanotech. **2**, 622 (2007).

[27] R. J. Schoelkopf, P. Wahlgren, A. A. Kozhevnikov, P. Delsing, and D. E. Prober, *The radio-frequency single-electron transistor (rf-set): a fast and ultrasensitive electrometer*, Science **280**, 1238 (1998).

[28] E. Buks, R. Schuster, M. Heiblum, D. Mahalu, and V. Umasky, *Dephasing in electron interference by a 'which-path' detector*, Nature **391**, 871 (1998).

[29] I. L. Aleiner, N. S. Wingreen, and Y. Meir, *Dephasing and the orthogonality catastrophe in tunneling through a quantum dot: The 'which path?' interferometer*, Phys. Rev. Lett. **79**, 3740 (1997).

[30] Y. Levinson, *Dephasing in a quantum dot due to coupling with a quantum point contact*, Europhys. Lett. **39**, 299 (1997).

[31] S. M. Sze and K. K. Ng, *Physics of semiconductor devices*, 3rd Ed. (Wiley, Hoboken, 2007).

[32] L. DiCarlo, H. J. Lynch, A. C. Johnson, L. I. Childress, K. Crockett, C. M. Marcus, M. P. Hanson, and A. C. Gossard, *Differential charge sensing and charge delocalization in a tunable double quantum dot*, Phys. Rev. Lett. **92**, 226801 (2004).

[33] I. Amlani, A. O. Orlov, G. L. Snider, C. S. Lent, and G. H. Bernstein, *External charge state detection of a double-dot system*, Appl. Phys. Lett. **71**, 1730 (1997).

[34] T. M. Buehler, D. J. Reilly, R. Brenner, A. R. Hamilton, A. S. Dzurak, and R. G. Clark, *Correlated charge detection for readout of a solid-state quantum computer*, Appl. Phys. Lett. **82**, 577 (2003).

[35] A. C. Johnson, C. M. Marcus, M. P. Hanson, and A. C. Gossard, *Charge sensing of excited states in an isolated double quantum dot*, Phys. Rev. B **71**, 115333 (2005).

[36] J. Petta, A. Johnson, J. Taylor, E. Laird, A. Yacoby, M. Lukin, C. Marcus, M. P. Hanson, and A. Gossard, *Coherent manipulation of coupled electron spins in semiconductor quantum dots*, Science **309**, 2180 (2005).

[37] D. J. Reilly, C. M. Marcus, M. P. Hanson, and A. C. Gossard, *Fast single-charge sensing with an rf quantum point contact*, Appl. Phys. Lett. **91**, 162101 (2007).

[38] S. Kogan, *Electronic noise and fluctuations in solids* (Cambridge University Press, Cambridge, 1996).

[39] Y. M. Blanter and M. Büttiker, *Shot noise in mesoscopic conductors*, Phys. Rep. **336**, 1 (2000).

[40] F. Pobell, *Matter and methods at low temperatures*, 2nd Ed. (Springer-Verlag, Berlin, 1996).

[41] L. DiCarlo, Y. Zhang, D. T. McClure, C. M. Marcus, L. N. Pfeiffer, and K. W. West, *System for measuring auto- and cross correlation of current noise at low temperatures*, Rev. Sci. Instrum. **77**, 073906 (2006).

[42] L. Spietz, K. W. Lehnert, I. Siddiqi, and R. J. Schoelkopf, *Primary electronic thermometry using the shot noise of a tunnel junction*, Science **300**, 1929 (2003).

[43] A. H. Steinbach, J. M. Martinis, and M. H. Devoret, *Observation of hot-electron shot noise in a metallic resistor*, Phys. Rev. Lett. **76**, 3806 (1996).

[44] M. Henny, S. Oberholzer, C. Strunk, and C. Schönenberger, *1/3-shot-noise suppression in diffusive nanowires*, Phys. Rev. B **59**, 2871 (1999).

[45] S. Oberholzer, E. V. Sukhorukov, C. Strunk, C. Schönenberger, T. Heinzel, and M. Holland, *Shot noise by quantum scattering in chaotic cavities*, Phys. Rev. Lett. **86**, 2114 (2001).

[46] Y. M. Blanter, *Recent advances in studies of current noise*, available at `http://arxiv.org/cond-mat/0511478`.

[47] R. de-Picciotto, M. Reznikov, M. Heiblum, V. umansky, G. Bunin, and D. Mahalu, *Direct observation of a fractional charge*, Nature **389**, 162 (1997).

[48] L. Saminadayar, D. C. Glattli, Y. Jin, and B. Etienne, *Observation of the e/3 fractionally charged laughlin quasiparticle*, Phys. Rev. Lett. **79**, 2526 (1997).

[49] M. Reznikov, R. de Picciotto, T. G. Griffiths, M. Heiblum, and V. Umansky, *Observation of quasiparticles with one-fifth of an electron's charge*, Nature **399**, 238 (1999).

[50] X. Jehl, M. Sanquer, R. Calemczuk, and D. Mailly, *Detection of doubled shot noise in short normal-metal/superconductor junctions*, Nature **405**, 50 (2000).

[51] P. Samuelsson, E. V. Sukhorukov, and M. Büttiker, *Two-particle Aharonov-Bohm effect and entanglement in the electronic Hanbury Brown–Twiss setup*, Phys. Rev. Lett. **92**, 026805 (2004).

[52] I. Neder, N. Ofek, Y. Chung, M. Heiblum, D. Mahalu, and V. Umansky, *Interference between two independent electrons: observation of two-particle Aharonov-Bohm interference*, available at `http://arxiv.org/abs/0705.0173`.

[53] M. Büttiker, *Scattering theory of current and intensity noise correlations in conductors and wave guides*, Phys. Rev. B **46**, 12485 (1992).

[54] L. DiCarlo, Y. Zhang, D. T. McClure, D. J. Reilly, C. M. Marcus, L. N. Pfeiffer, and K. W. West, *Shot-noise signatures of 0.7 structure and spin in a quantum point contact*, Phys. Rev. Lett. **97**, 036810 (2006).

[55] L. DiCarlo, Y. Zhang, D. T. McClure, D. J. Reilly, C. M. Marcus, L. N. Pfeiffer, K. W. West, M. P. Hanson, and A. C. Gossard, *Current noise in quantum point contacts*, available at `http://arxiv.org/abs/0704.3892v1`.

[56] K. J. Thomas, J. T. Nicholls, M. Y. Simmons, M. Pepper, D. R. Mace, and D. A. Ritchie, *Possible spin polarization in a one-dimensional electron gas*, Phys. Rev. Lett. **77**, 135 (1996).

[57] D. J. Reilly, *Phenomenological model for the 0.7 conductance feature in quantum wires*, Phys. Rev. B **72**, 033309 (2005).

[58] M. Reznikov, M. Heiblum, H. Shtrikman, and D. Mahalu, *Temporal correlation of electrons: Suppression of shot noise in a ballistic quantum point contact*, Phys. Rev. Lett. **75**, 3340 (1995).

[59] A. Kumar, L. Saminadayar, D. C. Glattli, Y. Jin, and B. Etienne, *Experimental test of the quantum shot noise reduction theory*, Phys. Rev. Lett. **76**, 2778 (1996).

[60] P. Roche, J. Ségala, D. C. Glattli, J. T. Nicholls, M. Pepper, A. C. Graham, K. J. Thomas, M. Y. Simmons, and D. A. Ritchie, *Fano factor reduction on the 0.7 conductance structure of a ballistic one-dimensional wire*, Phys. Rev. Lett. **93**, 116602 (2004).

[61] T. Rejec and Y. Meir, *Magnetic impurity formation in quantum point contacts*, Nature **442**, 900 (2006).

[62] A. Golub, T. Aono, and Y. Meir, *Suppression of shot noise in quantum point contacts in the '0.7 regime'*, Phys. Rev. Lett. **97**, 186801 (2006).

[63] A. Lassl, P. Schlagheck, and K. Richter, *Effects of short-range interactions on transport through quantum point contacts: A numerical approach*, Phys. Rev. B **75**, 045346 (2007).

[64] P. Jaksch, I. Yakimenko, and K.-F. Berggren, *From quantum point contacts to quantum wires: Density-functional calculations with exchange and correlation effects*, Phys. Rev. B **74**, 235320 (2006).

[65] L. DiCarlo, J. R. Williams, Y. Zhang, D. T. McClure, and C. M. Marcus, *Shot noise in graphene*, available at `http://arxiv.org/abs/0711.3206`.

[66] D. T. McClure, L. DiCarlo, Y. Zhang, H.-A. Engel, C. M. Marcus, M. P. Hanson, and A. C. Gossard, *Tunable noise cross correlations in a double quantum dot*, Phys. Rev. Lett. **98**, 056801 (2007).

[67] Y. Zhang, L. DiCarlo, D. T. McClure, M. Yamamoto, S. Tarucha, C. M. Marcus, M. P. Hanson, and A. C. Gossard, *Noise correlations in a Coulomb-blockaded quantum dot*, Phys. Rev. Lett. **99**, 036603 (2007).

[68] S. S. Safonov, A. K. Savchenko, D. A. Bagrets, O. N. Jouravlev, Y. V. Nazarov, E. H. Linfield, and D. A. Ritchie, *Enhanced shot noise in resonant tunneling via interacting localized states*, Phys. Rev. Lett. **91**, 136801 (2003).

[69] P. Barthold, F. Hohls, N. Maire, K. Pierz, and R. J. Haug, *Enhanced shot noise in tunneling through a stack of coupled quantum dots*, Phys. Rev. Lett. **96**, 246804 (2006).

[70] Y. Chen and R. A. Webb, *Full shot noise in mesoscopic tunnel barriers*, Phys. Rev. B **73**, 035424 (2006).

[71] Y. Chen and R. A. Webb, *Positive current correlations associated with super-Poissonian shot noise*, Phys. Rev. Lett. **97**, 066604 (2006).

[72] O. V. Lounaasma, *Experimental Principles and Methods Below 1 K*, 1st Ed. (Academic Press, New York, 1974).

[73] J. R. Arthur, *Molecular beam epitaxy*, Surface Science **500**, 189 (2002).

[74] A. C. Johnson, *Charge sensing and spin dynamics in GaAs quantum dots*, Ph.D. thesis, Harvard University (2005).

[75] A. K. Geim and K. S. Novoselov, *The rise of graphene*, Nat. Mater. **6**, 183 (2007).

[76] A. H. Castro Neto, F. Guinea, N. M. R. Peres, K. S. Novoselov, and A. K. Geim, *The electronic properties of graphene*, available at `http://arxiv.org/abs/0709.1163`.

[77] K. S. Novoselov, A. K. Geim, S. V. Morozov, D. Jiang, M. I. Katsnelson, I. V. Grigorieva, S. V. Dubonos, and A. A. Firsov, *Two-dimensional gas of massless Dirac fermions in graphene*, Nature **438**, 197 (2005).

[78] Y. Zhang, Y.-W. Tan, H. L. Stormer, and P. Kim, *Experimental observation of the quantum Hall effect and Berry's phase in graphene*, Nature **438**, 201 (2005).

[79] K. S. Novoselov, Z. Jiang, Y. Zhang, S. V. Morozov, H. L. Stormer, U. Zeitler, J. C. Maan, G. S. Boebinger, P. Kim, and A. K. Geim, *Room-temperature quantum Hall effect in graphene*, Science **315**, 1379 (2007).

[80] S. V. Morozov, K. S. Novoselov, M. I. Katsnelson, F. Schedin, D. Elias, J. A. Jaszczak, and A. K. Geim, *Intrinsic carrier mobilities in graphene and is bilayer*, available at `http://arxiv.org/abs/0710.5304`.

[81] C. Berger, Z. Song, X. Li, X. Wu, N. Brown, C. Naud, D. Mayou, T. Li, J. Hass, A. N. Marchenkov, E. H. Conrad, P. N. First, and W. A. de Heer, *Electronic confinement and coherence in patterned epitaxial graphene*, Science **312**, 1191 (2006).

[82] K. S. Novoselov, A. K. Geim, S. V. Morozov, D. Jiang, Y. Zhang, S. V. Dubonos, I. V. Grigorieva, and A. A. Firsov, *Electric field effect in atomically thin carbon films*, Science **306**, 666 (2004).

[83] J. Martin, N. Akerman, G. Ulbricht, T. Lohmann, J. H. Smet, K. von Klitzing, and A. Yacoby, *Observation of electron-hole puddles in graphene using a scanning single electron transistor*, available at `http://arxiv.org/abs/0705.2180`.

[84] M. C. Lemme, T. J. Echtermeyer, M. Baus, and H. Kurz, *A graphene field effect device*, IEEE Electron Device Lett. **28**, 283 (2007).

[85] B. Huard, J. A. Sulpizio, N. Stander, K. Todd, B. Yang, and D. Goldhaber-Gordon, *Transport measurements across a tunable potential barrier in graphene*, Phys. Rev. Lett. **98**, 236803 (2007).

[86] J. R. Williams, L. DiCarlo, and C. M. Marcus, *Quantum Hall effect in a gate-controlled p-n junction of graphene*, Science **317**, 638 (2007).

[87] D. J. Thouless, *Quantization of particle transport*, Phys. Rev. B **27**, 6083 (1983).

[88] B. Spivak, F. Zhou, and M. T. Beal Monod, *Mesoscopic mechanisms of the photovoltaic effect and microwave absorption in granular metals*, Phys. Rev. B **51**, 13226 (1995).

[89] P. W. Brouwer, *Scattering approach to parametric pumping*, Phys. Rev. B **58**, 10135(R) (1998).

[90] M. L. Polianski and P. W. Brouwer, *Pumped current and voltage for an adiabatic quantum pump*, Phys. Rev. B **64**, 075304 (2001).

[91] V. I. Fal'ko and D. E. Khmel'nitskii, *Mesoscopic photogalvanic effect in microjunctions*, Zh. Eksp. Teor. Fiz. **95**, 328 (1989) [Sov. Phys. JETP **68**, 186 (1989)].

[92] A. A. Bykov, G. M. Gusev, Z. D. Kvon, D. I. Lubyshev, and M. V. P., *Photovoltaic effect in a mesoscopic system*, Pis'ma Zh. Eksp. Teor. Fiz. **49**, 13 (1989) [JETP Lett. **49**, 13 (1989)].

[93] A. A. Bykov, G. M. Gusev, and Z. D. Kvon, *Microwave photoconductivity in a mesoscopic system*, Zh. Eksp. Teor. Fiz. **97**, 1317 (1990) [Sov. Phys. JETP **70**, 742 (1990)].

[94] J. Liu, M. A. Pennington, and N. Giordano, *Mesoscopic photovoltaic effect*, Phys. Rev. B **45**, 1267 (1992).

[95] J. J. Lin, R. E. Bartolo, and N. Giordano, *Photovoltaic effect in Au and Au-Fe microjunctions*, Phys. Rev. B **45**, 14231 (1992).

[96] A. A. Bykov, Z. D. Kvon, L. V. Litvin, Y. V. Nastaushev, V. G. Mansurov, V. P. Migal, and S. P. Moshchenko, *Mesoscopic photovoltaic effect in an electron interferometer*, Pis'ma Zh. Eksp. Teor. Fiz. **58**, 538 (1993) [JETP Lett. **58**, 543 (1993)].

[97] R. E. Bartolo and N. Giordano, *Photovoltaic effect in small superconducting normal-metal systems*, Phys. Rev. B **54**, 3571 (1996).

[98] R. E. Bartolo, N. Giordano, X. Huang, and G. H. Bernstein, *h/e Aharonov-Bohm photovoltaic oscillations in mesoscopic Au rings*, Phys. Rev. B **55**, 2384 (1997).

[99] J. Liu and N. Giordano, *Effect of an ac electric field on phase coherence in thin metal films*, Phys. Rev. B **39**, 9894 (1989).

[100] A. G. Huibers, J. A. Folk, S. R. Patel, C. M. Marcus, C. I. Duruöz, and J. S. Harris, *Low-temperature saturation of the dephasing time and effects of microwave radiation on open quantum dots*, Phys. Rev. Lett. **83**, 5090 (1999).

[101] X.-B. Wang and V. E. Kravtsov, *Conductance fluctuations in a quantum dot under almost periodic ac pumping*, Phys. Rev. B **64**, 033313 (2001).

[102] J. J. Lin and J. P. Bird, *Recent experimental studies of electron dephasing in metal and semiconductor mesoscopic structures*, J. Phys. Condens. Matter **14**, R501 (2002).

[103] M. G. Vavilov and I. L. Aleiner, *Theory of dephasing by external perturbation in open quantum dots*, Phys. Rev. B **60**, 16311(R) (1999).

[104] M. G. Vavilov and I. L. Aleiner, *Conductance fluctuations of open quantum dots under microwave radiation*, Phys. Rev. B **64**, 085115 (2001).

[105] S. W. Kim, *Floquet scattering in parametric electron pumps*, Phys. Rev. B **66**, 235304 (2002).

[106] M. Switkes, *Decoherence and adiabatic transport in semiconductor quantum dots*, Ph.D. thesis, Stanford University (1999).

[107] A. G. Huibers, M. Switkes, C. M. Marcus, K. Campman, and A. C. Gossard, *Dephasing in open quantum dots*, Phys. Rev. Lett. **81**, 200 (1998).

[108] I. H. Chan, R. M. Westervelt, K. D. Maranowski, and A. C. Gossard, *Strongly capacitively coupled quantum dots*, Appl. Phys. Lett. **80**, 1818 (2002).

[109] S. Gardelis, C. G. Smith, J. Cooper, D. A. Ritchie, E. H. Linfield, Y. Jin, and M. Pepper, *Dephasing in an isolated double-quantum-dot system deduced from single-electron polarization measurements*, Phys. Rev. B **67**, 073302 (2003).

[110] H.-A. Engel, V. N. Golovach, D. Loss, L. M. K. Vandersypen, J. M. Elzerman, R. Hanson, and L. P. Kouwenhoven, *Measurement efficiency and n-shot readout of spin qubits*, Phys. Rev. Lett. **93**, 106804 (2004).

[111] W. G. van der Wiel, S. De Franceschi, J. M. Elzerman, T. Fujisawa, S. Tarucha, and L. P. Kouwenhoven, *Electron transport through double quantum dots*, Rev. Mod. Phys. **75**, 1 (2002).

[112] W. Lu, Z. Ji, L. Pfeiffer, K. W. West, and A. J. Rimberg, *Real-time detection of electron tunnelling in a quantum dot*, Nature **423**, 422 (2003).

[113] J. M. Elzerman, R. Hanson, J. S. Greidanus, L. H. Willems van Beveren, S. De Franceschi, L. M. K. Vandersypen, S. Tarucha, and L. P. Kouwenhoven, *Few-electron quantum dot circuit with integrated charge read out*, Phys. Rev. B **67**, 161308(R) (2003).

[114] R. H. Blick, R. J. Haug, J. Weis, D. Pfannkuche, K. v. Klitzing, and K. Eberl, *Single-electron tunneling through a double quantum dot: The artificial molecule*, Phys. Rev. B **53**, 7899 (1996).

[115] C. Livermore, C. H. Crouch, R. M. Westervelt, K. L. Campman, and A. C. Gossard, *The Coulomb blockade in coupled quantum dots*, Science **274**, 1332 (1996).

[116] C. Cohen-Tannoudji, *Quantum Mechanics* (Wiley, New York, 1977), Vol. 1, Ch. 4.

[117] R. Ziegler, C. Bruder, and H. Schoeller, *Transport through double quantum dots*, Phys. Rev. B **62**, 1961 (2000).

[118] T. Martin, *Noise in mesoscopic physics*, in *Nanophysics: coherence and transport, Les Houches Session LXXXI*, edited by H. Bouchiat, Y. Gefen, S. Gueron, G. Montambaux, and J. Dalibard (Elsevier, New York, 2005).

[119] R. C. Liu, B. Odom, Y. Yamamoto, and S. Tarucha, *Quantum interference in electron collision*, Nature **391**, 263 (1998).

[120] S. Gustavsson, R. Leturcq, B. Simovič, R. Schleser, T. Ihn, P. Studerus, K. Ensslin, D. C. Driscoll, and A. C. Gossard, *Counting statistics of single electron transport in a quantum dot*, Phys. Rev. Lett. **96**, 076605 (2006).

[121] S. Gustavsson, R. Leturcq, B. Simovič, R. Schleser, P. Studerus, T. Ihn, K. Ensslin, D. C. Driscoll, and A. C. Gossard, *Counting statistics and super-Poissonian noise in a quantum dot: Time-resolved measurements of electron transport*, Phys. Rev. B **74**, 195305 (2006).

[122] E. Onac, F. Balestro, B. Trauzettel, C. F. J. Lodewijk, and L. P. Kouwenhoven, *Shot-noise detection in a carbon nanotube quantum dot*, Phys. Rev. Lett. **96**, 026803 (2006).

[123] T. Martin, A. Crépieux, and N. Chtchelkatchev, *Noise correlations, entanglement, and Bell inequalities*, in *Quantum noise in mesoscopic physics*, edited by Y. V. Nazarov, NATO Science Series II, Vol. 97 (Kluwer, Dordrecht, 2003).

[124] C. W. J. Beenakker, M. Kindermann, C. M. Marcus, and A. Yacoby, *Entanglement production in a chaotic quantum dot*, in *Fundamental Problems in Mesoscopic Physics*, edited by I. V. Lerner, B. L. Altshuler, and Y. Gefen, NATO Science Series II, Vol. 154 (Kluwer, Dordrecht, 2004).

[125] A. V. Lebedev, G. B. Lesovik, and G. Blatter, *Entanglement in a noninteracting mesoscopic structure*, Phys. Rev. B **71**, 045306 (2005).

[126] R. J. Schoelkopf, P. J. Burke, A. A. Kozhevnikov, D. E. Prober, and M. J. Rooks, *Frequency dependence of shot noise in a diffusive mesoscopic conductor*, Phys. Rev. Lett. **78**, 3370 (1997).

[127] D. C. Glattli, P. Jacques, A. Kumar, P. Pari, and L. Saminadayar, *A noise detection scheme with 10 mk noise temperature resolution for semiconductor single electron tunneling devices*, J. Appl. Phys. **81**, 7350 (1997).

[128] M. Sampietro, L. Fasoli, and G. Ferrari, *Spectrum analyzer with noise reduction by cross-correlation technique on two channels*, Rev. Sci. Instrum. **70**, 2520 (1999).

[129] M. Henny, S. Oberholzer, C. Strunk, T. Heinzel, K. Ensslin, M. Holland, and C. Schönenberger, *The fermionic Hanbury Brown and Twiss experiment*, Science **284**, 296 (1999).

[130] S. Oberholzer, M. Henny, C. Strunk, C. Schönenberger, T. Heinzel, K. Ensslin, and M. Holland, *The Hanbury Brown and Twiss experiment with fermions*, Physica E **6**, 314 (2000).

[131] S. Oberholzer, E. Bieri, C. Schönenberger, M. Giovannini, and J. Faist, *Positive cross correlations in a normal-conducting fermionic beam splitter*, Phys. Rev. Lett. **96**, 046804 (2006).

[132] W. D. Oliver, J. Kim, R. C. Liu, and Y. Yamamoto, *Hanbury Brown and Twiss-type experiment with electrons*, Science **284**, 299 (1999).

[133] A. T. Lee, *Broadband cryogenic preamplifiers incorporating gaas mesfets for use with low-temperature particle detectors*, Rev. Sci. Instrum. **60**, 3315 (1989).

[134] A. T.-J. Lee, *A low-power-dissipation broadband cryogenic preamplifier utilizing gaas mesfets in parallel*, Rev. Sci. Instrum. **64**, 2373 (1993).

[135] A. M. Robinson and V. I. Talyanskii, *Cryogenic amplifier for* $\sim 1$ *Mhz with a high input impedance using a commercial pseudomorphic high electron mobility transistor*, Rev. Sci. Instrum. **75**, 3169 (2004).

[136] A. V. Oppenheim and R. W. Schafer, *Discrete-time signal processing* (Prentice-Hall, Englewood Cliffs, 1989).

[137] J. B. Hagen, *Radio-Frequency Electronics* (Cambridge University Press, Cambridge, 1996).

[138] M. Frigo and S. G. Johnson, *FFTW: an adaptive software architecture for the FFT*, in *Proceedings of the IEEE International Conference on Acoustics, Speech, and Signal Processing*, Vol. 3, 1381 (IEEE, New York, 1998).

[139] R. H. Dicke, *The measurement of thermal radiation at microwave frequencies*, Rev. Sci. Instrum. **17**, 268 (1946).

[140] G. B. Lesovik, *Excess quantum noise in 2d ballisic point contacts*, Pis'ma Zh. Eksp. Teor. Fiz. **49**, 513 (1989) [JETP Lett. **49**, 592 (1989)].

[141] M. Büttiker, *Scattering theory of thermal and excess noise in open conductors*, Phys. Rev. Lett. **65**, 2901 (1990).

[142] A. Kristensen, H. Bruus, A. E. Hansen, J. B. Jensen, P. E. Lindelof, C. J. Marckmann, J. Nygård, C. B. Sørensen, F. Beuscher, A. Forchel, and M. Michel, *Bias and temperature dependence of the 0.7 conductance anomaly in quantum point contacts*, Phys. Rev. B **62**, 10950 (2000).

[143] D. J. Reilly, G. R. Facer, A. S. Dzurak, B. E. Kane, R. G. Clark, P. J. Stiles, R. G. Clark, A. R. Hamilton, J. L. O'Brien, N. E. Lumpkin, L. N. Pfeiffer, and K. W. West, *Many-body spin-related phenomena in ultra low-disorder quantum wires*, Phys. Rev. B **63**, 121311(R) (2001).

[144] D. J. Reilly, T. M. Buehler, J. L. O'Brien, A. R. Hamilton, A. S. Dzurak, R. G. Clark, B. E. Kane, L. N. Pfeiffer, and K. W. West, *Density-dependent spin polarization in ultra-low-disorder quantum wires*, Phys. Rev. Lett. **89**, 246801 (2002).

[145] S. M. Cronenwett, H. J. Lynch, D. Goldhaber-Gordon, L. P. Kouwenhoven, C. M. Marcus, K. Hirose, N. S. Wingreen, and V. Umansky, *Low-temperature fate of the 0.7 structure in a point contact: A Kondo-like correlated state in an open system*, Phys. Rev. Lett. **88**, 226805 (2002).

[146] W. D. Oliver, *The generation and detection of electron entanglement*, Ph.D. thesis, Stanford University (2002).

[147] L. P. Rokhinson, L. N. Pfeiffer, and K. W. West, *Spontaneous spin polarization in quantum point contacts*, Phys. Rev. Lett. **96**, 156602 (2006).

[148] C.-K. Wang and K.-F. Berggren, *Spin splitting of subbands in quasi-one-dimensional electron quantum channels*, Phys. Rev. B **54**, 14257(R) (1996).

[149] H. Bruus, V. V. Cheianov, and K. Flensberg, *The anomalous 0.5 and 0.7 conductance plateaus in quantum point contacts*, Physica E **10**, 97 (2001).

[150] Y. Meir, K. Hirose, and N. S. Wingreen, *Kondo model for the ı0.7 anomalyȷ in transport through a quantum point contact*, Phys. Rev. Lett. **89**, 196802 (2002).

[151] K. A. Matveev, *Conductance of a quantum wire in the wigner-crystal regime*, Phys. Rev. Lett. **92**, 106801 (2004).

[152] A. Ramšak and J. H. Jefferson, *Shot noise reduction in quantum wires with the 0.7 structure*, Phys. Rev. B **71**, 161311(R) (2005).

[153] M. Avinun-Kalish, M. Heiblum, A. Silva, D. Mahalu, and V. Umansky, *Controlled dephasing of a quantum dot in the Kondo regime*, Phys. Rev. Lett. **92**, 156801 (2004).

[154] L. P. Kouwenhoven, B. J. van Wees, C. J. P. M. Harmans, J. G. Williamson, H. van Houten, C. W. J. Beenakker, C. T. Foxon, and J. J. Harris, *Nonlinear conductance of quantum point contacts*, Phys. Rev. B **39**, 8040(R) (1989).

[155] N. K. Patel, J. T. Nicholls, L. Martn-Moreno, M. Pepper, J. E. F. Frost, D. A. Ritchie, and G. A. C. Jones, *Evolution of half plateaus as a function of electric field in a ballistic quasi-one-dimensional constriction*, Phys. Rev. B **44**, 13549 (1991).

[156] M. Büttiker, *Quantized transmission of a saddle-point constriction*, Phys. Rev. B **41**, 7906 (1990).

[157] M. P. Anantram and S. Datta, *Current fluctuations in mesoscopic systems with Andreev scattering*, Phys. Rev. B **53**, 16390 (1996).

[158] T. Martin, *Wave packet approach to noise in n-s junctions*, Phys. Lett. A **220**, 137 (1996).

[159] J. Torrès and T. Martin, *Positive and negative Hanbury-Brown and Twiss correlations in normal metal-superconducting devices*, Eur. Phys. J. B **12**, 319 (1999).

[160] A. M. Martin and M. Büttiker, *Coulomb-induced positive current-current correlations in normal conductors*, Phys. Rev. Lett. **84**, 3386 (2000).

[161] I. Safi, P. Devillard, and T. Martin, *Partition noise and statistics in the fractional quantum Hall effect*, Phys. Rev. Lett. **86**, 4628 (2001).

[162] A. Crépieux, R. Guyon, P. Devillard, and T. Martin, *Electron injection in a nanotube: noise correlations and entanglement*, Phys. Rev. B **67**, 205408 (2003).

[163] M. Büttiker, *Reversing the sign of current-current correlations*, in *Quantum noise in mesoscopic physics*, edited by Y. V. Nazarov, NATO Science Series II, Vol. 97 (Kluwer, Dordrecht, 2003).

[164] A. Cottet, W. Belzig, and C. Bruder, *Positive cross correlations in a three-terminal quantum dot with ferromagnetic contacts*, Phys. Rev. Lett. **92**, 206801 (2004).

[165] A. Cottet, W. Belzig, and C. Bruder, *Positive cross-correlations due to dynamical channel blockade in a three-terminal quantum dot*, Phys. Rev. B **70**, 115315 (2004).

[166] C. Texier and M. Büttiker, *Effect of incoherent scattering on shot noise correlations in the quantum Hall regime*, Phys. Rev. B **62**, 7454 (2000).

[167] S.-T. Wu and S. Yip, *Feedback effects on the current correlations in Y-shaped conductors*, Phys. Rev. B **72**, 153101 (2005).

[168] V. Rychkov and M. Büttiker, *Mesoscopic versus macroscopic division of current fluctuations*, Phys. Rev. Lett. **96**, 166806 (2006).

[169] S. Hershfield, J. H. Davies, P. Hyldgaard, C. J. Stanton, and J. W. Wilkins, *Zero-frequency current noise for the double-tunnel-junction Coulomb blockade*, Phys. Rev. B **47**, 1967 (1993).

[170] M. Eto, *Nonequilibrium transport properties through parallel quantum dots*, Jpn. J. Appl. Phys. **36**, 4004 (1997).

[171] G. Kießlich, A. Wacker, and E. Schöll, *Shot noise of coupled semiconductor quantum dots*, Phys. Rev. B **68**, 125320 (2003).

[172] C. W. J. Beenakker, *Theory of Coulomb-blockade oscillations in the conductance of a quantum dot*, Phys. Rev. B **44**, 1646 (1991).

[173] W. Belzig, *Full counting statistics of super-Poissonian shot noise in multilevel quantum dots*, Phys. Rev. B **71**, 161301(R) (2005).

[174] E. V. Sukhorukov, G. Burkard, and D. Loss, *Noise of a quantum dot system in the cotunneling regime*, Phys. Rev. B **63**, 125315 (2001).

[175] A. Thielmann, M. H. Hettler, J. König, and G. Schön, *Cotunneling current and shot noise in quantum dots*, Phys. Rev. Lett. **95**, 146806 (2005).

[176] G. Iannaccone, G. Lombardi, M. Macucci, and B. Pellegrini, *Enhanced shot noise in resonant tunneling: Theory and experiment*, Phys. Rev. Lett. **80**, 1054 (1998).

[177] O. Zarchin, Y. C. Chung, M. Heiblum, D. Rohrlich, and V. Umansky, *Electron bunching in transport through quantum dots in a high magnetic field*, Phys. Rev. Lett. **98**, 066801 (2007).

[178] H.-A. Engel, *Electron spins in dots and rings: coherence, read out, and transport*, Ph.D. thesis, University of Basel (2003).

[179] J. Tworzydło, B. Trauzettel, M. Titov, A. Rycerz, and C. W. J. Beenakker, *Sub-Poissonian shot noise in graphene*, Phys. Rev. Lett. **96**, 246802 (2006).

[180] V. V. Cheianov and V. I. Fal'ko, *Selective transmission of Dirac electrons and ballistic magnetoresistance of n-p junctions in graphene*, Phys. Rev. B **74**, 041403(R) (2006).

[181] P. San-Jose, E. Prada, and D. S. Golubev, *Universal scaling of current fluctuations in disordered graphene*, available at http://arxiv.org/abs/0706.383207.

[182] C. W. J. Beenakker and M. Büttiker, *Suppression of shot noise in metallic diffusive conductors*, Phys. Rev. B **46**, 1889(R) (1992).

[183] M. J. M. de Jong and C. W. J. Beenakker, *Mesoscopic fluctuations in the shot-noise power of metals*, Phys. Rev. B **46**, 13400 (1992).

[184] Y. V. Nazarov, *Limits of universality in disordered conductors*, Phys. Rev. Lett. **73**, 134 (1994).

[185] C. H. Lewenkopf, E. R. Mucciolo, and A. H. Castro Neto, *Conductivity and Fano factor in disordered graphene*, available at `http://arxiv.org/abs/0711.3202`.

[186] E. McCann and V. I. Fal'ko, *Landau-level degeneracy and quantum Hall effect in a graphite bilayer*, Phys. Rev. Lett. **96**, 086805 (2006).

[187] A. Rycerz, J. Tworzydło, and C. W. J. Beenakker, *Anomalously large conductance fluctuations in weakly disordered graphene*, Europhys. Lett. **79**, 57003 (2007).

[188] D. Graf, F. Molitor, T. Ihn, and K. Ensslin, *Phase-coherent transport measured in a side-gated mesoscopic graphite wire*, Phys. Rev. B **75**, 245429 (2007).

[189] Y. Zhang, J. P. Small, M. E. S. Amori, and P. Kim, *Electric field modulation of galvanomagnetic properties of mesoscopic graphite*, Phys. Rev. Lett. **94**, 176803 (2005).

[190] I. Snyman and C. W. J. Beenakker, *Ballistic transmission through a graphene bilayer*, Phys. Rev. B **75**, 045322 (2007).

[191] F. Schedin, A. K. Geim, S. V. Morozov, E. W. Hill, P. Blake, M. I. Katsnelson, and K. S. Novoselov, *Detection of individual gas molecules adsorbed on graphene*, Nat. Mater. **6**, 652 (2007).

[192] E. H. Hwang, S. Adam, S. D. Sarma, and A. K. Geim, *Transport in chemically doped graphene in the presence of adsorbed molecules*, available at `http://arxiv.org/abs/cond-mat/0610834`.

[193] Z. Chen, Y.-M. Lin, M. J. Rooks, and P. Avouris, *Graphene non-ribbon electronics*, available at `http://arxiv.org/abs/cond-mat/0701599`.

[194] M. Y. Han, B. Özyilmaz, Y. Zhang, and P. Kim, *Energy band-gap engineering of graphene nanoribbons*, Phys. Rev. Lett. **98**, 206805 (2007).

[195] A. Rycerz, J. Tworzydło, and C. W. J. Beenakker, *Valley filter and valley valve in graphene*, Nature Phys. **3**, 172 (2007).

[196] H. B. Heersche, P. Jarillo-Herrero, J. B. Oostinga, and L. M. K. Vnersypen, *Bipolar supercurrent in graphene*, Nature **446**, 56 (2007).

[197] M. I. Katsnelson, K. S. Novoselov, and A. K. Geim, *Chiral tunnelling and the Klein paradox in graphene*, Nature Phys. **2**, 620 (2006).

[198] V. V. Cheianov, V. Fal'ko, and B. L. Altshuler, *The focusing of electron flow and a Veselago lens in graphene p-n junctions*, Science **315**, 1252 (2007).

[199] D. R. Smith, J. B. Pendry, and M. C. K. Wiltshire, *Metamaterials and negative refractive index*, Science **305**, 788 (2004).

[200] D. A. Abanin and L. S. Levitov, *Quantized transport in graphene p-n junctions in a magnetic field*, Science **317**, 641 (2007).

[201] D. B. Farmer and R. G. Gordon, *Atomic layer deposition on suspended single-walled carbon nanotubes via gas-phase noncovalent functionalization*, Nano Lett. **6**, 699 (2006).

[202] V. P. Gusynin and S. G. Sharapov, *Unconventional integer quantum Hall effect in graphene*, Phys. Rev. Lett. **95**, 146801 (2005).

[203] D. A. Abanin, P. A. Lee, and L. S. Levitov, *Spin-filtered edge states and quantum Hall effect in graphene*, Phys. Rev. Lett. **96**, 176803 (2006).

[204] N. M. R. Peres, F. Guinea, and A. H. Castro Neto, *Electronic properties of disordered two-dimensional carbon*, Phys. Rev. B **73**, 125411 (2006).

[205] D. A. Syphers and P. J. Stiles, *Contiguous two-dimensional regions in the quantized Hall regime*, Phys. Rev. B **32**, 6620 (1985).

[206] R. J. Haug, A. H. MacDonald, P. Streda, and K. von Klitzing, *Quantized multichannel magnetotransport through a barrier in two dimensions*, Phys. Rev. Lett. **61**, 2797 (1988).

[207] S. Washburn, A. B. Fowler, H. Schmid, and D. Kern, *Quantized Hall effect in the presence of backscattering*, Phys. Rev. Lett. **61**, 2801 (1988).

[208] E. H. Hwang, S. Adam, and S. D. Sarma, *Carrier transport in two-dimensional graphene layers*, Phys. Rev. Lett. **98**, 186806 (2007).

[209] D. M. Pozar, *Microwave engineering*, 3rd Ed. (Wiley, Hoboken, 2005).